Microscale Engineering for the Structural Integrity and Transport Properties of Electrode Material in Li-ion Batteries

by

Min Zhu

A dissertation submitted in partial fulfillment
of the requirements for the degree of
Doctor of Philosophy
(Mechanical Engineering)
in The University of Michigan
2012

Doctoral Committee:

Professor Ann Marie Sastry, Chair
Professor H. Scott Fogler
Professor Margaret S. Wooldridge
Associate Professor Wei Lu

To My Family and Friends

ACKNOWLEDGEMENTS

I am ever grateful to God, my Creator and Guardian, for the opportunity to step into the excellent community of science, and the wisdom to make a difference in the world. At this time I would like to express my deep appreciation and gratitude to the following people for helping me complete this thesis.

First, I would like to thank Prof. Ann Marie Sastry, my advisor and committee chair, for giving me the opportunity to work on this fascinating and challenging project. From her I learned how to think like a true scientist, engineer, and leader. Her considerable expertise and knowledge, her persistent striving for excellence, and her compassion for her fellow colleagues and friends will always be an inspiration to me.

I would also like to thank my committee members – Prof. H. Scott Fogler, Prof. Margaret Wooldridge, and Prof. Wei Lu. I appreciate all their help and encouragement—from my preliminary exam to my final defense—and their invaluable advice on my thesis.

I am full of gratitude to Dr. Jonghyun Park, my colleague, friend and mentor, for helping me explore my potential and reach the place I am at now. His unceasing support and encouragement were essential to my achievement.

I would like to thank my colleagues from Prof. Sastry's Advanced Materials Systems Laboratory and the GM/UM Advanced Battery Coalition for Drivetrains for their support over the years and the congenial environment they created: Dr. Greg Less, Dr. Joseph Gallegos, Dr. Sangmin Lee, Dr. Seungjun Lee, Dr. Lin Liu, Mr. Sangwoo Han,

Mr. Dong Hoon Song, Mr. Yoon Koo Lee, Mr. Ho Sop Shin, Mr. Xianke Lin, Mr. Wenbo Du, and Mr. Nansi Xue. Thanks also to the former group members: Dr. Chia-Wei Wang, Dr. Munish Inamdar, Dr. Fabio Albano, Dr. Yen-Hung Chen, Dr. HyonCheol Kim, Dr. Xiangchun Zhang, Dr. Myoungdo Chung, Dr. Myounggu Park, Dr. Jeong Hun Seo, Mr. Peter Verhees, Ms. Qiuye Jin, Mr. Tim Slusser, and Mr. KC Miller. I thank them for many wonderful moments in our research community.

I am also grateful for the help of Ms. Eve Bernos, Ms. Nichole Burnside, Ms. Leah Wright, Ms. Samantha Maclaren, Ms. Jamie Eiseman, and Ms. Carol Lagemann for their immense help in administrative matters. Thanks also goes to Dr. Peter Nagourney, Mr. Paul Barron, and Mr. David Karczynski for their excellent editorial efforts.

I also wish to acknowledge the support provided by the U.S. Department of Energy and General Motors.

Special thanks goes to my brothers and sisters in Christ at the Chinese Christian Fellowship Church in Ann Arbor. They showed me God's great love, planted the seed of the Gospel in my heart, and served Him together with me. I thank them all for their prayers, caring and encouragement: David Soemarko, Joe Chou, Amy Chou, Wei Jiang, Lily Zheng, Stephen Jiang, Ye Lu, Min Wang, Joseph Lu, Jiechi Xu, May Lee, Jason Xu, Caleb Xu, Ringo Hui, Zhiling Zeng, James Hui, Daniel Hui, Liou Sun, Jian Wang, Abraham Sun, Alice Sun, Albert Sun, Qian Li, Nan Deng, Daniel Li, Michael Li, Roy Peng, Leah Liu, Stella Peng, Connie Chen, Anne Sin, Ian Sin, Chuanwu Xi, Wei Luo, Susan Xi, Andy Xi, Min Tan, Dongling Tan, Yanhui Guo, Xiaolei Meng, Lois T.A. Yang, CK Chan, Susan Lai, Sarah Chan, Matthew Chan, Ben Kao, Wenbo Zhang, Biyun Wu, Cindy Yayun Chen, Jonathan Chen, Su Chen, Su's mother Ning Su, Eva Chan, Lee Han,

Ziyun Wang, Lingyu Gao, Yu Qiao, Chuqiao Liu, Di Yang, Bingxin Chen, Garry Ng, Maggie Tam, Bingxin Xu, Tian Zhang, Jingjing Zhou, Alice Hwan, and Ursula Lin. To me, they are a loving family, whom I can draw my strength from.

I would like to thank these people for their longtime friendship: Yanli Tao, Sijia Chen, Di Wu, Jianan Du, Yinggang Ji, Yuanchen Huang, Jingzhu Liu, Suyi Li, Xiaoming Tang, Yihan Guan, Simin Chai, Jinjin Ma, Shinan Li, Yunjiao Cai, Boris Yim, Tong Wu, Jin Yan, Dianyun Zhang. I feel warm in my heart thinking of them.

I wish to thank my loving family members in China: Meiqin Sun, Fanong Zhu, Yaorong Zhu, Zhoupin Xu, Weishu Zhu, Weiying Luo, Weidong Zhu, Xiuting Wang, Jiaying Hua, Keqi Qiu, Chongyi Fan, Gonghuan Qiu, Fengying Zhou, Kexin Qiu, Baoxing Yang, Gongmin Qiu, Weiying Chen, Kang Xu, Feng Zhu, Yin Zhu, Bo Wan Yu, Yeqi Qiu, Yechu Fan, Yexi Fan, Yuyin Yang, Yesheng Xu, Manyue Yuan, and Ziyang Li.

I am eternally grateful to my late maternal grandmother Guifeng Xu for being my guardian and closest childhood friend. My remembrance also goes to my late paternal grandfather Wenhao Zhu and my late grandaunt Jufen Zhu.

Finally, I would like to express my profound thanks to my father Weibin Zhu and mother Keqing Qiu, for their endless love. They have stood firmly behind me during every decision I made, and have provided me with unconditional support throughout my twenty-seven years of life, even when I am thousands of miles away from home.

TABLE OF CONTENTS

LIST OF TABLES

LIST OF FIGURES

ABSTRACT

Aggregation between additive particles and active particles in the electrodes of Li-ion batteries is an important process for lithium-ion batteries in that it strongly affects mechanical stability, transport properties, utilization, and gravimetric and volumetric power/energy density. Transport properties, which encompass electrical conductivity, diffusion of lithium ions and reaction rate at the solid/electrolyte interface, determine the power performance of batteries. However, fracture has been experimentally observed in the electrode aggregates. Fracture is a putative degradation mechanism of lithium-ion batteries, one that may cause the rupture of electrode particles and disruption of conductive path, and thus adversely affect the structural integrity as well as transport properties of electrodes.

This thesis proposes two three-dimensional simulation models, in which Brownian dynamics and the Monte Carlo method are employed, respectively, to simulate the aggregation process of conductive additives and active particles. The aggregated structures generated from these models are characterized to analyze the effects of a few manufacturing parameters such as temperature, particle size, particle aspect ratio, and additive to active material mass ratio on the final morphology and transport properties of the electrode. Further, a stress and fracture analysis was carried out on these aggregated structures, as well as on single particles with unconstrained surfaces. The effects of particle geometry and electrochemical loading conditions on fracture propagation in single electrode particles are investigated, as is the location of initial defects. It is also

demonstrated through stress analysis that particles in a cluster have a significantly higher propensity to fracture compared to single particles with unconstrained surfaces under the same electrochemical cycling conditions. Finally, based on the findings of these studies, recommendations are provided for the optimization of Li-ion batteries in terms of conductivity, specific energy, and fracture resistance.

CHAPTER I

INTRODUCTION

Due to the enormous potential market size for both electric and hybrid electric vehicles (EV and HEV), extensive efforts have been made to create a high-performing but still economically practical Li-ion battery system. In particular, much research has focused on lowering the internal resistance and increasing the energy density of Li-ion batteries. One complicating issue, however, is that the energy storage capacity of a Li-ion cell is provided by active materials (e.g. $Li_xMn_2O_4$) that have very low conductivity [1, 2], thus limiting battery power performance. Conductive additives [e.g. carbon black (CB)] of a dimension several orders of magnitude smaller than the active material particles are typically added to improve the conductivity of electrodes. A polymer binder [e.g. polyvinylidene difluoride (PVDF), polytetrafluoroethylene (PTFE)] [3, 4, 5, 6] is used to combine electrode materials into an integrated system and provide mechanical integrity. However, these additives, which vary in scale (Fig. 1), increase the total mass of the battery.

Meanwhile, the growth of the EV and HEV market will also require the development of longer useful lifetimes for Li-ion batteries, particularly in aggressive operating conditions. The current challenge in making batteries that are longer-lasting and more cost-effective relative to vehicle life cycle is reducing capacity fade. A number

of causes are postulated to contribute to capacity fade, including electrochemical, chemical, and mechanical degradation, of which fracture is a part. Fracture of active material particles and conductive aggregates causes separation of particle fragments and isolation of the electronically conducting matrix, resulting in loss of electrical contact [7, 8]. Fracture of active material particles also increases the surface area exposed to the electrolyte, thus increasing side-reactions and Mn^{2+} dissolution [9, 10] into the electrolyte as well as accelerating capacity fade, especially at elevated temperatures. The development and propagation of fractures at the particle and aggregate level can also affect the mechanical stability of Li-ion battery materials. It remains unknown, however, how fractures develop and propagate at different length scales in the battery material, as well as the extent to which local fractures limit battery lifetime.

Figure 1.1 shows a schematic of the cathode system, indicating active material particles and conductive additive particles. The active material particles are usually secondary particles consisting of primary particles and have a size ranging from 100 μm to 1 μm. The primary active material particles have a size on the order of 1 μm. The size of conductive additive particles is measured on the nanometer scale [11]. Several forces and parameters (such as viscous forces, Brownian forces, temperature, conductive additive to active material mass ratio, and particle size distribution) have been thought to be responsible for the morphology of electrode material, as several experimental studies have shown [2, 12, 13, 14]. It has been observed that the active material, conductive additive and polymeric binder form different self-assembled characteristic structures according to the composition of the cathode. For example, it has been found that a higher polymer binder to conductive additive ratio facilitates the contact of the active material

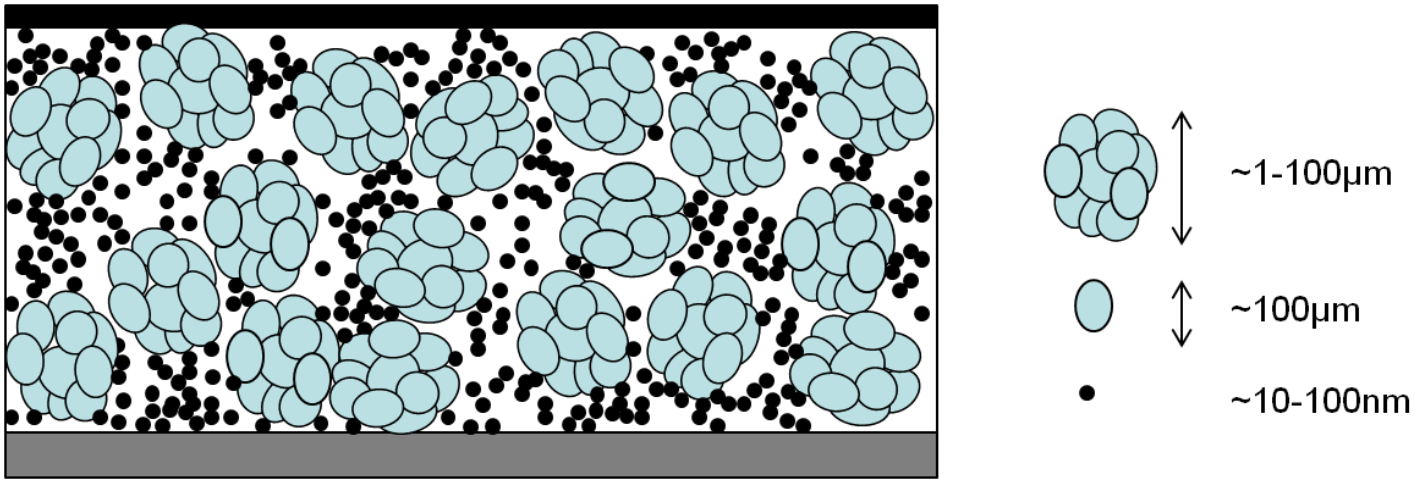

Figure 1.1: Illustration of cathode materials

and the conductive additive, helping forming a conductive network [2, 15]. The morphology of the self-assembled structure in cathodes also plays an important role in structural integrity, because local fracture may not only occur within single cathode particles [2, 8, 16], but also exist at the aggregate level, i.e., inside the binder that connects two particles or at the interface between the binder and the particle. At the aggregate level, fractures occurring within or between secondary particles may also disrupt connectivity, causing loss of conductivity in the cathode.

In order to optimize the composition of cathodes to improve capacity and power density, the appropriate balance of materials needs to be determined. It has been reported that the additives and binders improve conductivity and power performance by forming self-assembled characteristic structures [2, 15]. It has also been suggested that the electrical and ionic conductivities of the cell strongly depend on the final structure of electrode materials, and that structure is directly affected by the interaction of the constituents during electrode fabrication. In this work, we developed a self-assembly algorithm to simulate the aggregation of active material particles and conductive additives. The algorithm simulates the Brownian motion of spherical particles (Mn_2O_4 and carbon black) during the fabrication process of the electrode. We further characterized the aggregated structures generated by the simulation algorithm and identified the key parameters responsible for their characteristics (Chapter II).

In order to study more general and realistic cases for electrode particles, it is desirable to model the interaction between particles of non-spherical shapes. In the cases where pair-wise additive inverse power law potential (such as van der Waals energy) is considered, particle-particle interaction potential can be obtained by integrating over the

volumes of the interacting bodies [17]. However, explicit expressions are only available for several simple geometries. Efforts have been made to obtain the value of the interaction energy using methods that are less computationally intensive than numerical integration over ellipsoid volumes [18, 19, 20, 21, 22, 23]; however, these methods are either limited to certain types of potential profiles or only accurate within a short interaction range. In Chapter III, we modified the aggregation simulation algorithm presented in the previous chapter and extended the shape of active material particles to prolate spheroids (ellipsoids of revolution around their longer semi-axes). We generated a look-up table of interaction potential between two particles (ellipsoid-ellipsoid or ellipsoid-sphere) with parameterized relative position and orientation. We also conducted Monte Carlo simulation and compared the results with a spherical particle system.

One possible cause of fracture in battery materials is high stress. Several models have been developed to determine the stress generated by lithium intercalation and deintercalation. These range from one dimensional to three dimensional models—as well as from analytical expression to numerical simulation—of various cathode active materials such as $LiMn_2O_4$ and $LiFePO_4$ [24, 25, 26, 27, 28, 29, 30, 31, 32, 33]. In Chapter IV, multiphysics simulations and linear elastic fracture mechanics were employed to simulate crack propagation in ellipsoidal cathode particles under realistic electrochemical loading conditions. We investigated the effect of particle size, current density, and particle aspect ratio, as well as the location of the initial defect on fracture propagation. While the prior arts generally consider spherical particles with initial defects located near the surface, we focused on the propagation of initial defects inside the particle during the discharge of cathode materials, thus showing the energetically

favorable location of crack propagation during cycling and revealing new possible processes of particle failure. In Chapter V, we further extended our study from single particles to aggregated networks, conducting stress analyses and fracture simulations on a cluster of $LiMn_2O_4$ active material particles connected by PVDF polymer binders. The relative positions of active material particles are obtained from the Brownian dynamics simulation method presented in Chapter II.

Finally, Chapter VI summarizes the major findings and future directions of our research.

BIBLIOGRAPHY

[1] Chung, S.Y., Bloking, J.T. and Chiang, Y.M., 2002, “Electronically conductive phospho-olivines as lithium storage electrodes”, *Nature Materials*, **1**, pp. 123-128

[2] Liu, G., Zheng, H., Simens, A. S., Minor, A.M., Song, X. and Battaglia, V. S., 2007, “Optimization of acetylene black conductive additive and PVDF composition for high-power rechargeable lithium-ion cells”, *Journal of The Electrochemical Society*, **154** (12), pp. A1129-A1134

[3] Zhang, X., Ross Jr., P.N., Kostecki, R., Kong, F., Sloop, S., Kerr, J. B., Striebel, K., Cairns, E. J. and McLarnon, F., 2001, "Diagnostic characterization of high power lithium-ion batteries for use in hybrid electric vehicles", *Journal of The Electrochemical Society*, **148** (5), pp. A463-A470

[4] Fonseca, C. P., Pallone, E. M. J. A., Neves, S., 2004, "Electrochemical properties of LiMn2O4 films produced by combustion reaction", *Solid State Sciences*, **6**, pp. 1353–1358

[5] Chen, Y.-H., Wang, C.-W., Zhang, X. and Sastry, A. M., 2010, "Porous cathode optimization for lithium cells: Ionic and electronic conductivity, capacity, and selection of materials", *Journal of Power Sources*, **195**, pp. 2851–2862

[6] Manickam, M. and Takata, M., 2003, "Effect of cathode binder on capacity retention and cycle life in transition metal phosphate of a rechargeable lithium battery", *Electrochimica Acta*, **48**, pp. 957-963

[7] Zhu, M., Park, J. and Sastry, A. M., 2011, "Simulation of Particle Interactions in Cathode Material of Li-Ion Batteries", *Journal of The Electrochemical Society,* **158** (10) pp. A1155-A1159

[8] Wang, D., Wu, X., Wang, Z. and Chen L., 2005, "Cracking causing cyclic instability of $LiFePO_4$ cathode material", *Journal of Power Sources*, **140**, pp. 125–128

[9] Blyr, A., Sigala, C., Amatucci, G., Guyomard, D., Chabre, Y. and Tarascon, J.M., 1998, "Self-discharge of LiMn2O4/C Li-ion cells in their discharged state - Understanding by means of three-electrode measurements", *Journal of The Electrochemical Society*, **145** (1), pp.194-209

[10] Park, J., Seo, J. H., Plett, G., Lu, W. and Sastry, A. M., 2011, "Numerical simulation of the effect of the dissolution of LiMn2O4 particles on Li-ion battery performance", Electrochemical and Solid-State Letters, **14** (2), pp. A14-18.

[11] Mandal, S. Amarilla, J. M., Ibanez, J. and Rojo, J. M., 2011 "The role of carbon black in LiMn2O4-based composites as cathodes for rechargeable lithium batteries", *Journal of The Electrochemical Society*, **148** (1), pp. A24-A29

[12] Ligneel, E., Lestriez, B., Hudhomme, A. and Guyomard, D., 2009, "Shaping of Advanced Ceramics: The Case of Composite Electrodes for Lithium Batteries", *Journal of the European Ceramic Society*, **29**, pp. 925-929

[13] Guy, D., Lestriez, B., Bouchet, R. and Guyomard, D., 2006, "Critical Role of Polymetric Binders on the Electronic Transport Properties of Composites Electrode", *Journal of The Electrochemical Society*, **153** (4), pp. A679-A688

[14] Ligneel, E., Lestriez, B. and Guyomard, D., 2007, "Relationships between processing, morphology and discharge capacity of the composite electrode", *Journal of Power Sources*, **174**, pp, 716-719

[15] Liu, G., Zheng, H., Kim, S., Deng, Y., Minor, A. M., Song, X. and Battaglia, V. S., 2008, "Effects of Various Conductive Additive and Polymeric Binder Contents on the Performance of a Lithium-Ion Composite Cathode", *Journal of The Electrochemical Society*, **155** (12), pp. A887-A892

[16] Lim, M.-R., Cho, W.-I. and Kim, K.-B., 2001, "Preparation and characterization of gold-codeposited LiMn2O4 electrodes", *Journal of Power Sources*, **92** , pp. 168-176

[17] Ross, S. and Morrison, I. D., 1988, *Colloidal Systems and Interfaces*, John Wiley & Sons, Inc

[18] Fejer, S. N., Chakrabartia, D.and D.Wales, D. J., 2011, "Self-assembly of anisotropic particles", *Soft Matter*, **7**, pp. 3553

[19] Veble, G. and Podgornik, R. 2007, "The boundary element approach to Van der Waals interactions", *Eur. Phys. J. E* 23, pp. 275–279

[20] Golestanian R., 2005,"Lifshitz Interaction between Dielectric Bodies of Arbitrary Geometry", *Physical Review Letters*, **95**, pp. 230601

[21] Oversteegen, M. S. and Lekkerkerker, N. H. W., 2003, "Testing the Derjaguin approximation for colloidal mixtures of spheres and disks", *Physical Review E*, **68**, pp. 021404

[22] Kruger, S., Mogel, H.-J., Wahab, M. and Schiller, P., 2011,"Depletion Force between Anisometric Colloidal Particles", *Langmuir*, **27**(2), pp. 646–650

[23] Schiller, P., Kruger, S., Wahab, M. and Mogel, H.-J., 2011 "Interactions between Spheroidal Colloidal Particles", *Langmuir*, **27**, pp. 10429–10437

[24] Zaghib, K., Shim, J., Guerfi, A., Charest, P., and Striebel, K. A., 2005, "Effect of carbon source as additives in LiFePO4 as positive electrode for lithium-ion batteries", *Electrochem. Solid-State Lett.*, **8**, pp. A207

[25] Christensen, J. and Newman, J., 2006 "Stress generation and fracture in lithium insertion materials", *J. Solid State Electrochem.*, **10**, pp.293

[26] Zhang, X., Shyy, W., and Sastry, A. M., 2007, "Numerical Simulation of Intercalation-Induced Stress in Li-Ion Battery Electrode Particles", *Journal of The Electrochemical Society*, **154**(10), pp. A910

[27] Zhang, X., Sastry, A.M., and Shyy, W., 2008, "Intercalation-induced stress and heat generation within single lithium-ion battery cathode", Journal of the Electrochemical Society, v.**155**(7), pp.A542

[28]. Cheng, Y.-T and Verbrugge, M. W., 2008, "The influence of surface mechanics on diffusion induced stresses within spherical nanoparticles", *J. Appl. Phys.*, **104**, pp.083521

[29] Cheng, Y.-T. and Verbrugge, M. W., 2009, "Evolution of stress within a spherical insertion electrode particle under potentiostatic and galvanostatic operation", *J. Power Sources*, **190**, pp.453

[30]Cheng, Y.-T. and Verbrugge, M. W., 2010, "Diffusion-Induced Stress, Interfacial Charge Transfer, and Criteria for Avoiding Crack Initiation of Electrode Particles", *Journal of The Electrochemical Society*, **157** (4), A508

[31] Christensen, J. and Newman, J., 2006, "A Mathematical Model of Stress Generation and Fracture in Lithium Manganese Oxide", *Journal of The Electrochemical Society*, **153** (6), pp. A1019

[32] Hu, Y., Zhao, X. and Suo, Z., 2010, "Averting cracks caused by insertion reaction in lithium–ion batteries", *J. Mater. Res*., **25**(6), pp. 1007

[33] Woodford, W. H., Chiang, Y.-M., and Carter, C., 2010, "Electrochemical Shock of Intercalation Electrodes: A Fracture Mechanics Analysis", *Journal of The Electrochemical Society*, **157** (10), pp. A1052

CHAPTER II

INTERACTION AND AGGREGATION OF SPHERICAL PARTICLES IN THE CATHODE[1]

INTRODUCTION

In order to optimize the composition of cathodes to improve capacity and power density, the appropriate balance of materials needs to be determined. It has been reported that interfacial impedance dominates cell impedance; and while the additives and binders improve conductivity and power performance by forming self-assembled characteristic structures [1 , 2], they represent a parasitic mass, thus reducing gravimetric and volumetric energy. An optimal balance between conductive additives and polymeric binders is also required to achieve optimal conductivity and performance. A higher PVDF content (AB/PVDF = 1:2) reduces self-attraction of AB particles, improving cathode capacity at high C-rates (5C); however, electrode conductivity increases and then decreases with increasing AB/PVDF ratio. Based upon these observations, it has been suggested that the electrical and ionic conductivities of the cell strongly depend on the final structure of electrode materials, which structure is directly affected by the interaction of the constituents during electrode fabrication. Accurate reproduction of

[1] Material in this chapter is a published paper: Zhu, M., Park, J. and Sastry, A. M., 2011, "Particle Interaction and Aggregation in Cathode Material of Li-Ion Batteries: A Numerical Study", *J. Electrochem. Soc*., **158** (10), pp. A1155-A1159

aggregates via simulation can also help predict the impact of fracture on conductivity at the aggregate level.

In the research of self-assembly of colloidal particles, previous work has used Brownian dynamics simulations to model colloidal aggregation of monodispersed systems [3, 4, 5]. Binary systems which contain two types of ellipsoidal particles of different sizes have also been modeled using Brownian dynamics simulations. For example, in the work of Cerbelaud et. al. [6], the heteroaggregation of AlO particles (~200nm) and SiO nanoparticles (~12.5nm) was simulated, and it was reported that a suspension of AlO particles can be destabilized by a small amount of SiO particles, leading to the formation of aggregates. In these models, van der Waals energy and electrostatic energy are minimized while the parcicles execute Brownian motion, leading to the formation of stable aggregated networks. These Brownian dynamics simulation techniques developed for modeling colloidal aggregation can be applied to simulate the self-assembly process of the cathode particles of Li-ion batteries during cathode fabrication, although the particle shapes are limited to spheres only.

Given the experimental observation that the structure of the electrode materials strongly affects cell performance [1, 2], it will be potentially beneficial to understand and optimize the aggregation process of the electrode material structure through simulation. However, due to the complexity of electrode material interaction, a robust algorithm to simulate this interaction process and identify the key energetic drivers and aggregates characteristics has not yet been developed. In the present study our objectives are as follows:

1) develop a simulation algorithm to model the self-assembly process during electrode fabrication;
2) characterize the morphology of the self-assembled structures;
3) identify the effect of particle size, mass ratio and temperature on the morphology of the self-assembled structures

METHODS

1. Brownian dynamics simulation

We performed a Brownian dynamics simulation [6] to model the aggregation of CB and AM particles. The trajectory of the particles is governed by the Langevian equation

$$m_i \frac{d\mathbf{v}_i(t)}{dt} = -\zeta_i \mathbf{v}_i(t) + \sum_j \mathbf{F}_{ij}\left\{\mathbf{r}_{ij}(t)\right\} + \mathbf{\Gamma}_i(t) \quad (1)$$

where m_i is the mass of the i-th particle; $\mathbf{v}_i$ is the velocity of the i-th particle; $\mathbf{F}_{ij}$ is the force exerted on the i-th particle by the j-th particle; $\mathbf{r}_{ij}$ is the position vector from the j-th particle to the i-th particle; and $\zeta_i = 6\pi\eta a_i$ is the friction coefficient that depends on the solvent viscosity η, simulating Stokes' friction, which represents the only hydrodynamic interaction considered in this study. $\mathbf{\Gamma}_i(t)$ represents the interaction between CB and/or AM particles with surrounding PVDF-NMP solution molecules, obeying the following statistical properties

$$\left\langle \mathbf{\Gamma}_i(t) \right\rangle = 0, \text{ and } \left\langle \mathbf{\Gamma}_i(t)\mathbf{\Gamma}_j(t') \right\rangle = C\delta(t-t')\delta_{ij} \quad (2)$$

where $C = 2k_B T\zeta_i$ with k_B is the Boltzmann constant and T is temperature. The integration schemes are given by equation (3) and (4) [6], and time step size $\delta t = 4\times10^{-10}$s:

$$\mathbf{v}_i(t+\delta t)=\mathbf{v}_i(t)+\frac{\sqrt{2k_BT\zeta_i}}{m_i}(\delta t)^{1/2}\mathbf{Y}_i+\frac{1}{m_i}\left(-\zeta_i\mathbf{v}_i(t)+\sum_j\mathbf{F}_{ij}\{r_{ij}(t)\}\right)\delta t \tag{3}$$

$$\mathbf{r}_i(t+\delta t)=\mathbf{r}_i(t)+\mathbf{v}_i(t)\delta t \tag{4}$$

Note that $\frac{\sqrt{2k_BT\zeta_i}}{m_i}(\delta t)^{1/2}\mathbf{Y}_i$ is the random Brownian force term given by stochastic calculus. $\mathbf{Y}_i$ follows Gaussian distribution.

The DLVO (named after Derjaguin and Landau, Verwey and Overbeek) theory is employed [7] and the interaction between particles is viewed as the sum of two contributions: 1) attraction due to van der Waals forces U_{ij}^{wdW} and 2) electrostatic double layer interaction U_{ij}^{el} due to surface charges of the particles

$$U_{ij}^{DLVO}=U_{ij}^{vdW}+U_{ij}^{el} \tag{5}$$

The van der Waals contribution is represented as

$$U_{ij}^{vdW}(r_{ij})=-\frac{A_{ij}}{6}\left[\frac{2a_ia_j}{r_{ij}^2-(a_i+a_j)^2}+\frac{2a_ia_j}{r_{ij}^2-(a_i-a_j)^2}+\ln\left(\frac{r_{ij}^2-(a_i+a_j)^2}{r_{ij}^2-(a_i-a_j)^2}\right)\right] \tag{6}$$

where a_i and a_j denote the radius of particle i and j, and A_{ij} is the Hamaker constant that depends on the polarizability both of particles i and j and of the solvent.

The electrostatic contribution is represented as

$$U_{ij}^{el}(r_{ij})=\pi\varepsilon\frac{a_ia_j}{a_i+a_j}(\psi_i^2+\psi_j^2)\times\left[\frac{2\psi_i\psi_j}{\psi_i^2+\psi_j^2}\ln\left(\frac{1+e^{-\kappa h_{ij}}}{1-e^{-\kappa h_{ij}}}\right)+\ln(1-e^{-\kappa h_{ij}})\right] \tag{7}$$

where $\varepsilon=\varepsilon_0\varepsilon_r$ is the dielectric constant of the solvent; ε_r is the relative dielectric constant and ε_0 is permittivity of the vacuum; ψ_i is the surface potential of particle i;

$h_{ij} = r_{ij} - \left(a_i + a_j\right)$ is the surface-to-surface separation distance; and κ is the inverse Debye screening length $1\times10^{9}\text{m}^{-1}$ used in this simulation.

2. Simulation parameters

We model the formation of the electrode structure, with manganese oxide as the active material (AM), CB as the conductive additive, and PVDF as the polymeric binder. The CB and AM are modeled as spherical particles. CB particles are simulated with a diameter of 60nm, assuming they start from a very low level of agglomeration prior to the mixing process, and AM particles are simulated with a diameter of 0.5μm or 1μm in two different cases. PVDF binder is dissolved in an Anhydrous *N*-methylpyrrolidone (NMP) solution, forming a homogenous viscous medium.

The parameters of the constituents we used in this simulation can be found in Table 2.1. The Hamaker constant of CB is given as 2.53×10^{-19}J [8]. The surface energy of NMP γ_n=0.04J/m^2 [9] is used to calculate the Hamaker constant of NMP using equation $A = 24\pi\gamma_n D_o^2$ [8, 10], and the Hamaker constant is found to be 8.21×10^{-20}J. The Hamaker constant between manganese oxide and Si_3N_4 in an aqueous solution is 2.4×10^{-19}J [11], and the Hamaker constant for water is 3.7×10^{-20}J [12, 13]. Furthermore, the Hamaker constant of Si_3N_4 is given as 2.53×10^{-19}J [14], and the Hamaker constant of manganese oxide is then calculated from equation (8) to be 1.59×10^{-18}J.

$$A_{132} = \left(\sqrt{A_{11}} - \sqrt{A_{33}}\right)\left(\sqrt{A_{22}} - \sqrt{A_{33}}\right) \tag{8}$$

where A_{132} is the Hamaker constant between manganese oxide and Si_3N_4 in an aqueous solution, A_{11}, A_{22} and A_{33} are the Hamaker constants for manganese oxide, Si_3N_4 and water, respectively.

Material	diameter [µm]	density [g/cm^3]	Hamaker constant [J]	relative dielectric constant	Zeta potential
CB	0.06	2.0	2.53e-19	-	-50mV
MnOx	0.5-1.0	4.0	1.59e-18	-	-30mV
NMP	-	-	8.21e-20	32.2	-

Table 2.1: Parameters associated with the electrode materials

From equation (8), we calculated the Hamaker constant in NMP for CB-CB, manganese oxide-manganese oxide, and CB-manganese oxide, which are 4.69×10^{-20}J, 9.5×10^{-19}J, and 2.11×10^{-19}J, respectively.

The zeta potentials for the particles are -50mV for CB [15] and -30mV for manganese oxide [16]. In our simulation, we take the zeta potential as the surface potential of CB and manganese oxide particles. NMP has a relative dielectric constant of 32.0 [17] and a viscosity of 1.67mPa*s.

CB and AM particles are initiated at random positions in this PVDF-NMP medium, simulating the initially homogenized system. The Brownian dynamics simulation [6, 18] is then employed, and CB and AM particles are allowed to form aggregates in the PVDF-NMP medium until a stable structure is established.

The CB and AM particles are both simulated as spheres with densities of $2g/cm^3$ and $4g/cm^3$, respectively. 60nm is used as the diameter for CB; in the simulations we varied the diameters of AM particles from 0.5μm to 1.0μm. The mass ratio for CB and AM is 1:23 and 1:11. The volume fraction of the total solid phase (CB, AM and PVDF solid) in the simulation domain is 50%, with PVDF dissolved in the solvent throughout the simulated process and excluded from the solid phase. In this work, 10 AM particles are simulated inside the domain with period boundary conditions. The size of the simulation domain and the number of CB particles are calculated from the solid volume fraction and mass ratio of CB/AM. The number of CB particles is 629, 1315, and 5032, respectively, for the cases with AM particle size 0.5μm and 1.0μm. Table 2.2 shows the parameter matrix that we explored in this work.

Mass ratio (CB:AM)	AM size	Temperature
4%:92%	1.0µm	298K
		308K
		328K
	0.5µm	298K
		308K
		328K
8%:88%	0.5µm	298K
		308K
		328K

Table 2.2: System parameters

Figure 2.1 shows the normalized potential energy plotted against the normalized separation distance (surface distance) between different particles (in the case where the AM particle diameter equals 0.5μm). From the monotonies of these curves we conclude that despite the repulsive electrostatic interactions between particles, the overall forces are attractive due to the contribution of the van der Waals interaction. We set up the potential cut-off distance at the points where interaction forces are negligible. The potential cut-off distance (from center to center) is 1.8 times the diameter of a single CB particle for CB-CB interaction, 1.2 times the diameter of a single AM particle for AM-AM interaction, and 0.6 times the diameter of a single AM particle for CB-AM interaction. A Verlet neighbor list with a radius of 2.2 times the cut-off distance was created as illustrated in Figure 2.1(d). The list was updated once the displacement of any particle became greater than half of this radius. At short range, the magnitude of the attractive force increased toward infinity, which is not realistic and in our numerical simulation would lead to particle overlapping. To avoid overlapping, the DLVO force curve was cut off at a short separation distance (1% the diameter of a CB particle for CB-CB interaction; 1% the diameter of an AM particle for AM-AM interaction; and 0.1% the diameter of an AM particle for CB-AM interaction) and replaced by a force that decreases with decreasing separation distance and changes into a strong repulsive force when overlapping occurs. The form of this force was determined so that two approaching particles could come into contact with negligible overlapping and vibration, which we observed did not affect the configuration of the particle cluster.

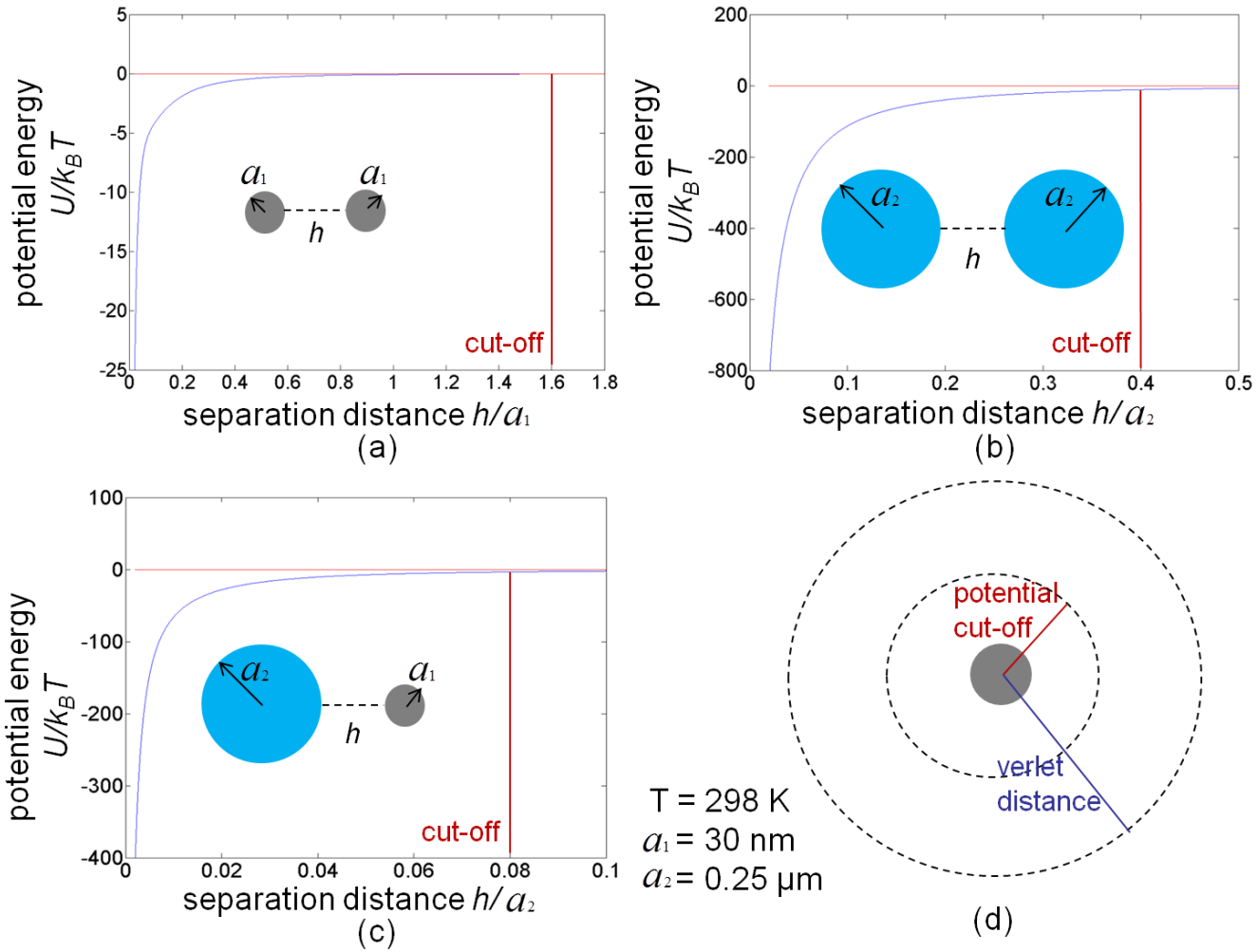

Figure 2.1: Schematics of potential energy drop-off and interaction distances. a) CB-CB; b) MnO_x-MnO_x; c) CB-MnO_x;d) potential cut-off and Verlet distance

3. Key factors and aggregates characterization

We employed a design of experiment to study the effect of key factors (temperature, particle size, and mass ratio) on the aggregate geometry. We assigned the temperature to 3 levels: 298K, 308K, and 328K. The size of the AM particles ranged from 0.5μm to 1.0 μm, and CB/AM mass ratio ranged from 4%:92% to 8%:88%. We performed 5 simulation runs for each combination, and characterized the resulting aggregates in terms of the number of CB particles connected to AM particle clusters. In all simulation cases, the AM particle number and solid volume fraction were constant.

We selected the parameters for the following reasons: 1) temperature has a considerable influence on the magnitude of Brownian forces, which helps the particles overcome local minima and achieve an energetically favorable (stable) state; on the other hand, high temperature can also cause bonds between particles to break due to large random motion; 2) the size of AM particles has a large influence on the performance of batteries (optimizing for energy or power), and particle size also affects the magnitude of forces exerted on surrounding particles; and 3) the CB is an additive that improves conductivity—it is desirable to optimize the mass ratio of CB and AM in order to achieve greater conductivity with minimal added mass.

The aggregates generated using the above-mentioned simulation algorithm were characterized in order to identify the key parameters that determine the final structure geometry.

In our simulation, we recorded whether each pair of particles was connected or not. Using this information, we built a cluster list in which the connected particles were grouped in the same cluster. In order to improve the conductivity of the electrode

material, the connection between CB particles and AM particle clusters is an important parameter. At a given CB content, it is reasonable to assume that the more CB particles are connected to AM particle clusters, the bigger contribution they make to the improvement of conductivity of the cathode system. Therefore, we characterize the aggregated system by the percentage of CB particles connected to the AM particles using the cluster list we found.

RESULTS

Final configuration – A representation of the final configuration obtained through Brownian dynamics simulation is shown in Figure 2.2. The blue (larger) spheres represent AM particles, while the red (smaller) spheres represent CB particles. AM particles occupy the most volume within the domain due to their larger size; they form a percolated network. The CB particles are connected to AM particles by means of attractive forces. Also, relatively short-range attractive forces between CB particles form local clusters among them. These clusters are attracted to the AM particle network, improving conductivity of the electrode. Fundamentally, the configurations of the system are determined by the combination of interactions due to van der Waals force, electrostatic force, and random forces. Temperature also plays an important role in determining the system structure. Brownian motion, which is temperature dependent, can shake the CB and AM particles to prevent the system from being trapped into a local minimum.

Effect of temperature – For AM particles with a diameter of 0.5μm and 1.0μm, and for systems with a CB/AM mass ratio of 4%:92% and 8%:88%, the percentage of CB

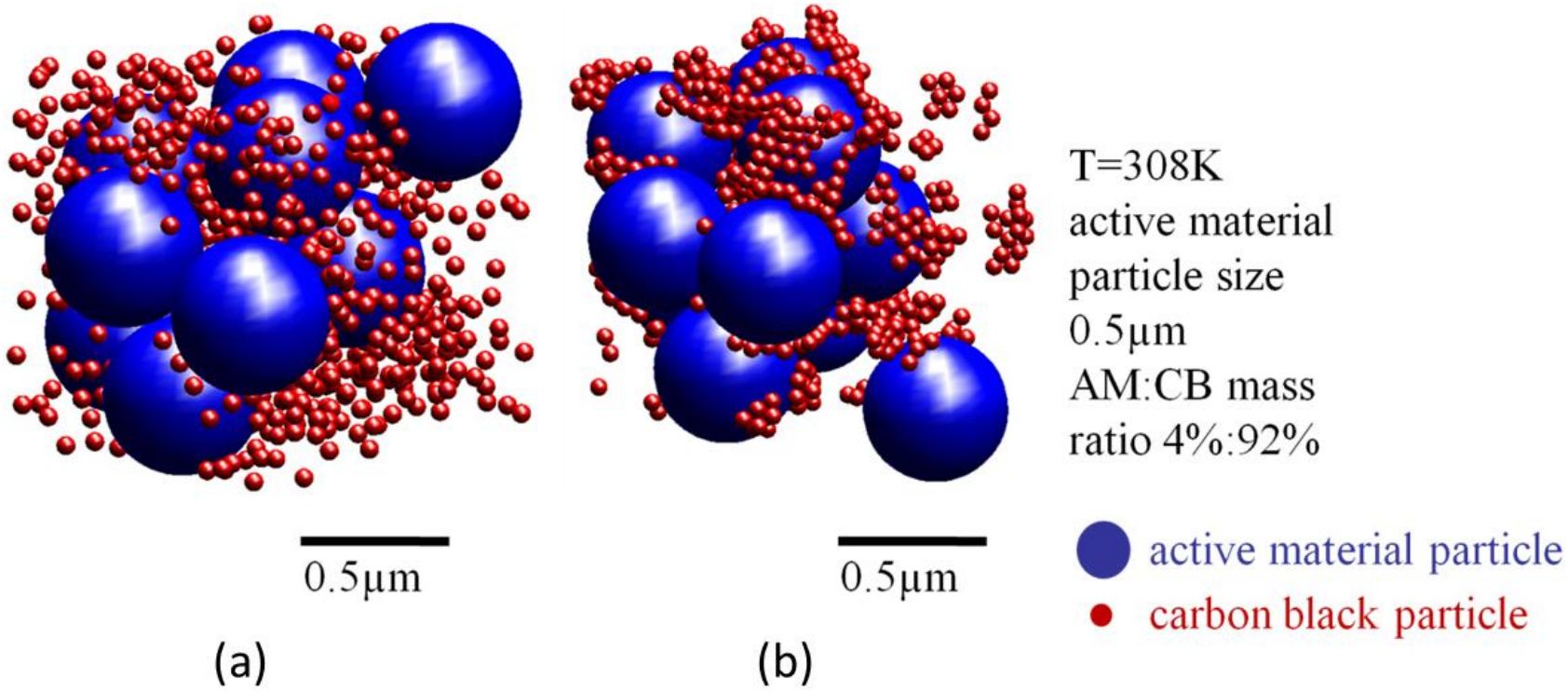

Figure 2.2: Cathode particle cluster : (a) random initial configuration;
(b) configuration after Brownian dynamics simulation

particles (out of a total of 629, 1315 or 5032 CB particles being simulated) connected to the cluster of aggregated AM is plotted against different temperature levels in Figure 2.3. Our simulation results show that when temperature increases, the percentage of CB particles connected to AM clusters increases for cases with AM particles 1 μm in diameter (Fig. 4(b)). However this percentage decreases for AM particles with a diameter of 0.5 μm (Fig. 4(a) and 4(c)). The P-value for the null-hypothesis (that there is no difference in mean for samples from cases with different temperature levels) is small (0.0085 and 1.34e-7) for the two cases with a CB/AM mass ratio 4%:92% (Fig. 4(a) and 4(b)), indicating a significant correlation between temperature and CB connection. However, for cases with a CB/AM mass ratio of 8%:88% (Fig. 4(c)), the P-value is found to be larger (0.073), indicating a weaker correlation. Our explanation for cases with AM particle size 1.0 μm is that the increase in temperature increases the Brownian motion of particles and enhances their ability to overcome the energy barrier and minimize potential. However, for cases with an AM particle size 0.5 μm, Brownian motion becomes more significant with increased temperature due to the weaker attraction forces between AM particles and CB particles. This results in easier bond separation.

Effect of AM particle size – When particle size increased from 0.5 μm to 1.0 μm and the mass ratio of CB and AM were kept constant (4%:92%), the percentage of CB particles connected to AM particles (averaged across all temperature values) increased from 25.0% to 43.2%. The larger AM particle size increases the attraction force to CB particles, and thus increases the percentage of CB particles connected to the AM cluster.

Effect of CB/AM mass ratio – When the AM particle size is kept at 0.5 μm and the mass ratio of CB and AM is increased from 4%:92% to 8%:88%, the percentage of

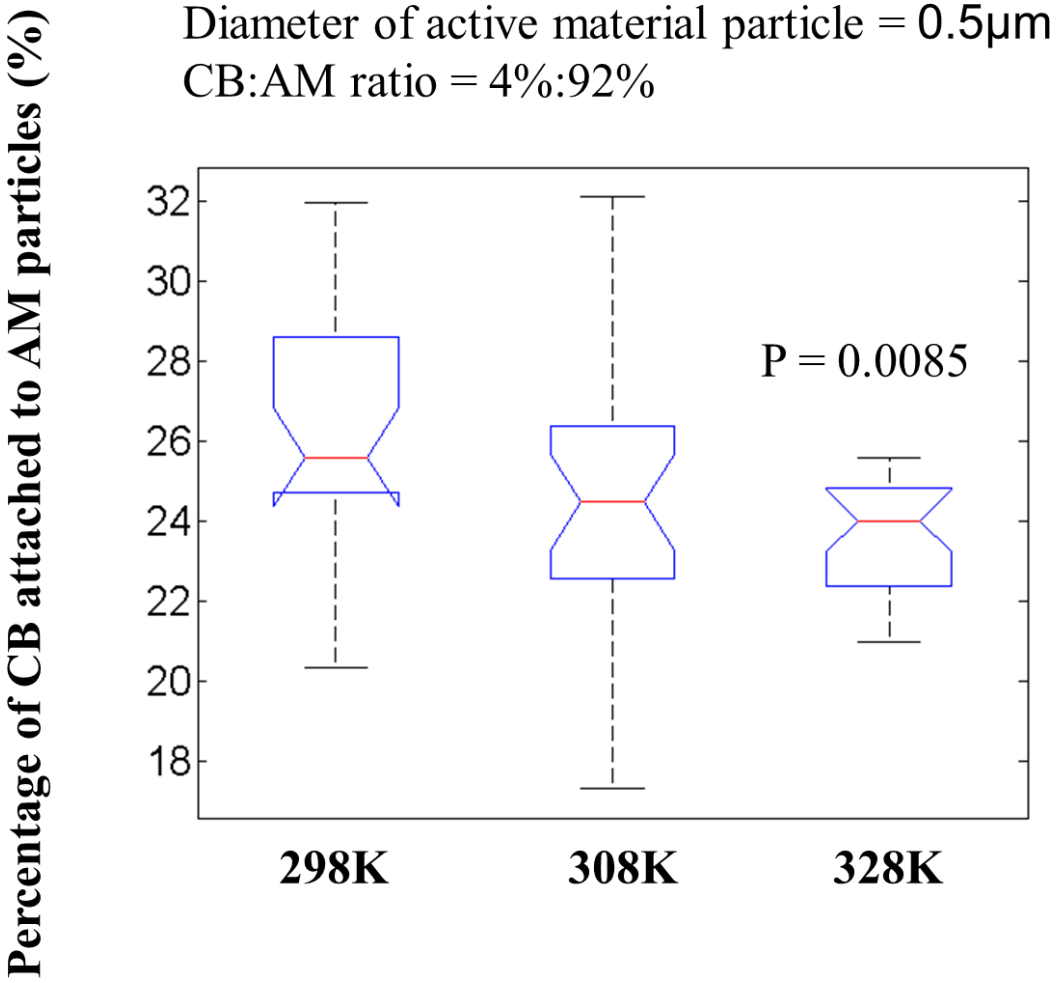

Figure 2.3 (a): Number of CB connected to AM cluster plotted against temperature

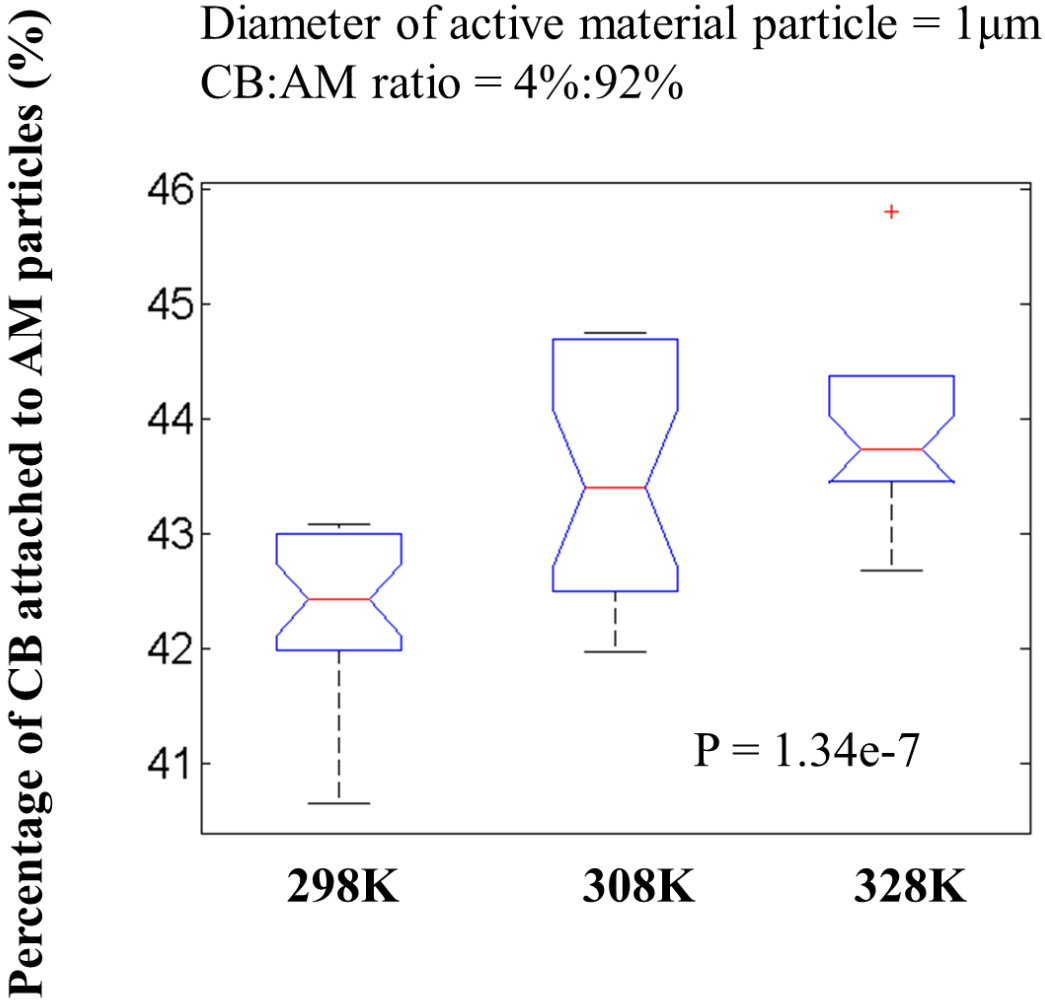

Figure 2.3 (b): Number of CB connected to AM cluster plotted against temperature

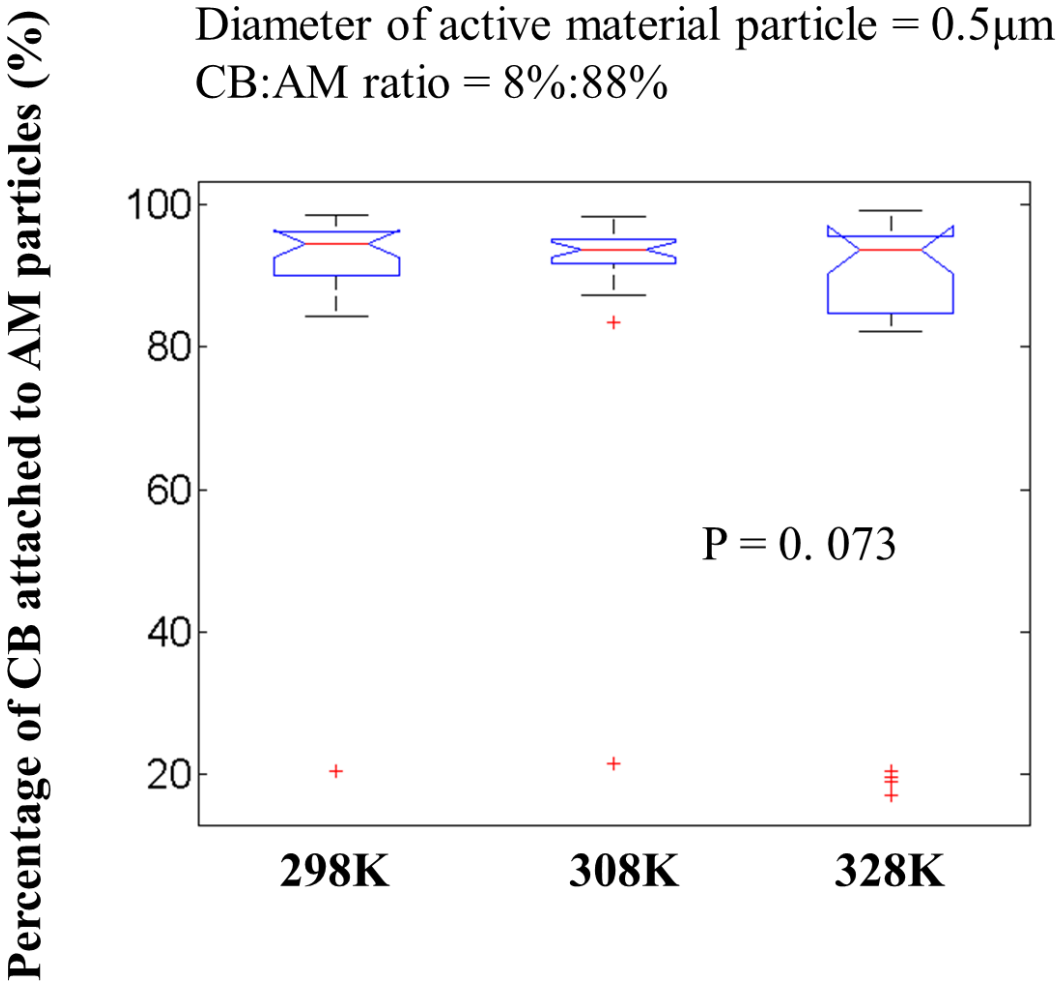

Figure 2.3 (c): Number of CB connected to AM cluster plotted against temperature

CB connection (averaged across all temperature values) increases from 25.0% to 86.4%. The larger CB mass ratio increases the probability for CB particles to interact among themselves and interact with AM particles, thus improving the conductive network by increasing the CB connection rate.

DISCUSSION

Brownian dynamics simulation has served as a tool for modeling interactions between colloids; however, this is the first work to utilize this tool to investigate the characteristics of aggregates in a Li-ion battery cathode system. In this work, the cathode aggregation process of Li-ion batteries is simulated to find the relative position of different particles, which is the first step in providing insight into optimizing battery cathodes. We have demonstrated the trend between CB connection percentage and particle size, mass ratio, and temperature.

The aggregated structure produced by this simulation method can also be used to perform further fracture analysis on aggregated clusters. Although experimental methods such as focused ion-beam (FIB) cross-sectioning [19, 20] can also be used to generate images that reveal the morphology of the cathode structure, the method presented in this chapter provides the capability to adjust input parameters and generate different characteristics structures, thus providing insight into the effect of these parameters on the fracture behavior of cathode clusters.

One of the limitations of this work is that only spherical particles are considered in the Brownian dynamics simulation. The method is not readily extendable to more

generally shaped particles, since no analytical solution is available for interaction forces between generally shaped particles other than spheres.

BIBLIOGRAPHY

[1] Liu, G., Zheng, H., Simens, A. S., Minor, A.M., Song, X. and Battaglia, V. S., 2007, "Optimization of acetylene black conductive additive and PVDF composition for high-power rechargeable lithium-ion cells", *Journal of The Electrochemical Society,* **154** (12), pp. A1129-A1134

[2] Liu, G., Zheng, H., Kim, S., Deng, Y., Minor, A. M., Song, X. and Battaglia, V. S., 2008, "Effects of Various Conductive Additive and Polymeric Binder Contents on the Performance of a Lithium-Ion Composite Cathode", *Journal of The Electrochemical Society*, **155** (12), pp. A887-A892

[3] Hutter, M., 2000,"Local Structure Evolution in Particle Network Formation Studied by Brownian Dynamics Simulation", *Journal of Colloid and Interface Science*, **231**, pp. 337–350

[4] Schenker, I., Filser, F. T., Aste, T., Gauckler, L.J., 2008, "Microstructures and mechanical properties of dense particle gels: Microstructural characterization", *Journal of the European Ceramic Society*, **28** ,pp. 1443–1449

[5] Hecht, M. and Harting, J. 2007, "Formation and growth of clusters in colloidal suspensions", *International Journal of Modern Physics C*, **18** (4), pp. 501-510

[6] Cerbelaud, M., Videcoq, A., Ablard, P., Pagnoux, C., Rossignol, F., and Ferrando, R., 2008, "Heteroaggregation between Al2O3 Submicrometer Particles and SiO2 Nanoparticles: Experiment and Simulation", *Langmuir* **24** (7), 3001-3008

[7] Elimelech, M., Gregory, J., Jia, X., Williams, R. A., 1995, *Particle Deposition and Aggregation: Measurement, Modeling and Simulation*, Butterworth-Heinemann: Oxford, England

[8] Dagastine, R. R., Prieve, D. C. and White, L. R., 2002, "Calculation of van der Waals forces in 2-dimensionally anisotropic materials and its application to carbon black", *Journal of Colloid and Interface Science*, **249**, pp. 78-83

[9] Keman D. M. and Blau, W. J., 2008, "Exploring the mechanisms of carbon-nanotube dispersion aggregation in a highly polar solvent", *EPL*, **83**, pp. 66009

[10] Cho, Y. K., Wartena, R., Tobias, S. M., Chiang, Y.-M., 2007, "Self-assembling colloidal-scale devices: selecting and using short-range surface forse between conductive solids", *Advanced Functional Materials*, **17**, pp. 379-389

[11] Na, C. and Martin, S. T., 2009, "Growth of manganese oxide nanostructures alters the layout of adhesion on a carbonate substrate" *Environ. Sci. Technol.*, **43**, pp. 4967-4972

[12] Hiemenz, P. C. and Rajagopalam, R., 1997, *Principle of Colloid and Surface Chemistry*, 3rd ed. CRC

[13] ASTM Standard D, Zeta Potential of Colloids in Water and Waste Water, American Society for Testing and Materials, 1985

[14] Jaiswal, R. P., Kumar, G., Kilroy, C. M., and Beaudoin, S. I., 2009, "Modeling and validation of the van der Waals force during the adhesion of nanoscale objects to rough surfaces: a detailed description", *Langmuir*, **25**(18), pp. 10612-10623

[15]Basch, A., Horn, R. and Besenhard, J. O., 2005, "Substrate induced coagulation (SIC) of nano-disperse carbon black in non-aqueous media: the dispersibility and stability of carbon black in N-methyl-2-pyrrolidinone", *Colloids and Surfaces A: Physicochem. Eng. Aspects*, **253**, pp. 155–161

[16] Fuerstenau, D. W. and Shibata, J., 1999, "On using electrokinetics to interpret the flotation and interfacial behavior of manganese dioxide", *Int. J. Miner. Process.*, **57**, pp. 205-217

[17] Masuda, T., Matsuki, Y. and Shimoda, T., 2009, "Spectral parameters and Hamaker constants of silicon hydride compounds and organic solvents", *Journal of Colloid and Interface Science*, **340**, pp. 298–305

[18] Allen, M. P. and Tildesley, D.J., 1987, *Computer Simulation of Liquids*, Clarendon, Oxford

[19] Massl, S., Kostenbauer, H., Keckes, J. and Pippan, R., 2008, "Stress measurement in thin films with the ion beam layer removal method: Influence of experimental errors and parameters", *Thin Solid Films*, **516**, pp. 8655-8662,

[20] Reyntjens, S., and Puers, R., 2001, "A review of focused ion beam applications in microsystem technology", *Journal of Micromechanics and Microengineering*, **11** (4), pp. 287,

CHAPTER III

INTERACTION AND AGGREGATION OF ELLIPSOICAL PARTICLES IN THE CATHODE

INTRODUCTION

In an effort to optimize the composition of the cathode to improve capacity and power density while keeping parasitic mass to a minimum, Brownian dynamics simulations with binary spherical particle system have been conducted and the effects of key parameters have been identified. However, the geometries of real particles in Li-ion battery electrodes generally depart from the purely spherical [1, 2, 3]. In order to study more general and therefor realistic cases of electrode particles, it is desirable to model the interaction between non-spherical particles.

In cases where pair-wise additive inverse power law potential (such as van der Waals energy) is considered, particle-particle interaction potential can be obtained by integrating over the volumes of the interacting bodies [4]. However, explicit expressions are only available for several simple geometries. The explicit expression of the interaction energy for ellipsoidal particles has not been formulated. Efforts have been made to obtain the value of the interaction energy using methods that are less computationally intensive than numerical integration over ellipsoid volumes. Empirical potential functions have been proposed for ellipsoids with certain types of interaction potential profiles [5]. When considering interaction based on pair-wise additive potential,

a boundary element method was also proposed [6] which converts the volume expression into surface integrals which are then calculated by discretizing the surface of the object into triangular elements. A perturbative expansion in the dielectric contrast is proposed which converges rapidly for particles at small separations [7]. Derjaguin's approximation has also been applied in colloidal aggregation simulation [8, 9, 10], greatly simplifying the calculation of interaction forces under the assumption that a relatively small region with a short distance between particle interfaces contributes almost all the interaction energy between the interacting convex particles. However, the approximation is only valid for an interaction distance several times smaller than the particle size. For long separation distances, the interaction energy quickly approaches zero; however, for intermediate ranges where the separation distance is comparable to the size of the interacting particles, the above-mentioned approximation diverges from the exact value, thus rendering the approximation unsuitable for the electrode particle aggregation process we are interested in.

A method that is both capable of accurately finding the interaction potential between generally shaped particles such as ellipsoids, and at the same time computationally efficient enough to be used during aggregation simulation, is not available from the literature, given the high computational cost associated with numerical integration and the limitations of the applicable ranges of the approximation method. In this work, therefore, our objectives are as follows:

1) develop a simulation algorithm to model the self-assembly process for non-spherical particles during electrode fabrication;

2) develop a fast approach to finding interaction energy between ellipsoidal and spherical particles;
3) characterize the self-assembled structures and identify the effect of particle aspect ratio

METHODS

1. Monte Carlo simulation

We performed a Monte Carlo simulation to model the aggregation of CB and AM particles. Periodical boundary conditions were applied to the simulation cell. In order to achieve the desired packing density, we employed a concurrent construction method to generate the initial configuration of ellipsoidal particles [11, 12, 13], which process is similar to molecular dynamics except for a few major differences. Particle generation starts with a collection of randomly dispersed ellipsoidal particles which are 1/1000 the size of the actual simulated particle. The particles are assigned random initial translational and rotational velocities and are allowed to elastically collide with each other. As time progresses, the particles enlarge uniformly at a rate of $a(t)$. When particles collide, momentum transfer occurs. Since we are only interested in generating a relatively densely packed initial configuration for further simulation, several simplifications are made in the collision algorithm to reduce computational cost at this stage. We simplified the linear momentum transfer between ellipsoids using the model of equal spheres. The translational velocities of two particles (number 1 and 2) are denoted $\mathbf{V}_1$ and $\mathbf{V}_{2,}$ just before the collision. These two velocities were resolved into parallel (p)

and transverse (*t*) components with respect to the line of particle centers as shown in Figure 3.1:

$$\mathbf{V}_1 = \mathbf{V}_1^{(p)} + \mathbf{V}_1^{(t)} \tag{1}$$

$$\mathbf{V}_2 = \mathbf{V}_2^{(p)} + \mathbf{V}_2^{(t)} \tag{2}$$

The transverse velocity components remain unchanged after impact, whereas the parallel components changed places with a modification in magnitude by *h*. V_1^* and V_2^* denote the velocities just after impact.

$$\mathbf{V}_1^* = [\mathbf{V}_2^{(p)} + h\mathbf{u}_{12}] + \mathbf{V}_1^{(t)} \tag{3}$$

$$\mathbf{V}_2^* = [\mathbf{V}_1^{(p)} - h\mathbf{u}_{12}] + \mathbf{V}_2^{(t)} \tag{4}$$

where $\mathbf{u}_{12}$ is the unit vector:

$$\mathbf{u}_{12} = \frac{(\mathbf{r}_1 - \mathbf{r}_2)}{|\mathbf{r}_1 - \mathbf{r}_2|} = -\mathbf{u}_{21} \tag{5}$$

and the particle size growth rate is represented as:

$$h = \frac{da(t)}{dt} \tag{6}$$

As for the rotational velocities of the two ellipsoidal particles, ω_1 and ω_2, a physically realistic collision model will require the determination of contact points at the surface of each ellipsoid in order to determine the changes in rotational velocity based on rigid body motion. For the purpose of this work, a simplification is made and random rotational velocities are assigned to the two particles after collision. If the new rotational velocities result in particle overlapping at the next simulation time step, they are rejected and a new value is assigned until no overlapping occurs at the next time step.

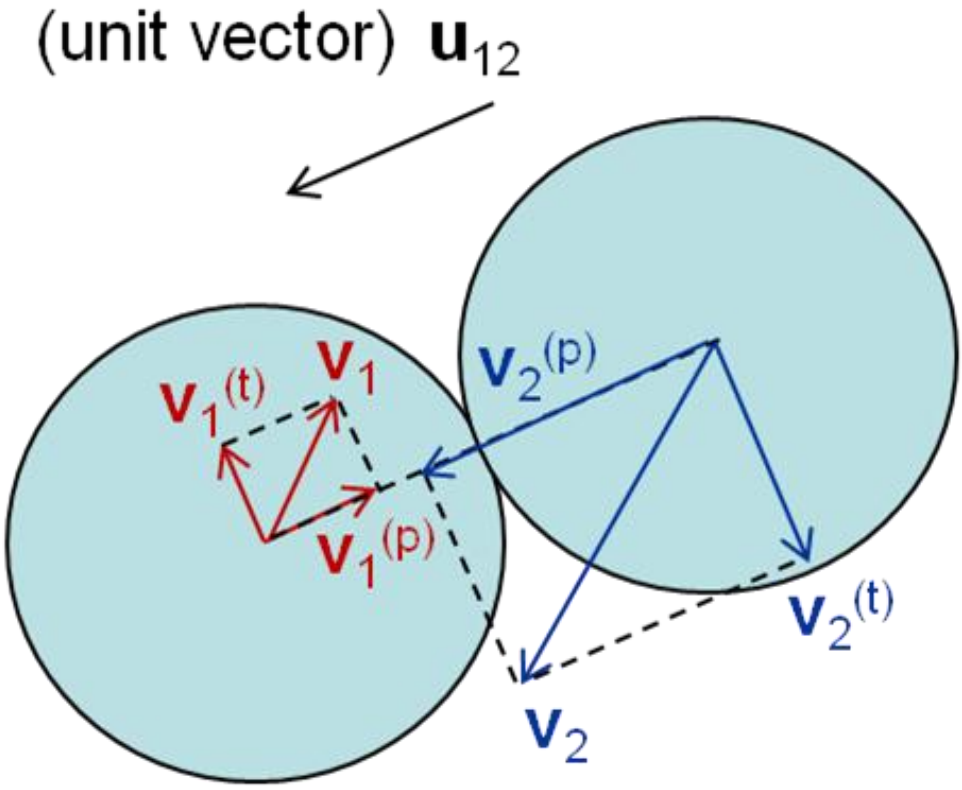

Figure 3.1: Velocity components for two particles (simplified as spheres)

After the larger ellipsoidal active material particles are generated, they are subject to Monte Carlo simulation until a stable configuration is achieved. Next, smaller carbon black particles are randomly placed in the simulation cell and execute Monte Carlo movements until a stable configuration is reached. With each move, a single particle is randomly selected and displaced. The magnitude and direction of the translational displacement is randomly assigned based on Gaussian distribution. For an ellipsoidal particle, another vector is added to the unit vector representing the orientation of the axis of revolution. The magnitude and direction of the added vector is also randomly assigned based on Gaussian distribution. The new orientation vector is then normalized. If the moved particle overlaps with any other particle, the move is rejected and the algorithm repeats the previous procedures by selecting a new particle and performing a trial move. If no overlapping is detected, the change in energy for the entire system is calculated, and the Monte Carlo move is accepted based on a probability as follows:

$$\mathrm{P(accept)} = \begin{cases} \exp\left(-\dfrac{E_{new} - E_{old}}{k_B T}\right); & if \quad E_{new} > E_{old} \\ 1 \qquad\qquad\qquad\quad ; & if \quad E_{new} \le E_{old} \end{cases} \tag{7}$$

where P(accept) is the probability that the Monte Carlo move will be accepted; E_{new} is the energy of the new configuration after the Monte Carlo move; E_{old} is the energy of the old configuration; k_B is the Boltzmann constant; and T is the absolute temperature.

Throughout the Monte Carlo simulation, we use an overlapping detection algorithm to check whether the two ellipsoids overlap with each other, and reject the Monte Carlo move if overlapping occurs. The algorithm was developed for ellipsoids of revolution with equal size [14, 15], which is suitable for the particle system we simulate in this work. The necessary and sufficient condition for the two ellipsoids to have no real

point in common or to be exteriorly tangent is that the functions Φ, S_1 and S_2 be positive or zero, and at least one among g_1, g_2 and m be negative.

$$g_\alpha = 4 + \left[\left(\frac{a}{b}\right) - \left(\frac{b}{a}\right)\right]^2 (\mathbf{u}_1 \times \mathbf{u}_2)^2 - \left(\frac{r^2}{b^2}\right) + \left[\left(\frac{1}{b^2}\right) - \left(\frac{1}{a^2}\right)\right](\mathbf{r} \cdot \mathbf{u}_\alpha)^2 \tag{8}$$

$$m = g_1 + g_2 - 2 - \left(\frac{1}{b^2}\right)\left[\left(\frac{a}{b}\right) - \left(\frac{b}{a}\right)\right]^2 (\mathbf{u}_1, \mathbf{u}_1, \mathbf{r})^2 \tag{9}$$

$$p = -m \tag{10}$$

$$q = g_1 g_2 - 4 \tag{11}$$

$$w = 4m - g_1^2 + g_2^2 \tag{12}$$

$$\phi = 4(p^2 - 3q)(q^2 - 3wp) - (9w - pq)^2 \tag{13}$$

$$S_1 = m^2 - 2g_1 g_2 - 4 \tag{14}$$

$$S_2 = g_1^2 g_2^2 + 8g_1 g_2 - 2m(g_1^2 + g_2^2) \tag{15}$$

where $\mathbf{u}_1$ and $\mathbf{u}_2$ are the unit vectors of the axes of revolution for the two ellipsoids; a is the length of the semi-major axis, which is along the axis of revolution; b is the length of the semi-minor axis; $\mathbf{r}$ is the vector connecting the center points of the two ellipsoids; and α = 1,2.

2. Interaction energy look-up table

We employed the Hamaker Theory to find the interaction potential between two particles [4]. Assuming multibody forces are ignored, we considered the interactions to be pair-wise; the Gibbs free energy due to dispersion interactions can be expressed as:

$$\Delta G_{12}^{d} = -\int_{v_1} dv_1 \int_{v_2} \frac{\Lambda_{12}\rho_1\rho_2}{r_{12}^6} dv_2 \tag{16}$$

where Λ_{12} is the London coefficient for two different kinds of molecules, and ρ_1 and ρ_2 are the molecular number densities (molecules per unit volume)**.**

Interaction energy between two particles can be obtained by integration over their volumes. In the special case of two interacting spheres with equal radii a_0, the total free energy can be expressed as

$$\Delta G_{12}^{d} = -\frac{A_{12}}{6}\left[\frac{2a_0^2}{R^2 - 4a_0^2} + \frac{2a_0^2}{R^2} + \ln\left(1 - \frac{4a_0^2}{R^2}\right)\right] \tag{17}$$

where A_{12} is the Hamaker constant

$$A_{12} = \pi^2 \rho_1 \rho_1 \Lambda_{12} \tag{18}$$

However, for the interaction between the two ellipsoids of which the semi-axes are of different lengths, no algebraic form is available for the ΔG_{12}^{d} in Eq. 16. Numerical integration methods can be employed to calculate the value of interaction potential, but they are too computationally expensive to be incorporated in each time step of the Monte Carlo simulation. To accelerate the process of finding interaction potential, we developed a look-up table. We first parameterized the relative position and orientation of two particles and calculated the interaction potential over the entire range of these parameters. The interaction potential between two particles can then be obtained by interpolation using the look-up table.

In this work, active material particles are modeled as equal ellipsoids of revolution around the longer semi-axis, and carbon black particles are modeled as equal spheres.

As shown in Figure 3.2, for any two given ellipsoidal particles E_1 and E_2, a Cartesian coordinate system (X-Y-Z) is chosen so that the Y-axis is in line with the axis of revolution of E_1, and the origin of the coordinate system is located at the center point of E_1. The center point of ellipsoid E_2 is expressed with polar angles α, β, and distance r with respect to the coordinate system X-Y-Z. The directional vector of the axis of revolution of ellipsoid E_2 can be expressed by Euler angles φ and θ. Therefore, five parameters are required to describe the relative position between the two ellipsoids. In order to describe the relative position and orientation between one ellipsoid and one sphere, the Euler angles φ and θ are not necessary with the ellipsoid E_1 fixed at the origin of the X-Y-Z coordinate system and axis of revolution in line with the Y-axis, as shown in Figure 3.3. In this case, only three parameters (α, β and r) are required to describe the relative position of two particles.

Look-up tables are generated for the ellipsoid-ellipsoid and ellipsoid-sphere interactions, respectively. The range of parameters is listed in Table 3.1. Only positive values for the parameter range are listed here, since for combinations of parameters that include negative values an equivalent positive parameter combination can always be found using symmetry. The symbol a denotes the length of the longer semi-axis of the ellipsoid, a_{CB} is the radius of carbon black particles, and r_0 is the distance of closest approach between two particles at a given combination of α, β, φ and θ. The distance of closest approach is the distance between the centers of the particles when they are externally tangent; it is calculated with the algorithm developed by Zheng *et. al.* [16, 17].

The interaction potential ΔG_{12}^{d} is calculated according to Eq. 16 through numerical integration using Mathematica 7, and tabulated in the five-dimensional

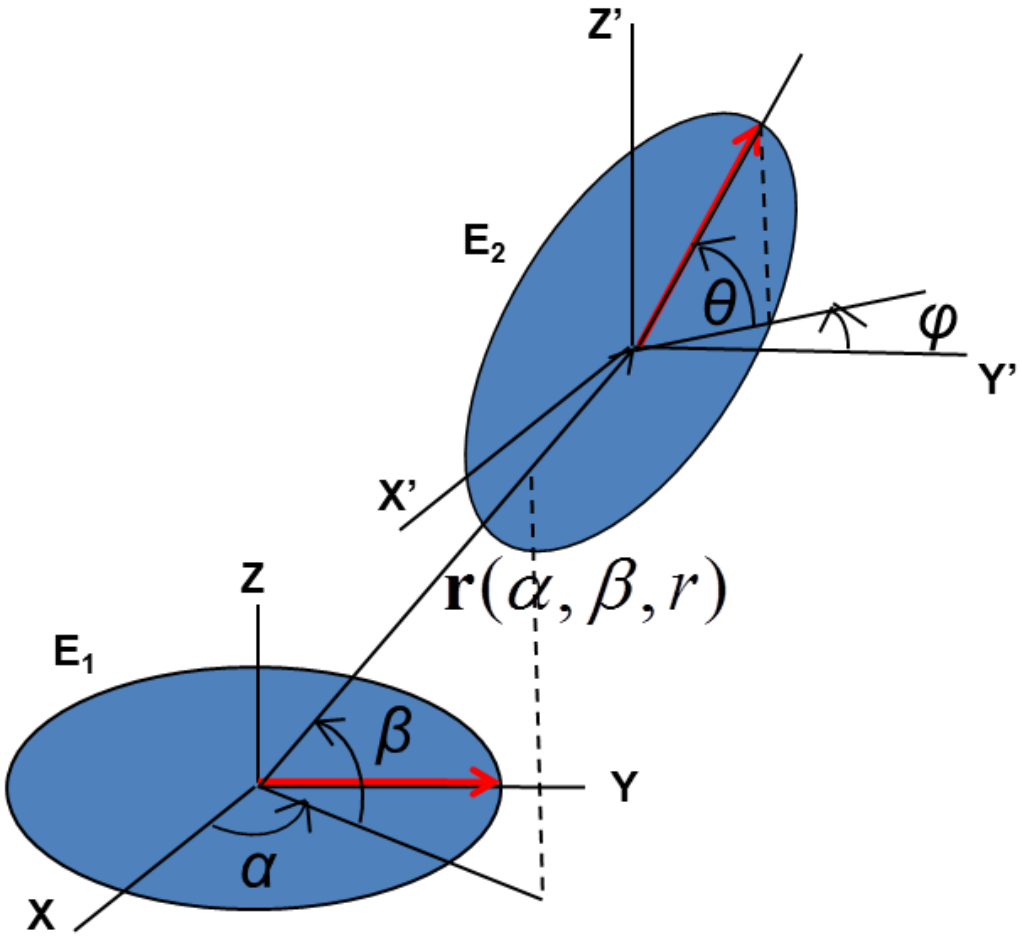

Figure 3.2: Relative position and orientation between two equal ellipsoids of revolution

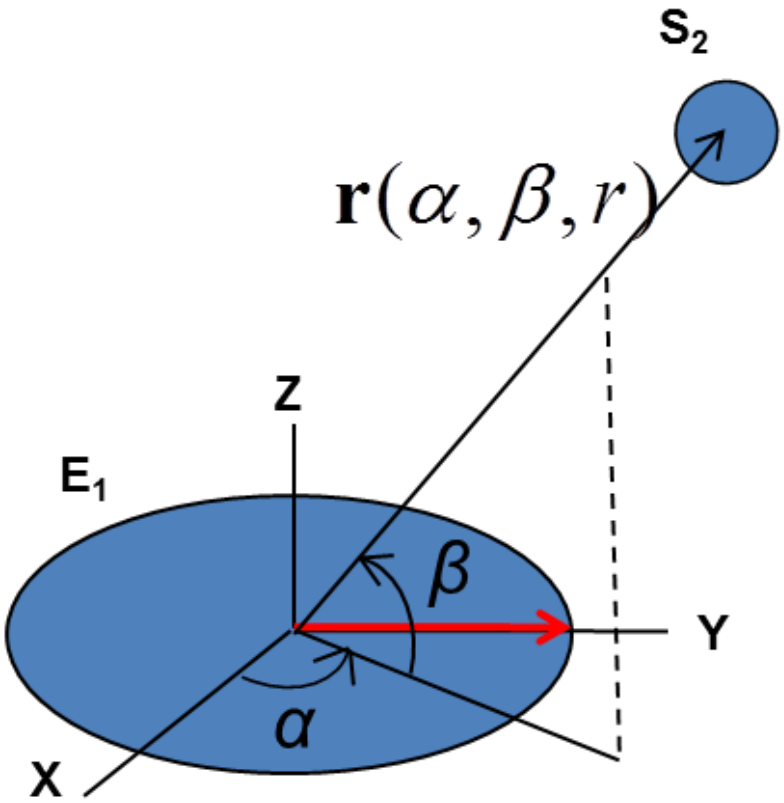

Figure 3.3: Relative position and orientation between one ellipsoid (E_1) and one sphere (S_2)

Parameter	Range	Number of intervals and increment
r	$1.01r_0 \sim 5a$	20 intervals, logarithmic scale
α	$0 \sim \frac{\pi}{2}$	15 intervals / an increment of $\frac{\pi}{30}$
β	$0 \sim \frac{\pi}{2}$	15 intervals / an increment of $\frac{\pi}{30}$
ϕ	$0 \sim \frac{\pi}{2}$	15 intervals / an increment of $\frac{\pi}{30}$
θ	$0 \sim \frac{\pi}{2}$	15 intervals / an increment of $\frac{\pi}{30}$

(a)

Parameter	Range	Number of intervals and increment
r	$1.01r_0 \sim 1.8(a + a_{CB})$	20 intervals, logarithmic scale
α	$0 \sim \frac{\pi}{2}$	64 intervals / an increment of $\frac{\pi}{128}$
β	$0 \sim \frac{\pi}{2}$	64 intervals / an increment of $\frac{\pi}{30}$

(b)

Table 3.1: Look-up table parameter range for (a) ellipsoid-ellipsoid and (b) ellipsoid-sphere interactions

parameter space for ellipsoid-ellipsoid interactions or three-dimensional parameter space for ellipsoid-sphere interactions. During the Monte Carlo simulation, the interaction potential is calculated for a given combination of relative position and relative orientation through interpolation, using 5 closest data points in each dimension of the parameter space. At distances shorter than the cut-off distance ($1.01\,r_0$ for AM-AM and AM-CB interaction, $1.001\,r_0$ for CB-CB interaction), the potential is replaced by a cut-off potential in order to avoid divergence in interaction energy.

3. Simulation parameters

We model the formation of the electrode structure, with manganese oxide as the active material (AM), carbon black (CB) as the conductive additive, and PVDF as the polymeric binder. AM particles are simulated as ellipsoids of revolution with a semi-major axis (axis of revolution) of 0.3969 μm and a semi-minor axis of 0.1984 μm. CB particles are simulated as spheres with a diameter of 60nm, assuming they start from a very low level of agglomeration prior to the mixing process. PVDF binder is dissolved in an Anhydrous *N*-methylpyrrolidone (NMP) solution, forming a homogenous viscous medium. The material properties of the constituents we used in this simulation can be found in Table 3.2 [18], where *d* is the diameter of a CB particle, and *a*, *b* and *c* are the semi-axes of an AM particle.

The mass ratio for CB, AM, PVDF is 4% : 92% : 4%. The volume fraction of the total solid phase (CB, AM, PVDF, after the NMP solvent evaporates) in the simulation domain is 50%. In this work, 20 AM particles are simulated inside the domain with periodic boundary conditions. The size of the simulation domain and the number of CB

Material	size [µm]	density [g/cm^3]	Hamaker constant [J]	relative dielectric constant
CB	d = 0.06	2.0	2.53e-19	-
MnOx	a = 0.3969 b = c = 0.1984	4.0	1.59e-18	-
NMP	-	-	8.21e-20	32.2

Table 3.2: Material properties associated with the electrode materials

particles are calculated from the solid volume fraction and mass ratio of CB/AM. The number of CB particles is 1258. The temperature is fixed at 298K.

4. Aggregated structure characterization

The aggregates generated using the above-mentioned simulation algorithm were characterized in terms of the amount of CB connected to the AM cluster.

In our simulation, we recorded whether each pair of particles was connected. Using this information, we built a cluster list in which the connected particles were grouped in the same cluster. The connection between CB particles and AM particle clusters is an important parameter, since only when conductive additives connect with active material do they contribute to the overall conductivity of the system. At a given CB content, it is reasonable to assume that the more CB particles are connected to AM particle clusters, the bigger contribution they make toward improving the conductivity of the cathode system. Therefore, we characterize the aggregated system by the percentage of CB particles connected to the AM particles, using the cluster list we found.

RESULTS

We conducted 5 Monte Carlo simulation cases containing ellipsoidal active material particles and compared the results with the simulation results for systems containing only spherical particles [7], which are presented in Chapter II. The spherical particles have the same volume as ellipsoidal particle in this case. CB:AM ratio and solid volume fraction are the same. Figure 3.4 shows a representation of the final stabilized configuration of the system containing ellipsoidal active material particles. The larger

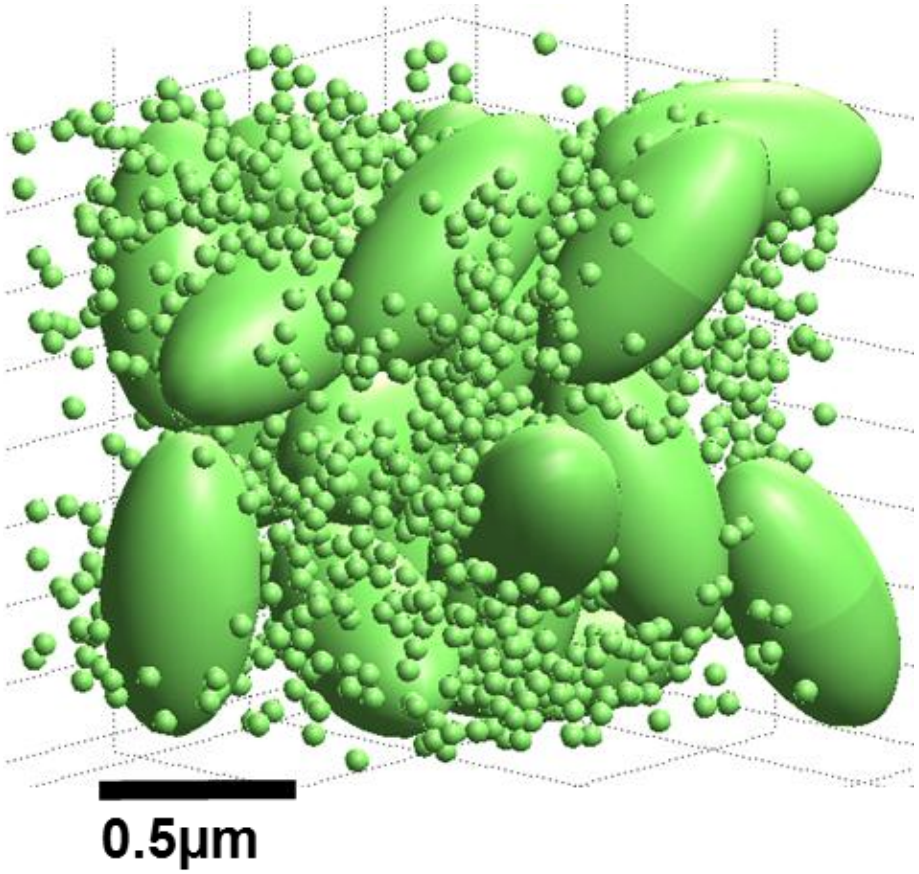

Figure 3.4: Representations of the final stabilized configuration for aggregates with ellipsoidal active material particles and spherical conductive additive particles

ellipsoids represent AM particles while the smaller spheres represent CB particles. In all cases, AM particles form a percolated network. The CB particles are connected to AM particles and also form local clusters among themselves. Some of these clusters are attracted to the AM particle network, contributing to the conductivity of the electrode.

The resulting aggregated structures are characterized, and the percentage of CB particles connected to the clusters of ellipsoidal AM particles (aspect ratio = 2) is plotted in Figure 3.5 and compared to the system containing spherical AM particles (aspect ratio = 1). The average percentage of CB particles attached to the ellipsoid AM particle cluster is found to be 42.5%, compared to 19.8% in cases where the AM particles are spherical.

DISCUSSION

The Monte Carlo method is used in this simulation instead of the Brownian dynamics used in the case of spherical particles. Capable of sampling energetically favorable configurations and extracting the information we are interested in, Monte Carlo method does not require the implementation of collision and momentum transfer between particles, which in this case involves complicated rigid body motion and interaction of ellipsoids (linear translation and rotation), thus drastically reducing the computational cost compared to Brownian dynamics for ellipsoidal particles. However, Brownian dynamics simulation handles the collective motion of particles better than the Monte Carlo, since the latter method only allows one particle to move at a time.

The implementation of a look-up table provides an accurate and efficient method of finding interaction energy for a generalized ellipsoid system, compared with the computationally intensive direct integration method and the approximation methods

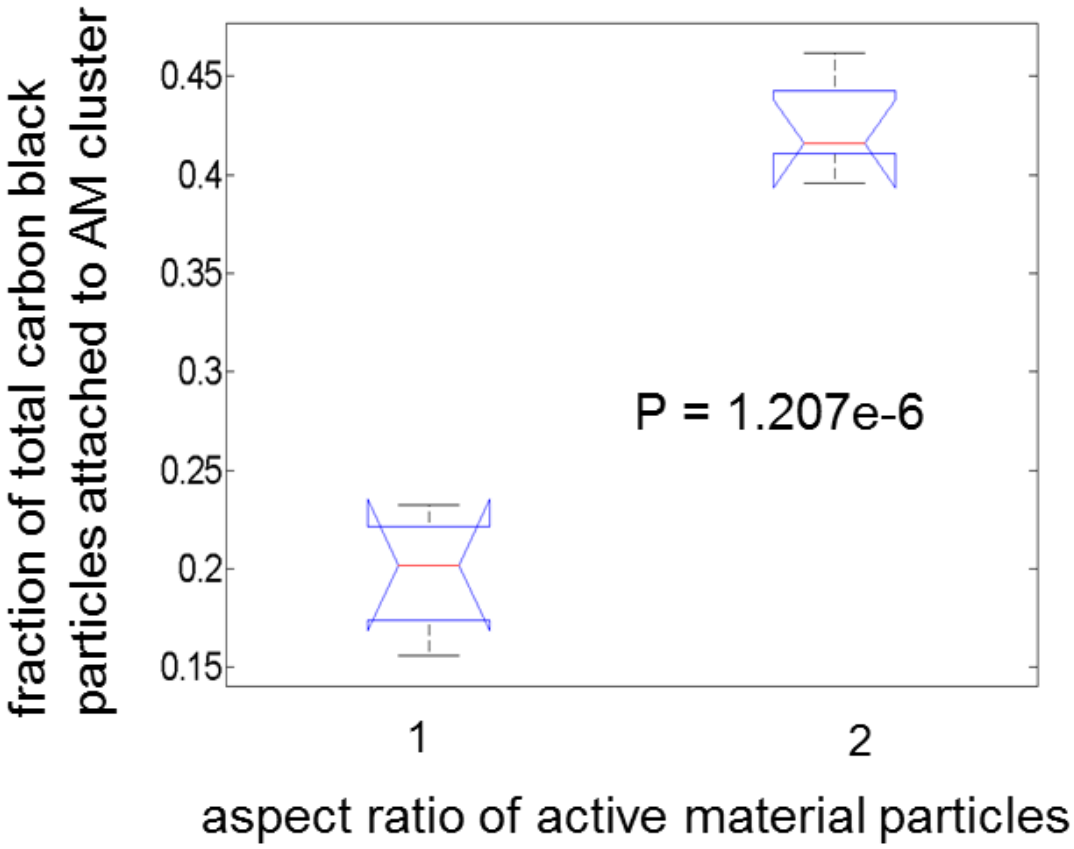

Figure 3.5: Number of CB connected to AM cluster for AM particle with different aspect ratio

which have only a narrow applicable range. The accuracy of this method can be further increased by increasing the resolution of the look-up table. This method also has the benefit of being readily extendable to different types of interaction potentials other than the pair-wise additive inverse power law potential discussed in this work. The limitation of this look-up table is that for each new aspect ratio a new look-up table needs to be generated. For a system containing N types of particles (different particle type means different material, aspect ratio and/or different size), a total of N! look-up tables need to be generated in advance. It is particularly impractical to implement in systems containing particles with continuously varying shapes and sizes.

In this chapter, the electrostatic double layer interaction potential is not considered. Van der Waals interaction is shown in Chapter II to be dominant; the electrostatic double layer contribution can be omitted.

BIBLIOGRAPHY

[1] Wang, H., Jang, Y.-I., Huang, B., Sadoway, D. R. and Chiang, Y.-M., 1999, "TEM Study of Electrochemical Cycling-Induced Damage and Disorder in LiCoO2 Cathodes for Rechargeable Lithium Batteries", *Journal of The Electrochemical Society*, **146** (2), pp. 473-480

[2] Lim, M.-R., Cho, W.-I., Kim, K.-B., 2001, "Preparation and characterization of gold-codeposited LiMn2O4 electrodes", *Journal of Power Sources*, **92**, pp. 168-176

[3] Wang, D., Wu, X., Wang, Z. and Chen, L., 2005, " Cracking causing cyclic instability of LiFePO4 cathode material", *Journal of Power Sources*, **140**, pp. 125-128

[4] Ross, S. and Morrison, I. D., 1988, *Colloidal Systems and Interfaces* , John Wiley & Sons, Inc

[5] Fejer, S. N., Chakrabartia, D. and Wales, D. J., 2011, "Self-assembly of anisotropic particles", *Soft Matter*, **7**, pp. 3553

[6] Veble, G., and Podgornik, R., 2007, "The boundary element approach to Van der Waals interactions", *Eur. Phys. J. E*, **23**, pp. 275–279

[7] Golestanian, R., 2005, "Lifshitz Interaction between Dielectric Bodies of Arbitrary Geometry", *Physical Review Letters*, **95**, pp. 230601

[8] Oversteegen, M. S. and Lekkerkerker, H. N. W., 2003, "Testing the Derjaguin approximation for colloidal mixtures of spheres and disks", *Physical Review E* **68**, pp. 021404

[9] Kruger, S., Mogel, H.-J., Wahab, M., and Schiller, P., 2011, "Depletion Force between Anisometric Colloidal Particles", *Langmuir*, **27**(2), pp. 646–650

[10] Schiller, P., Kruger, S., Wahab, M. and Mogel, H.-J., 2011, "Interactions between Spheroidal Colloidal Particles", *Langmuir*, **27**, pp. 10429–10437

[11] Moscinski, J., Bargiel, M., Rycerz Z. A. and Jacobs, P. W. M., 1989, "The Force-Biased Algorithm for The Irregular Close Packing of Equal Hard Spheres", *Molecular Simulation*, **3**, pp. 201-212

[12] Lubaehevsky B. D. and Stillinger, F. H., 1990, "Geometric Properties of Random Disk Packings", *Journal of Statistical Physics*, **60**(5/6), pp. 561

[13]Donev, A., Stillinger, F. H., Chaikin, P. M. and Torquato, S., 2004,"Unusually Dense Crystal Packings of Ellipsoids", *Physical Review Letters*, **92** (25), pp. 255506

[14] Yi, Y.-B. and Sastry, A. M., 2004, “Analytical approximation of the percolation threshold for overlapping ellipsoids of revolution”, *Proc. R. Soc. Lond.* A, **460**, pp. 2353-2380

[15] Vieillard-Baron, J., 1972, “Phase transitions of the classical hard-ellipse system”, *The Journal of Chemical Physics*, **56** (10), pp. 4729

[16] X. Zheng, and P. Palffy-Muhoray, 2007"Distance of closest approach of two arbitrary hard ellipses in two dimensions", *Phys. Rev. E*, **75**, pp. 061709

[17] X. Zheng, W. Iglesias and P. Palffy-Muhoray, 2009"Distance of closest approach of two arbitrary hard ellipsoids ", *Phys. Rev. E*, **79**, pp. 057702

[18] Zhu, M., Park, J., and Sastry, A. M., 2011, “Simulation of Particle Interactions in Cathode Material of Li-Ion Batteries”, *Journal of The Electrochemical Society*, **158** (10) pp. A1155-A1159

CHAPTER IV

FRACTURE ANALYSIS OF A SINGLE CATHODE PARTICLE[2]

INTRODUCTION

Local fractures in Li-ion batteries have been experimentally observed in several cathode materials [1, 2, 3]. Scanning electron microscope (SEM) images [2] have shown evident disruption on the surface of Li/Au-codeposited $LiMn_2O_4$ particles with a diameter of 20 μm cycled at a scan rate of 4mV/s, whereas no fracture was observed for a lesser scan rate of 0.1mV/s. This indicates that the propensity of fracture is related to current level and that fracture is more likely to occur during cycling at a higher C-rate. Experimentally [1], the capacity of $LiFePO_4$, cells has been shown to fade gradually from the initial 149mAh/g to 117mAh/g with a current density of 30mA/g at room temperature after 60 cycles. Both SEM and transmission electron microscope (TEM) techniques have been used to characterize the $LiFePO_4$ particles, and it has been shown that the particles cracked during cycling, possibly due to the high internal strain. The fracture of $LiFePO_4$ was proposed as one of the reasons for capacity fading in the cell under experiment. In other experimental work [3], $LiCoO_2$ particles were cycled 50 times between 2.5 and 4.35V at a current density of 0.4mA/cm^2. TEM results showed that local microstructural

[2] Material in this chapter is a published paper: Zhu, M., Park, J. and Sastry, A. M., 2012, " Fracture Analysis of the Cathode in Li-Ion Batteries: A Simulation Study", *J. Electrochem. Soc*., **159** (4), pp. A492-A498

and crystallograhic changes had occurred, although the cell was still electrochemically stable. Accumulated damage of this kind was proposed to be responsible for degradation in $LiCoO_2$-based batteries upon overcharging or after extended cycling. Fracture in $LiMn_2O_4$ particles has also been observed using various other techniques, including X-ray diffraction (XRD) [4,5] and acoustic emission spectroscopy [6].

One possible cause of fracture in battery materials is high stress. Stress can be induced in battery materials during fabrication, which usually involves compression to control the porosity of the cathode [7, 8, 9]; it can also result from cycling of the cells throughout the lifetime of the Li-ion batteries due to the intercalation of lithium ions as well as the transition of active material phases. In $Li_xMn_2O_4$ spinel systems, where $0<x<1$, the insertion and extraction of lithium into and out of the intersititial sites in the host Mn_2O_4 framework results in the expansion and contraction of the cubic lattice structure [10, 11]. A 6.5% volume change in the cubic phase of $Li_xMn_2O_4$ results from the intercalation of Li-ions when x changes from 0.2 to 0.995 [10]. An even larger volume change and stress level increase can be introduced by phase transition, at which time the $Li_xMn_2O_4$ material is further lithiated to $1<x<2$ and Jahn-Teller distortion occurs, resulting in 5.6% total expansion in unit cell volume [5, 12]. The stress caused by both the first order transition and Jahn-Teller distortion can contribute to local fracture in the active material of a battery cathode.

Several models have been developed to determine the stress generated by lithium intercalation and deintercalation. One-dimensional models [13, 14] have been developed to estimate stress generation in spherical electrode particles. Three-dimensional finite element simulations have also been developed to model diffusion-induced stress in

analogy to thermal stress [15, 16], and relationships have been established between stress levels within cathode particles and parameters such as current density, voltage and particle size. Analytical expressions have been constructed to capture the stress evolution in spherical electrode particles under galvanostatic or potentiostatic conditions [17, 18, 19] in an attempt to determine which operating conditions prevent cracking in electrodes. Stress generated in spherical particles that consider both diffusion and phase transition is calculated analytically and used to predict fracture [20]. A lithium insertion-induced fracture mechanism was employed in $LiFePO_4$ materials to predict cracking in two electrode phases without considering realistic particle geometry [21]. Further [22], an "electrochemical shock" model has also been proposed to calculate the conditions under which crack propagation develops from an initial semicircular defect on the surface of a spherical electrode particle. In this model, the driving force for the initial defect to crack is a tensile tangential stress at the particle surface.

However, no direct relationship between stress and fracture has been established for ellipsoidal particles of aspect ratios other than one, these being capable of more general and realistic cases for electrode particles. It remains to be investigated the geometric and electrochemical conditions under which initial defects further propagate and form larger fractures in the cathode materials under electrochemical reactions during charge/discharge cycles at different length scales (single cathode active material particles as well as aggregated network which consider active material particles and polymeric binders). In the present work, our objectives are as follows:

1) determine the effect of current density on the state of stress;

2) determine the effect of particle shape and size on the state of stress;

3) for both spherical and ellipsoidal particles, determine the range of the above-mentioned parameters under which the states of stress will result in fracture propagation; and

4) determine the effect of the initial defect location on fracture propagation

METHODS

Tensile stress is correlated to fracturing in cathode particles (in this case, the brittle material $LiMn_2O_4$) during cycling. In order to determine the conditions under which crack propagation occurs, three principal stresses σ_1, σ_2, and σ_3 were calculated using COMSOL Multiphysics simulation for particles without an initial defect during cycling. Their evolution during lithium intercalation and deintercalation was also captured. The three principal stresses were ranked in descending order, and the largest of the three—maximum principal stress—was denoted σ_1. In each case, the highest point of σ_1 was identified in the particle, and the maximum principal stress at that location was denoted $\sigma_{1,MAX}$. $\sigma_{1,MAX}$ rose to its peak before the charge/discharge process reached its end due to the reduction of the Li-ion concentration gradient in the later stage. The stress determines when $\sigma_{1,MAX}$ peaks were used in fracture simulations so as to capture the most severe conditions for crack propagation. These peak $\sigma_{1,MAX}$ in different simulation cases were ranked, and only the cases in which peak $\sigma_{1,MAX}$ exceeded 70% of the maximum tensile strength of $LiMn_2O_4$ were selected for further fracture simulation with ABAQUS. The threshold of 70% max tensile strength was selected to filter out the cases where crack propagation was unlikely. The fracture simulation used the calculated Li-ion

concentration profile as an input to evaluate the stress state for particles with initial defects and to determine whether crack propagation occurs.

Section 1 provides the governing equations and methodologies used in the 3D finite element analysis in this study; Section 2 explains the simulation setups and the range of parameters under study; and Section 3 describes the material properties used in the simulation.

1. Three-dimensional Finite Element Simulation

During the discharge of Li-ion cells, lithium inserts itself into the Mn_2O_4 host structure and occupies open tetrahedral sites. The diffusion of lithium into the Mn_2O_4 particle forms a concentration gradient profile that results in a stress field in the cubic $Li_xMn_2O_4$ phase. In this work, it was assumed that only a single cubic phase of $Li_xMn_2O_4$ existed in the particle, where $0<x<1$. The volume change in a single phase particle was solely attributable to the insertion and extraction of lithium to and from the interstitial sites in the Mn_2O_4 framework. In the simulations conducted, it was assumed that the onset of Jahn-Teller distortion in the spinel structure was prevented by charging and discharging the cell between $x=0$ and $x=1$ only.

The lithium intercalation-induced stress during cycling was calculated using an analogy to thermal stress [15, 16, 23], assuming that the lattice constants of the material changed linearly with the amount of ions inserted [10].

To obtain the concentration profile due to intercalation, the diffusion problem was solved together with the elastic field. The driving force for Li-ion diffusion can be

obtained by the gradient of the characteristic potential comprising the chemical and elastic energy of the system. The diffusion flux **J** is given by [15]

$$\mathbf{J} = -D\left(\nabla c - \frac{\Omega c}{RT}\nabla\sigma_h\right) \tag{1}$$

where c is the concentration of the Li-ions, D is the diffusion coefficient, Ω is the partial molar volume of Li-ion, R is a gas constant, T is absolute temperature, and σ_h is the hydrostatic stress.

Combining Eq. 1 with the mass conservation equation, $\partial c/\partial t + \nabla \cdot \mathbf{J} = 0$, we have

$$\frac{\partial c}{\partial t} = D\left(\nabla^2 c - \frac{\Omega}{RT}\nabla c \cdot \nabla\sigma_h - \frac{\Omega c}{RT}\nabla^2\sigma_h\right) \tag{2}$$

The initial condition is $c=c_o$, and the constant current boundary condition is

$$\mathbf{J} = -D\left(\nabla c - \frac{\Omega c}{RT}\nabla\sigma_h\right) = \frac{\mathbf{i_n}}{F} \tag{3}$$

where $\mathbf{i}_n$ is the current density on the particle surface and F is Faraday's constant.

The stress-strain relation with the existing concentration gradients can be written as

$$\varepsilon_{ij} = \frac{1}{E}\left[(1+\nu)\sigma_{ij} - \nu\sigma_{kk}\delta_{ij}\right] + \frac{\tilde{c}\Omega}{3}\delta_{ij} \tag{4}$$

where $\tilde{c} = c - c_0$ is the lithium concentration change from the original stress-free value, ε_{ij} and σ_{ij} are strain and stress components, E is Young's modulus, ν is Poisson's ratio, c is the Li-ion concentration, and δ_{ij} is the Kronecker delta. The last term accounts for the intercalation strain.

The problem was solved in three-dimensional space using FEMLAB (COMSOL Multiphysics). Two models were included in the multiphysics simulation: the PDE

(partial differential equation) model and the solid stress–strain model. In the PDE model, the diffusion process was described by the generalized form of Eq. 2. In the solid stress–strain model, "thermal expansion" was included as a load based on the variable of the concentration *c* instead of temperature in the thermal stress calculation.

The calculated Li-ion concentration profile was then exported to a fracture simulation model as an input condition. The fracture propagation was simulated using ABAQUS 6.9 standard with Extended Finite Element Method (XFEM), in which the elements that contained cracks were enriched [24]: the singularity around the tip of the crack was captured by the near-tip asymptotic functions and the discontinuous jump in displacement across the crack surfaces was represented by a discontinuous function. Fracturing was simulated with a damage-initiation rule based on maximum principal stress criterion, followed by a damage-evolution rule which considers the energy required for fracture to extend beyond the initiation of damage.

2. Design of Experiments

In this study, the effects of current density, particle size and particle shape on the stress state were investigated; whether or not the peak state of stress during charging/discharging resulted in fracture propagation was determined; and the effect of initial defect location on crack propagation was also examined.

Stress evolution – To find the evolution of the state of stress during cycling, a spherical particle with a radius of 7μm and without initial defect was subjected in the COMSOL Multiphysics simulation to both a charging and then a discharging process.

The surface current density was set to be $0.5A/m^2$ in both cases. The $\sigma_{1,MAX}$ was plotted against charge/discharge time.

Particle size and current density – Particle size and current density were considered two key parameters in this study because 1) variation of current density affects concentration gradient, which in turn affects the amount of volume expansion; and 2) variation in size also affects the amount of volume expansion, which in turn determines the stress level inside a particle. This study focused on the discharge process because discharging rates for Li-ion batteries are often higher than the charging rates in real world applications per manufacturer recommendations and thus require more attention. The radii of the spheres ranged from 1μm to 9μm. For each particle radius, the surface current density was varied from $0.1A/m^2$ to $0.6A/m^2$, with an increment of $0.1A/m^2$. For each case, the peak $\sigma_{1,MAX}$ was found for particles without defect via COMSOL, and the calculated Li-ion concentration profiled was exported to the ABAQUS fracture simulation. In the ABAQUS model, the initial crack was disk-shaped with a diameter 1/10 of that of the sphere; it was located in the center of the particle as shown in Figure 4.1, where the highest maximum principal stress was found during discharge. The range of these parameters is summarized in Table 4.1.

Particle aspect ratio - Besides these two parameters, aspect ratio (α) is also an important geometric factor that affects the stress level of Mn_2O_4 particles [15, 16, 25]. Since the real battery electrodes are generally composed of irregularly shaped particles, ellipsoidal particles with aspect ratios other than one are more general and more realistic representations of irregular electrode particles. In order to study the effect of particle aspect ratio and surface current density on fracture propagation, particles with aspect

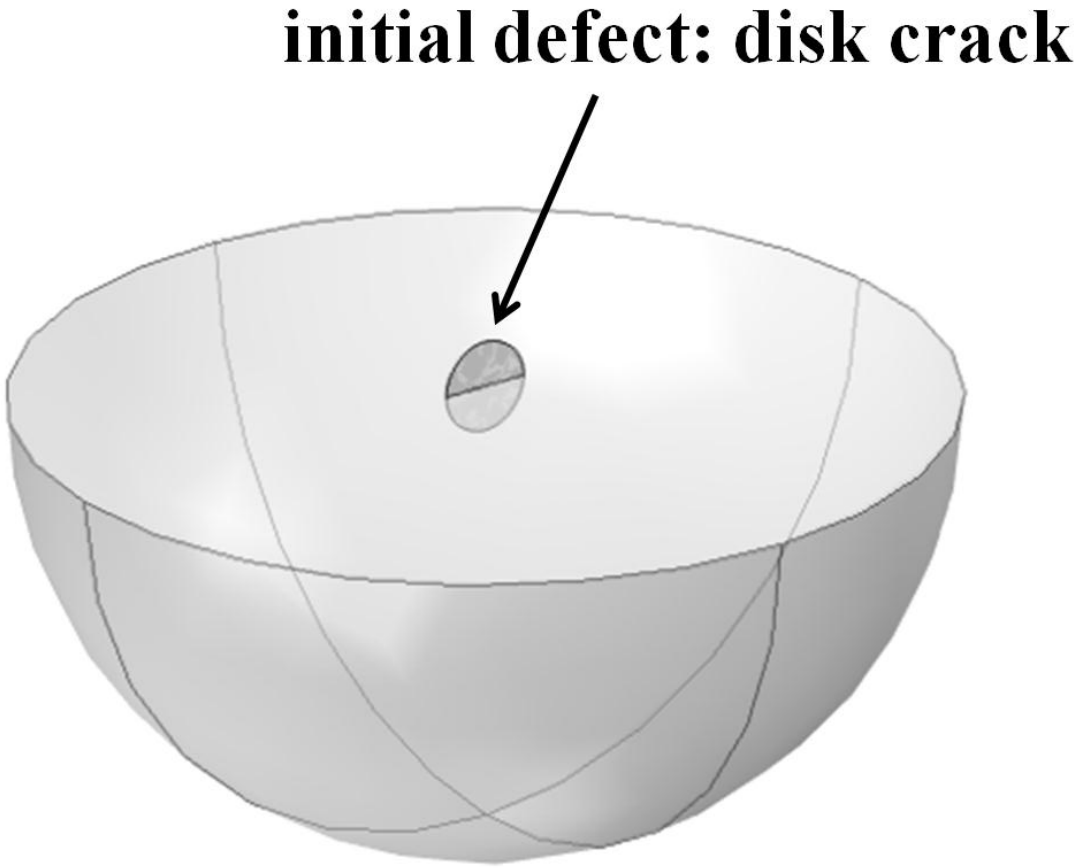

Figure 4.1: Position of initial defect in a Mn_2O_4 particle

Factors	Levels							
particle radius	1μm	3μm	4μm	5μm	6μm	7μm	8μm	9μm
current density	0.1A/m^2 -0.6A/m^2, with an increment of 0.1 A/m^2 (for each particle radius)							

Factors	Levels				
aspect ratio	1:1	1.5:1	2:1	3:1	4:1
C-rate	0. 07C – 0.42C, with an increment of 0.07C (for each aspect ratio)				

Table 4.1: Simulation parameters

ratios ranging from 1 to 4 were simulated. The shape of the particles was prolate ellipsoid with two semi-minor axes of equal length and a longer semi-major axis. The aspect ratio α was defined as the ratio of the semi-major axis and the semi-minor axes. In order to keep the capacity of the active material constant, the total volume of the particles was fixed at $4\pi \times (7\mu m)^3 / 3$. Current density was varied. However, for different aspect ratios, the total surface current (the product of the current density and the surface area) was conserved at each level. The increment of total surface current was fixed at 0.2A/m^2 $\times 4\pi \times (7\mu m)^2$. Therefore, the C-rate at each level was kept constant across particles of varying aspect ratio. The C-rates ranged from 0.07 C to 0.42 C, with an increment of 0.07 C. For each case, the peak $\sigma_{1,\text{MAX}}$ was found for particles without defect via COMSOL and the calculated Li-ion concentration profiled was exported to the ABAQUS fracture simulation. In the ABAQUS model, the initial crack was disk-shaped with a radius 1/10 of that of the semi-minor axis of the ellipsoidal particle; it was located at the center of the particle. The range of the parameters is summarized in Table 4.1.

Initial defect location – Finally, initial defect location is another important factor, since in the actual material defects may exist at any location throughout the volume of a particle. To investigate the effect of initial defect location on fracture propagation, the position of the initial defect in a particle $4\pi \times (7\mu m)^3 / 3$ in volume and with aspect ratio 2 was relocated from the center of the particle to the surface of the particle. Depending on the direction of Li-ion flow, the maximum stress could be located either at the center or along the equator for a prolate spheroidal particle, which implies that both the charging and discharging processes should be examined for initial defect locations over the whole volume of the particle. Thus for each initial defect location, the particle was subjected to

both the charging and the discharging process, and in each case the C-rate was varied from 0.07C to 0.42C, with an increment of 0.07 C. The lowest C-rate at which fracture propagation occurred was reported.

3. Material Properties

As seen in many engineering materials, the orientation of crystalline and grain microstructures are distributed randomly [26, 27] so that macroscopic elastic properties are almost equal in all directions. Thus isotropic behavior was assumed, which was reasonable for the purpose of the present work.

The Young's modulus value for the exact material (Mn_2O_4) in the electrode from direct measurement was not readily available. Values reported in the literature on porous sintered polycrystalline samples and other spinel oxides ranged from 10GPa to 300GPa [28, 29, 30]. In this work, an estimated value of 100GPa was used as Young's modulus. Because maximum tensile strength for the exact material (Mn_2O_4) was not reported in the literature, this study estimated the maximum tensile strength based on the properties of similar brittle materials. For example, TiO_2, which is also an oxide and has a density similar to $Li_xMn_2O_4$ (4.24g/cm^3 compared to 4.4-4.5 g/cm^3), had a tensile strength of 69-103MPa [20, 31]. The maximum tensile strength was estimated to be 100MPa for Mn_2O_4 in the simulation. The surface energy was estimated from a similar cathode material to be 0.66J/m^2 [21]. The material properties are summarized in Table 4.2.

RESULTS

Stress evolution – for the spherical particle with radius 7 μm under study, $\sigma_{1,MAX}$ was found at the surface of the sphere during charge and at the center of the sphere

Property	Unit	Mn_2O_4
Young's modulus (E)	GPa	100 [28, 29, 30]
Poisson's ratio (v)		0.3 [23]
Diffusion coefficient (D)	m^2/s	7.08×10^{-15} [15]
Stoichiometric maximum concentration (c_{max})	mol/m^3	2.29×10^4 [32]
maximum tensile strength (σ_{TS})	MPa	100 [20, 31]
surface energy (γ)	J/m^2	0.66 [21]

Table 4.2: Material properties of Mn_2O_4

during discharge. Figure 4.2 shows that in the spherical particle $\sigma_{1,MAX}$ increased monotonously during the charging process; it should be noted, however, that it first increased to its peak and subsequently decreased during the discharging process. The increase in the stress level during charging could be explained by the fact that the outer part of the particle experienced pressure due to a relatively higher rate of contraction compared to the inside of the particle when Li-ions de-intercalated through the surface. The decrease in the stress level after 960 seconds of discharging could be explained by the fact that as more Li-ions intercalated into the particle while the Li-ion concentration at the particle center rose, the concentration gradient decreased during the later stage of the discharge. It was further noted that the peak $\sigma_{1,MAX}$ values were similar during both the charging and discharging processes. In real battery applications, the discharge rate is often higher than the charge rate; thus, the current study focuses mainly on the discharging process.

Particle size and current density – Figure 4.3(a) shows the concentration profile for a spherical particle with radius 7μm and surface current density 0.5A/m^2 after a discharge time of 960 seconds. The concentration varied from low in the center of the particle to high on the particle surface, indicating higher expansion of the outer part of the particle. As a result, the difference in expansion rate subjected the material of the spherical particle to tensile stress in the direction normal to the sphere surface, creating a condition for mode I fracture to occur. Figure 4.3(b) shows the maximum principle stress level inside the particle, resulting from the difference in expansion rate caused by the Li-ion concentration gradient discussed above. The maximum principal stress was lower near the surface and higher near the center of the particle. The same phenomenon

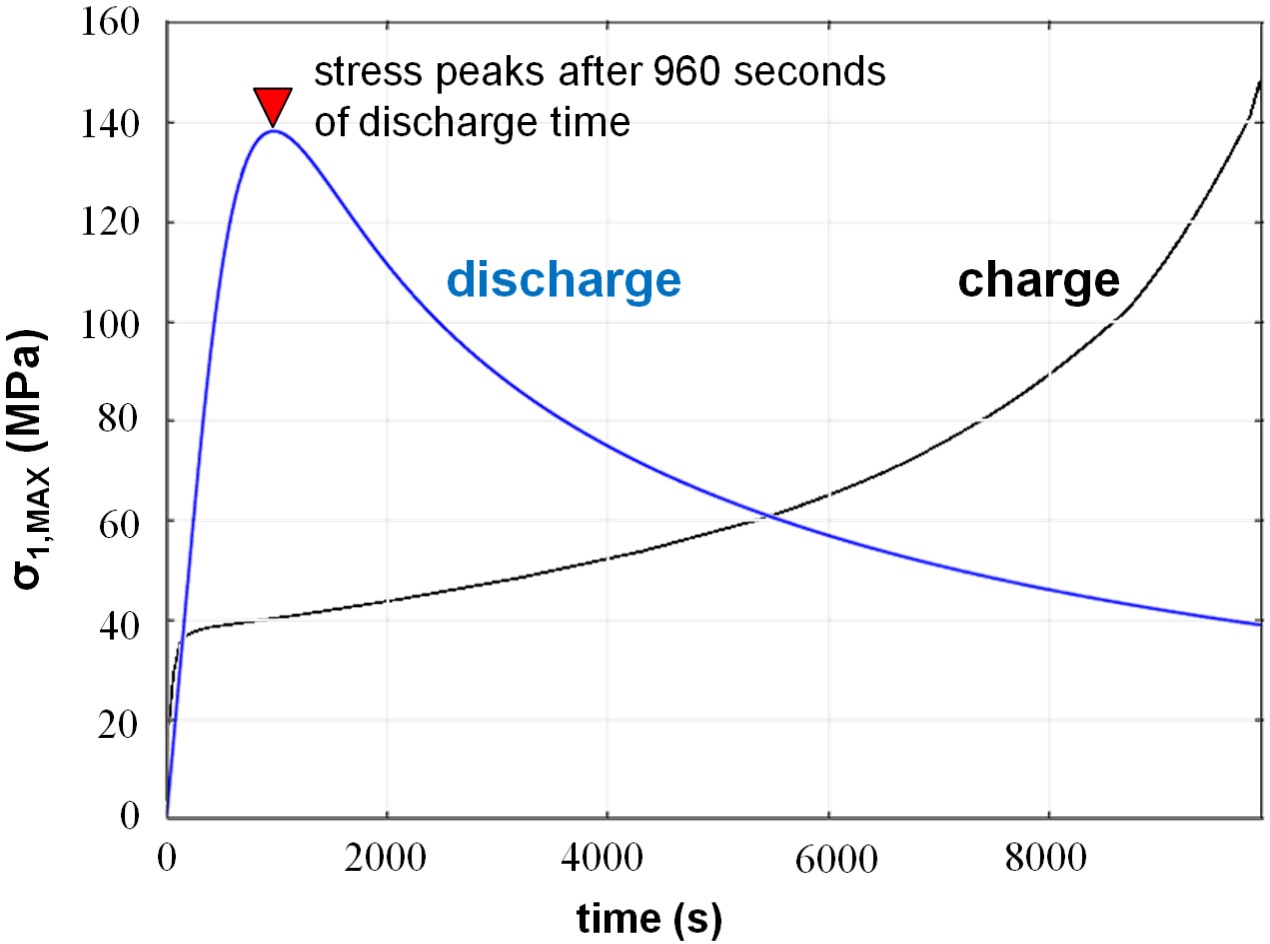

Figure 4.2: Evolution of $\sigma_{1,max}$ during the charging and discharging process for a spherical particle with a radius of 7µm

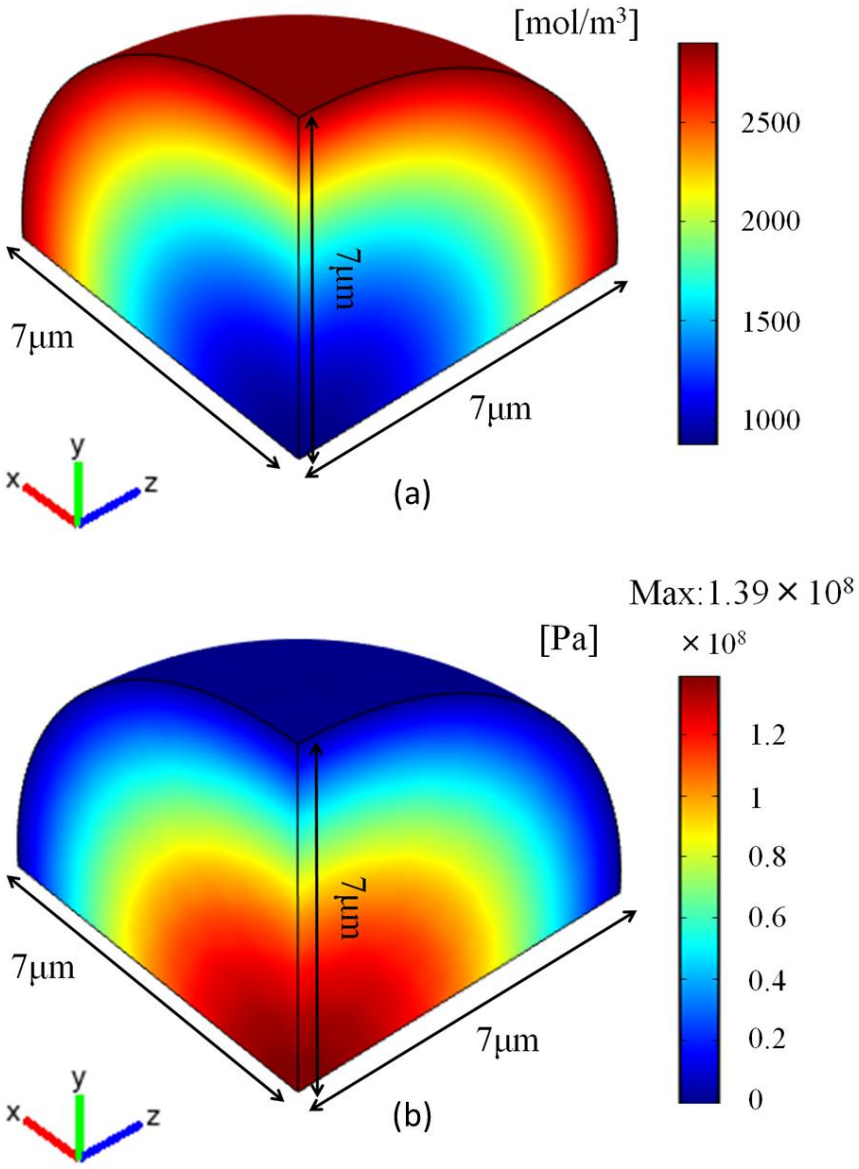

Figure 4.3: Lithium concentration profile and maximum principal stress in a spherical particle during the discharging process (radius = 7μm, current density = 0.5A/m^2, discharge time = 960 seconds when $\sigma_{1,MAx}$ peaks) (a) lithium concentration [mol/m^3] (b) max. principal stress [Pa]

was observed for all the investigated particles with different sizes and aspect ratios. For fracture in brittle material such as Mn_2O_4, the maximum principal stress criterion gave reasonably accurate predictions. Thus, during discharge, crack propagation was more likely to occur with the initial defect near the center of the particle (which was confirmed by changing the initial defect location in a later section); one would miss important phenomena in the fracture study if the inside of the particle were not investigated. The peak $\sigma_{1,MAX}$ for each simulation case for spherical particles is plotted in Figure 4.4. The simulation revealed whether initial defects in the center of the particles propagated further; the results for particle sized from 3μm to 9μm are mapped out in Figure 4.5, and a critical boundary is plotted. The small blue circles represent all the simulation cases that have been performed; the green boundary separates the cases where crack propagation occurs from the cases where crack propagation does not occur; the simulation cases that are located closest to the boundary are marked with large blue dots (no crack propagation) and red diamonds (crack propagates). Additional simulations were performed with more refined current density increments (0.025 A/m^2) to provide a more accurate boundary. Figure 4.6 is a plot of particle size (ranging from 1μm to 9μm) against C-rate (calculated from current density) in log-scale. The critical simulation cases are depicted as green marks. A straight trendline, serving as the critical boundary in log-scale, can be used to fit these data points; this indicates a power-law correlation between particle size and C-rate along the critical boundary (with a coefficient of determination above 0.99).

Particle aspect ratio – Figure 4.7(a) is a representation of the lithium concentration profile for an ellipsoidal particle when the stress level rises to its maximum during discharge. The highest level of lithium concentration can be found at the tip of the

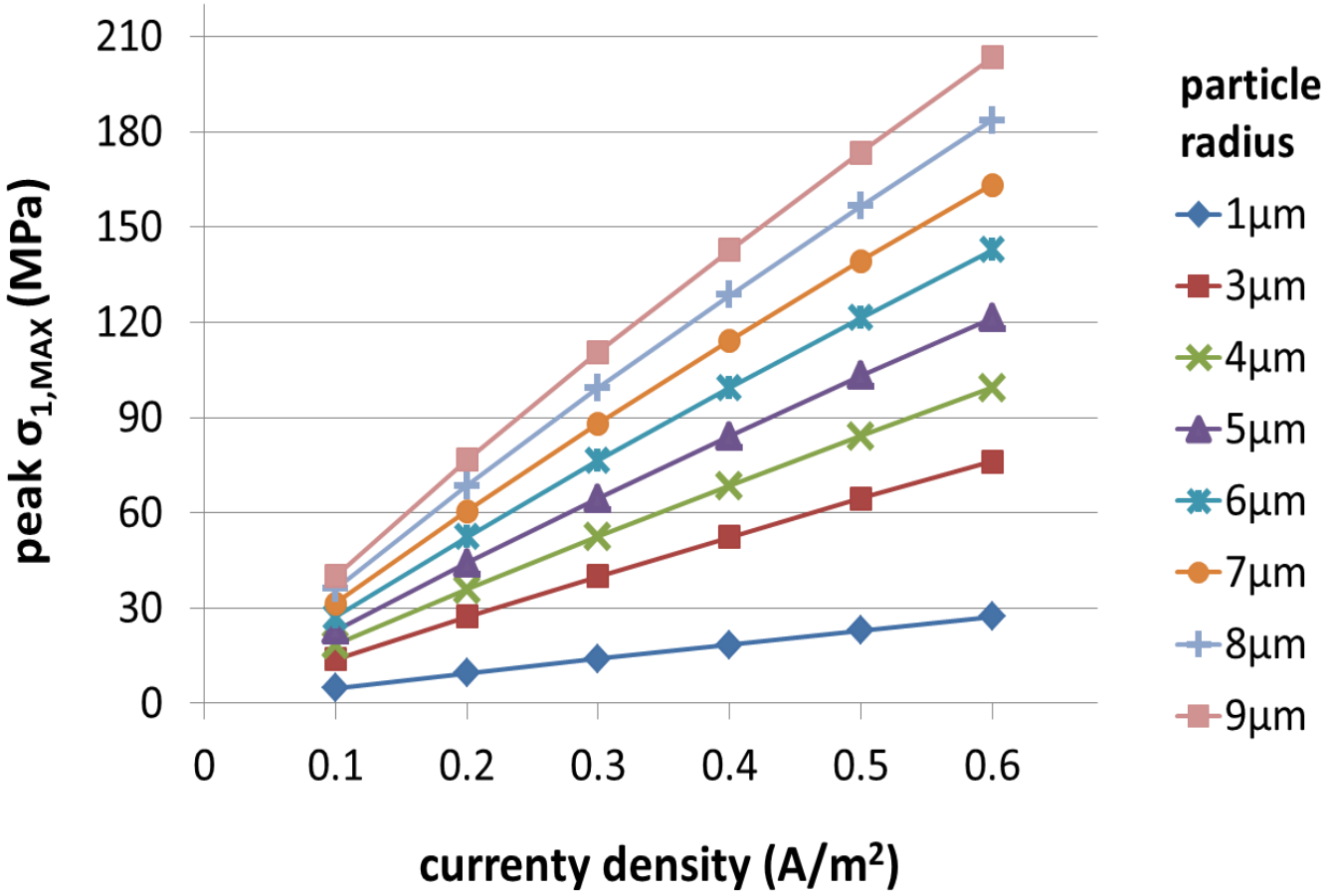

Figure 4.4: Peak $\sigma_{1,max}$ values for spherical particles

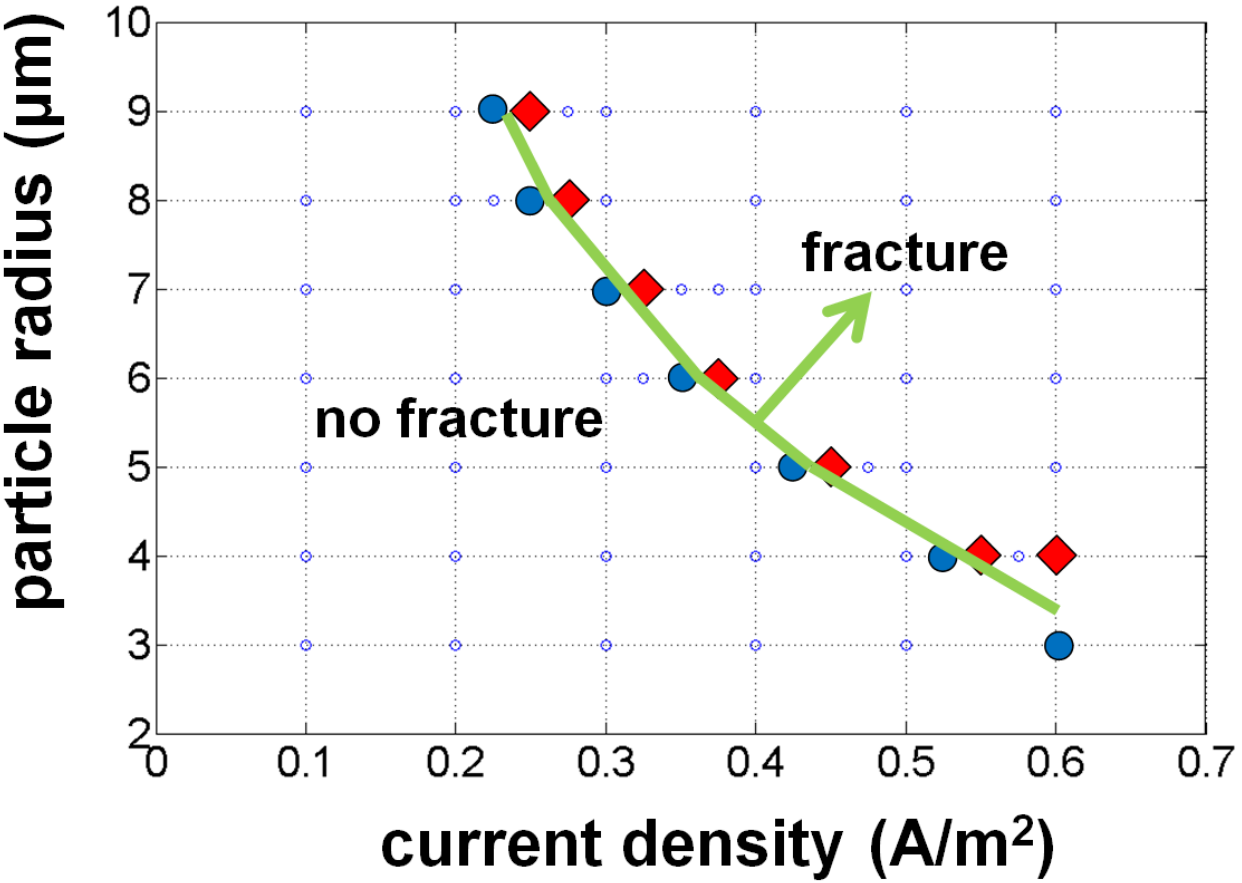

Figure 4.5: Fracture propagation conditions (particle size and current density)

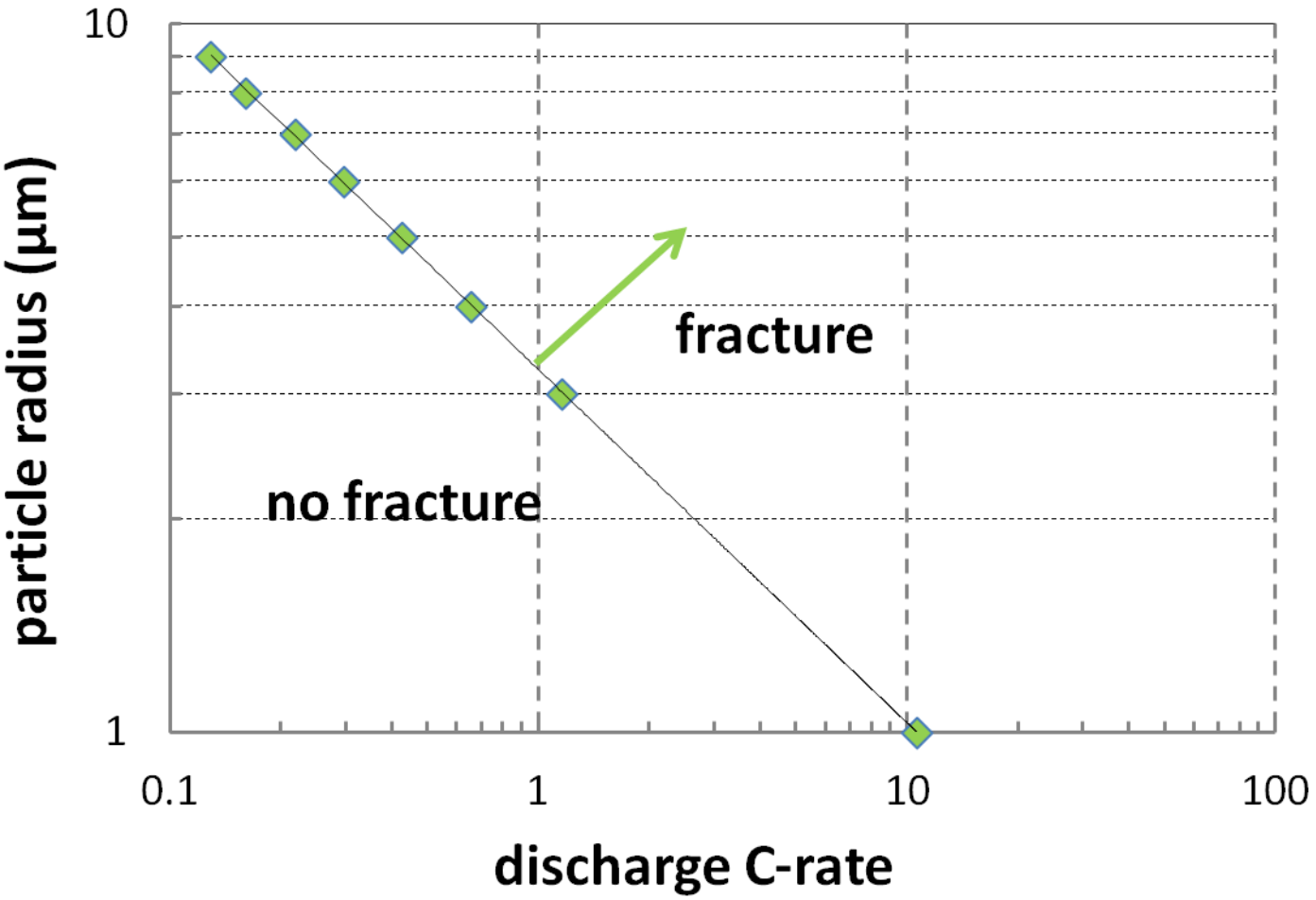

Figure 4.6: Fracture propagation conditions (particle size against C-rate in log scale, 1µm case included)

longer axes; however, the highest level of maximum principal stress is in the center of the particle, as shown in Figure 4.7(b). Under maximum principal stress fracture criterion, crack propagation was most likely to occur near the center of ellipsoidal particles. The $\sigma_{1,\mathrm{MAX}}$ found in particles with different aspect ratios during discharge is plotted in Figure 4.8. With increasing aspect ratio, the $\sigma_{1,\mathrm{MAX}}$ in ellipsoidal particles first increased and then decreased at each C-rate. The highest value of $\sigma_{1,\mathrm{MAX}}$ for the same C-rate can be found for particles with an aspect ratio of 1.5. The combination of particle aspect ratio and current level under which crack propagation occured for defects in the center of the particles was shown in Figure 4.9. The critical boundary for crack propagation to occur was plotted in the same manner as in Figure 4.6, which was described previously. From this boundary, particles with aspect ratio 1.5 were found to require the lowest discharge C-rate (about 0.18C) for crack propagation to occur at the particle center. The non-monotonic dependency of fracturing on aspect ratio is due to the competing effects of the increase and decrease in the length of the three semi-axes. As the aspect ratio increases while volume is conserved, the Li-ion diffusion path is increased along the semi-major axis, increasing the concentration gradient, which in turn increases stress. However, the diffusion path decreases along the two semi-minor axes, lowing the concentration gradient and stress.

Initial defect location - Particles $4\pi \times (7\mu m)^3 / 3$ in volume and with aspect ratio 2 were used to determine the most favorable initial defect location for crack propagation. During the discharging process, when the initial crack was located at the center of the particle, crack propagation occurred at a current rate of 0.21C. The initial defect was moved along the semi-major axis and the C-rates at which fracture occurs were shown in

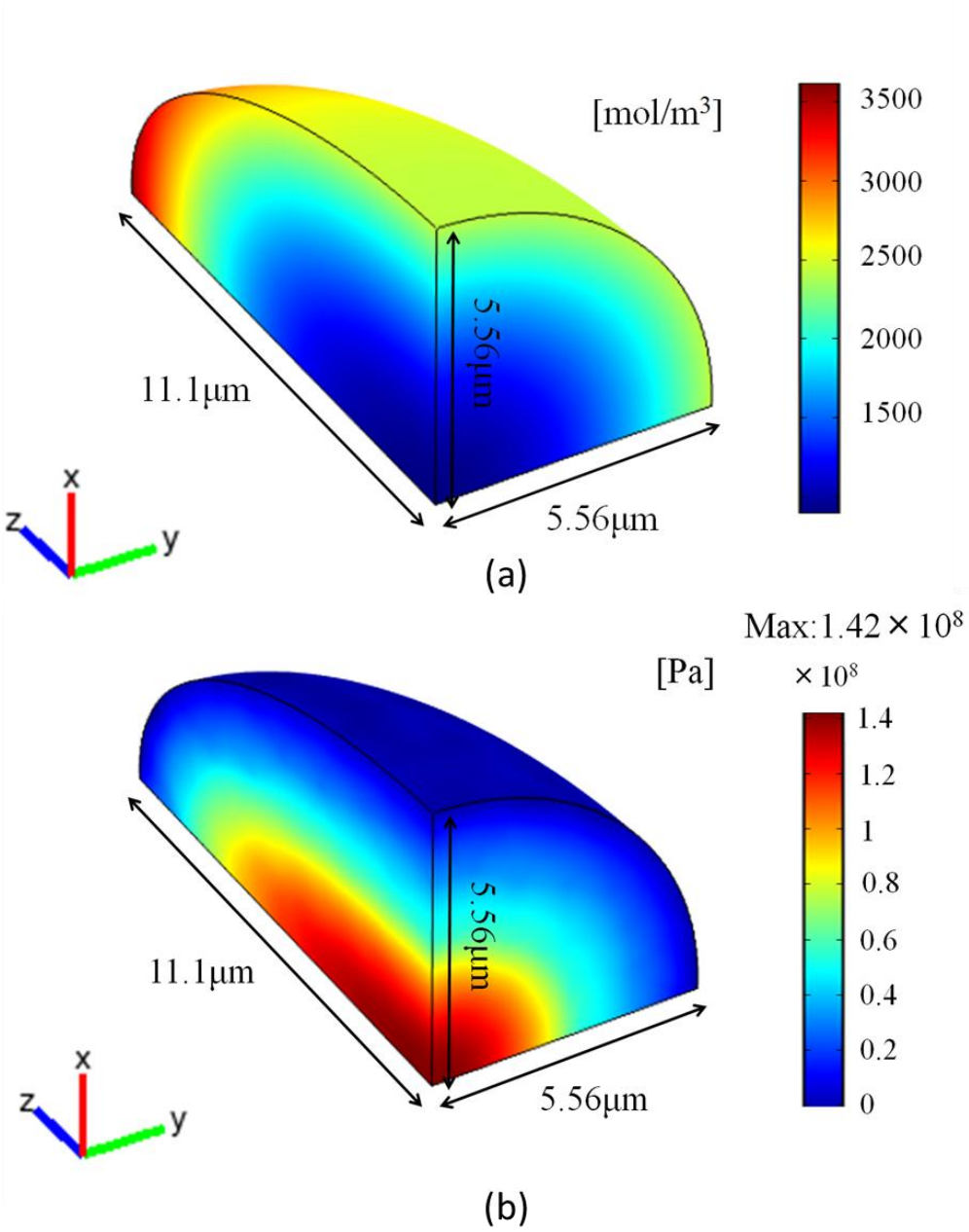

Figure 4.7: Lithium concentration profile and maximum principal stress in an ellipsoidal particle during the discharging process (aspect ratio = 2, charging rate = 0.35C, discharge time = 900 seconds when $\sigma_{1,MAX}$ peaks) (a) lithium concentration [mol/m^3] (b) max. principal stress [Pa]

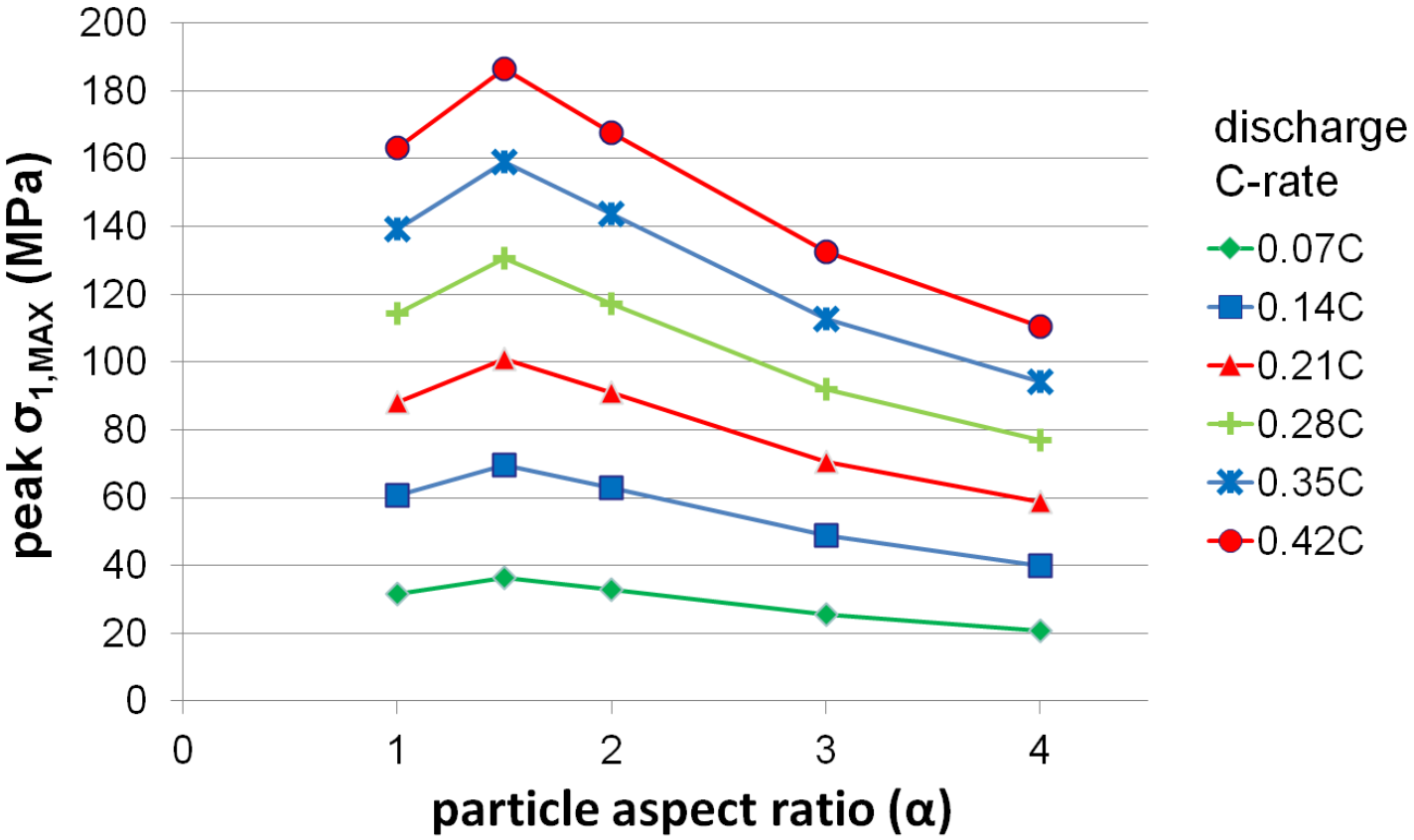

Figure 4.8: Peak $\sigma_{1,max}$ values with particle aspect ratio α. The particle volume was the same for all cases; and radius=7μm when α = 1

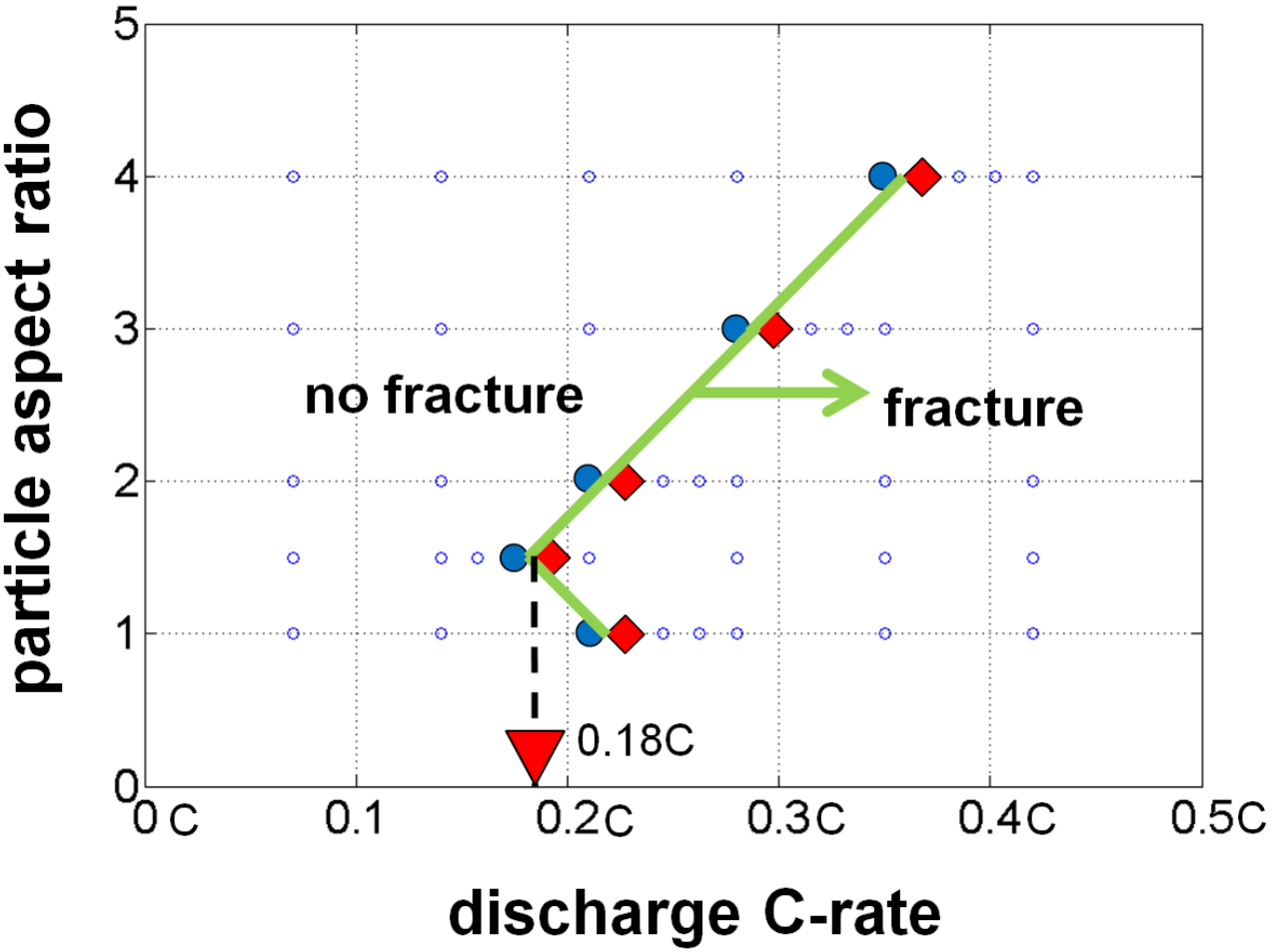

Figure 4.9: Fracture propagation conditions (aspect ratio and current density), with corresponding C-rates shown

Figure 4.10. When the defect was located away from the center by 1/3 or 1/2 of the length of the semi-major axis (position A and B), the crack propagated at a current rate of 0.28C. A crack did not propagate even at 0.42C in the case where the initial defect was located on the surface of the particle (position C). When the initial defect was then moved along the semi-minor axis away from the center by 1/3 the length of the semi-minor axis (position D), crack propagation occurred at 0.35C. When the initial defect was then moved along the semi-minor axis away from the center by 1/2 the length of the semi-minor axis (position E) or was located at the surface (Position F), crack propagation did not occur, even for discharging rates as high as 0.42C. Figure 4.10(a) shows the lowest C-rates at which fracture propagates for different initial defect locations. However, when the same particle was subjected to the charging process, an initial defect located in almost all of the above mentioned locations did not propagate for charging rates up to 0.42C (except for Position F, the initial crack propagates at a charging rate of 0.35C), as shown in Figure 4.10(b). Figure 4.11 shows the lithium concentration level and the maximum principal stress level in the particle during the charging process. The $\sigma_{1,\mathrm{MAX}}$ can be found at the surface of the particle corresponding to Position F. Comparing Figure 4.10 (a) and (b), it was noticed that crack propagation is most likely to occur from an initial defect at the center of the particle during discharge.

DISCUSSION

Only single smooth ellipsoidal particles were considered in this work; this was done to study the effect of parameters such as aspect ratio, particle size and current density, as well as the location of the initial defect. In the prior art, fracture mechanisms

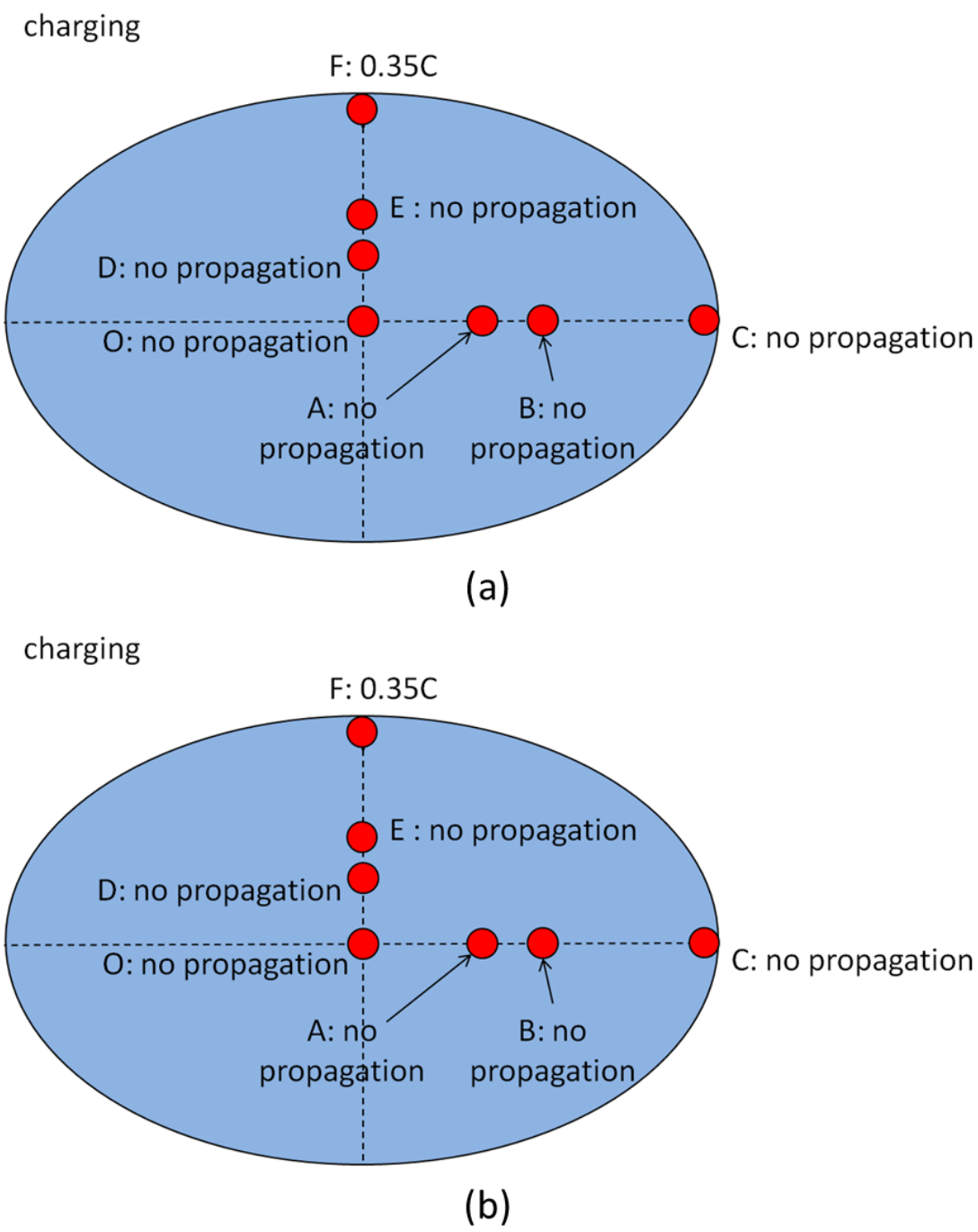

Figure 4.10: lowest C-rates (up to 0.42C) at which fracture propagated for different initial defect location (a) during discharging; (b) during charging

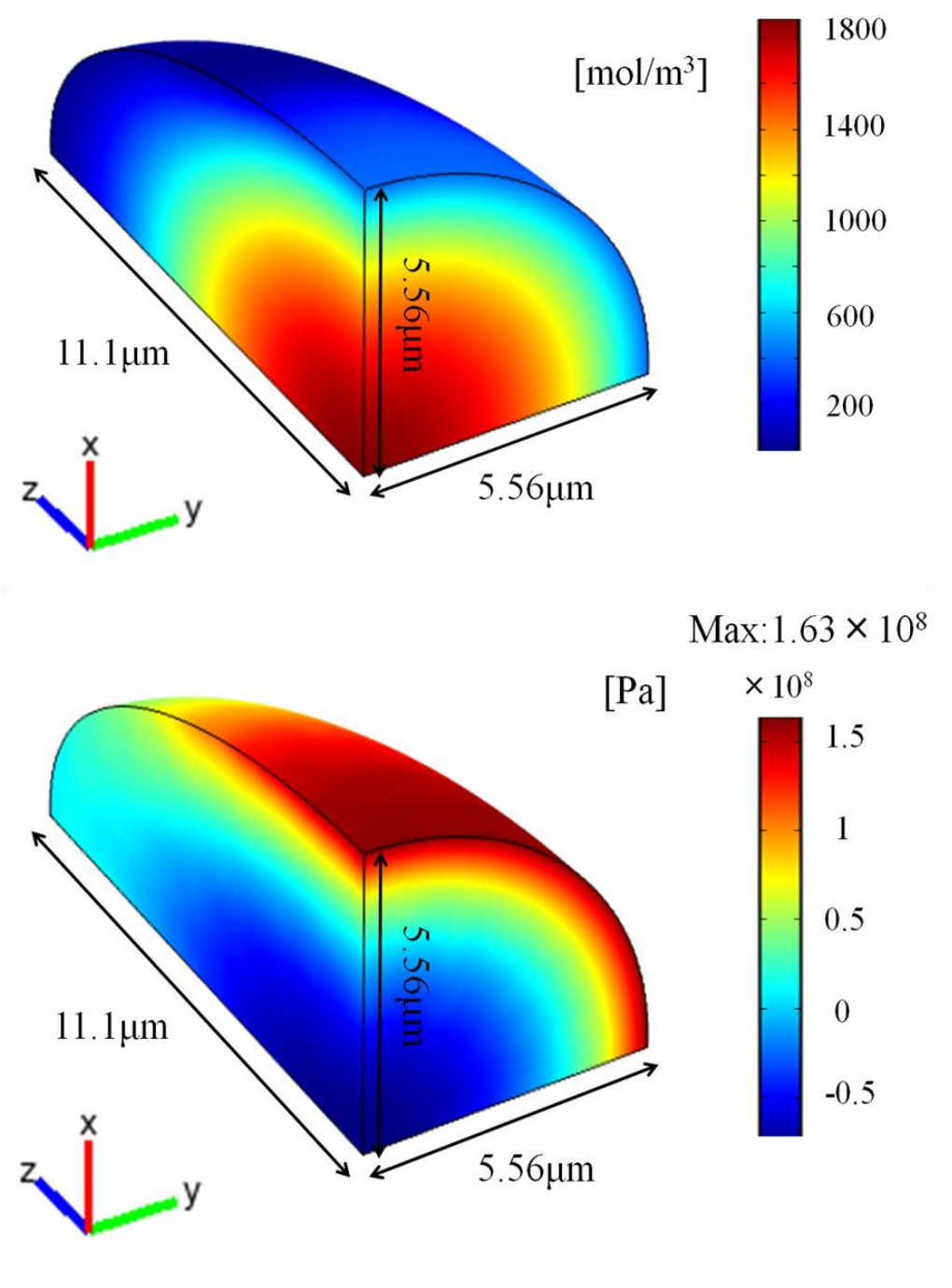

Figure 4.11: Lithium concentration profile and maximum principal stress during the charging process (aspect ratio = 2, charging rate = 0.35C, charge time = 10068 seconds when max. 1st principal stress reached the highest level) (a) lithium concentration [mol/m^3] (b) max. principal stress [Pa]

had been employed in electrode materials. In some cases, however, realistic electrochemical loading conditions and the geometrical effects were not investigated [21]; in others, only perfectly spherical particles with initial defects located on the surface were considered [22]. Our findings—that fracture tends to propagate in particles with larger size and higher current density—are in agreement with the trend reported in these analysis results. However, due to differences in the parameters used, such as Young's Modulus, partial molar volume, and especially diffusivity (the reported diffusivity values from various sources has discrepancies of several orders of magnitude), our results cannot be directly compared to the simulation results in the prior arts. While the prior arts generally consider spherical particles with initial defects located near the surface [22], the efforts were focused on the propagation of initial defects inside the particle during the discharge of cathode materials, thus showing the energetically favorable location of crack propagation during cycling and revealing new possible ways of particle failure.

Our study shows that crack propagation can occur at a low C-rate at the order of C/5. This finding matches well with experimental observations of fracture in cathode active materials [1, 3], where cracking occurs when cycling at a rate of 30mA/g (C/5) for LiFePO4 with a capacity of 149mAh/g, and at a current density of 0.4mA/cm^2 (also C/5) for $LiCoO_2$. Our study also shows that there is a power-law correlation between particle size and the maximum discharge rate that this particle size can withstand. As particle size decreases, the maximum discharge rate increases rapidly. For example, the maximum allowable discharge rate exceeds 10C for spherical particles with a radius less than 1μm. Therefore, when a threshold size is reached, intercalation-induced fracture no longer

needs to be considered in battery optimization for practical usage. This finding is in agreement with experimental observations in other battery electrode materials [33].

Even though the current simulations address some key physical phenomena related to fracture in the cathode particles, there are still issues important to understanding the entire mechanism of fracture in the active materials as well as the effect of fracture on battery performance. These topics include a wide range of physics; they cannot be addressed all together.

In this work only single isolated ellipsoidal particles were considered. The cathode system contains aggregated structures formed by active material particles, inactive polymer binder and conductive additive [34]. The interaction between multiple active material particles as well as interaction between different material phases will affect the stress level and the fracturing behavior of the particles as well as the integrity of the whole aggregated structure. It will be necessary not only to consider fracturing within the homogenous single phase, but also to investigate the disruption of the boundary between the active material and inactive material phases [21].

Further, it was assumed that the cell was charged and discharged in the single phase region, and thus that Jahn-Teller distortion was prevented. Figure 4.4 shows the dependence of maximum principal stress on the particle size and current density within this single phase region: larger particle size and higher current density will increase the level of maximum principal stress, thus increasing the chance for crack propagation to occur. In some real world applications, however, crystallites at the surface of the particle can be over-lithiated at high C-rates and undergo phase transition locally even when the overall voltage of the cell is above 3.0V. This phase transition effect can lead to abrupt

lattice parameter change and increase stress significantly when combined with volume change due to intercalation. This contributing factor to fracture propagation will be considered in a future study.

The present work considered smooth ellipsoidal particles. While these provide a more general representation of real world cathode particles than the purely spherical models, the present work should lead to the future simulation of particles with irregular shape and non-smooth multiple convex and concave surfaces, as well as with particles containing such defects as phase boundaries and/or grain boundaries. In addition, interaction between multiple particles, as well as interaction between active material particles and polymer binders in the aggregates level of a cathode system, should also be considered.

BIBLIOGRAPHY

[1] Wang, D., Wu, X., Wang, Z. and Chen L., 2005, "Cracking causing cyclic instability of $LiFePO_4$ cathode material", *Journal of Power Sources*, **140**, pp. 125–128

[2] Lim, M.-R., Cho, W.-I. and Kim, K.-B., 2001, "Preparation and characterization of gold-codeposited $LiMn_2O_4$ electrodes", *Journal of Power Sources*, **92**, pp. 168-176

[3] Wang, H., Jang, Y.-I., Huang, B., Sadoway, D.R. and Chiang, Y.-M., 1999 "TEM Study of Electrochemical Cycling-Induced Damage and Disorder in $LiCoO_2$ Cathodes for Rechargeable Lithium Batteries", *Journal of The Electrochemical Society*, **146** (2) , pp. 473-480

[4] Thackeray, M. M., Shao-Horn, Y., Kahaian, A. J., Kepler, K. D., Skinner, E., Vaughery, J. T. and Hackney, S. A., 1998, "Structural fatigue in spinel electrodes in high voltage (4V) Li/LixMn2O4 cells", *Electrochem. Solid-State Lett*., **1**(1), pp.7

[5] Ohzuku, T., Kitagawa, M. and Hirai, T., 1989, "Electrochemistry of Manganese Dioxide in Lithium Nonaqueous Cell", *J. Electrochem. Soc*., **136**(11), pp. 3169-3174

[6] Ohzuku, T., Tomura, H. and Sawai, K., 1997, "Monitoring of particle fracture by acoustic emission during charge and discharge of Li/MnO2 cells", *J. Electrochem. Soc*., **144**, pp.3496

[7] Striebel, K.A., Sierra, A., Shim, J., Wang, C.-W. and Sastry, A.M., 2004, "The effect of compression on natural graphite anode performance and matrix conductivity", Journal of Power Sources, **134**, pp.241-251.

[8] Wang, C.-W., Yi, Y.-B., Sastry, A.M., Shim, J. and Striebel, K.A., 2004, "Particle Compression and Conductivity in Li-ion Anodes with Graphite Additives", Journal of the Electrochemical Society, **151** (9), pp. 1489-1498

[9] Yi, Y.-B., Wang, C.-W. and Sastry, A.M., 2006, "Compression of Packed Particulate Systems: Simulations and Experiments in Graphitic Li-ion Anodes", ASME Journal of Engineering Materials and Technology, **128**(1), pp. 73-80.

[10] David, W. I. F., Thackeray, M. M., de Piccitotto, L. A. and Goodenough, J. B., 1987, "Structure refinement of the spinel-related phases Li2Mn2O4 and Li0.2Mn2O4", *J. Solid State Chem.,* **67**, pp.316

[11] Scarminio, J., Talledo, A., Andersson, A. A., Passerini, S. and Decker, F., 1993, "Stress And Electrochromism Induced by Li Insertion In Crystalline And Amorphous V_2O_5 Thin Film Electrodes", *Elecrrochimica Acta*, **38** (12), pp. 1637-1642.

[12] Ohzuku, T., Kitagawa, M. and Hirai, T., 1990, "Electrochemistry of Manganese Dioxide in Lithium Nonaqueous Cell", *J. Electrochem. Soc*., **137**, pp.769

[13] Zaghib, K., Shim, J., Guerfi, A., Charest, P. and Striebel, K. A., 2005, "Effect of carbon source as additives in LiFePO4 as positive electrode for lithium-ion batteries", *Electrochem. Solid-State Lett*., **8**, pp. A207

[14] Christensen, J. and Newman, J., 2006 "Stress generation and fracture in lithium insertion materials", *J. Solid State Electrochem.*, **10**, pp.293

[15] Zhang, X., Shyy, W. and Sastry, A. M., 2007, "Numerical Simulation of Intercalation-Induced Stress in Li-Ion Battery Electrode Particles", *Journal of The Electrochemical Society*, **154**(10), pp. A910

[16] Zhang, X., Sastry, A.M. and Shyy, W., 2008, "Intercalation-induced stress and heat generation within single lithium-ion battery cathode", Journal of the Electrochemical Society, v.**155**(7), pp.A542

[17]. Cheng, Y.-T. and Verbrugge, M. W., 2008, "The influence of surface mechanics on diffusion induced stresses within spherical nanoparticles", *J. Appl. Phys.*, **104**, pp.083521

[18] Cheng, Y.-T. and Verbrugge, M. W., 2009, "Evolution of stress within a spherical insertion electrode particle under potentiostatic and galvanostatic operation", *J. Power Sources*, **190**, pp.453

[19]Cheng, Y.-T. and Verbrugge, M. W., 2010, "Diffusion-Induced Stress, Interfacial Charge Transfer, and Criteria for Avoiding Crack Initiation of Electrode Particles", *Journal of The Electrochemical Society*, **157** (4), A508

[20] Christensen, J. and Newman, J., 2006, "A Mathematical Model of Stress Generation and Fracture in Lithium Manganese Oxide", *Journal of The Electrochemical Society*, **153** (6), pp. A1019

[21] Hu, Y., Zhao, X. and Suo, Z., 2010, "Averting cracks caused by insertion reaction in lithium–ion batteries", *J. Mater. Res*., **25**(6), pp. 1007

[22] Woodford, W. H., Chiang, Y.-M. and Carter, C., 2010, "'Electrochemical Shock' of Intercalation Electrodes: A Fracture Mechanics Analysis", *Journal of The Electrochemical Society,* **157** (10), pp. A1052

[23] Prussin, S., 1961, "Generation and Distribution of Dislocations by Solute Diffusion" *J. Appl. Phys.*, **32**, pp. 1876

[24] ABAQUS/Standard: Version 6.9. Hibbitt, Karlsson & Serensen, Inc. (2009)

[25] Park, J., Lu, W. and. Sastry, A. M., 2011, "Numerical Simulation of Stress Evolution in Lithium Manganese Dioxide Particles due to Coupled Phase Transition and Intercalation", *Journal of The Electrochemical Society,* **158** (2), pp. A201

[26] He, X., J Cai, . Li, Y., Jiang, C. and Wan, C., 2006, "Preparation of spherical spinel LiMn2O4 cathode material for Li-ion batteries", *Materials Chemistry and Physics* **95**, pp.105

[27] Choa, T.H., Parka, S.M., Yoshioa, M., Hiraib, T. and Hideshimab, Y., 2005, "Effect of synthesis condition on the structural and electrochemical properties of Li[Ni1/3Mn1/3Co1/3]O2 prepared by carbonate co-precipitation method", *Journal of Power Sources* **142**, pp. 306

[28] Paolone, A., Cantelli, R., Rousse, G. and Masquelier, C., 2003 " The charge order transition and elastic/anelastic properties of $LiMn_2O_4$", *J. Phys.: Condens. Matter*, **15**, pp.457

[29] Yoneda, A., 1990, "Pressure derivatives of elastic-constants of single-crystal MgO and $MgAl_2O_4$", *J. Phys. Earth*, **38**, pp.19

[30] Ravinder, D., 1994, " Composition dependence of the elastic moduli of mixed lithium–cadmium ferrites", J. Appl. Phys., **75**, pp.6121

[31] Cardarelli, F., 2000, *Materials Handbook: A Concise Desktop Reference*, Springer-Verlag, London

[32] Yamada, A. and Tanaka, M., 1995, "Jahn-Teller structural phase transition around 280K in $LiMn_2O_4$", *Mater. Res. Bull.*, **30**, pp.715

[33] Ryu, I., Choi, J. W., Cui, Y. and Nix, W. D., 2011, "Size-dependent fracture of Si nanowire battery anodes ", *Journal of the Mechanics and Physics of Solids*, **59**, pp. 1717–1730

[34] Zhu, M., Park, J. and Sastry, A. M., 2011, "Simulation of Particle Interactions in Cathode Material of Li-Ion Batteries", *Journal of The Electrochemical Society,* 158 (10) pp. A1155-A1159

CHAPTER V

FRACTURE ANALYSIS OF CATHODE PARTICLE AGGREGATES

INTRODUCTION

Fracture in Li-ion batteries has been experimentally observed and implicated as a capacity fade mechanism causing loss of electrical contact in the secondary particles [1, 2, 3]. Fracture in the cathode system can not only occur within secondary active material particles, but also between these particles and across the whole electrode [4]. Inter-particle fracture may occur due to the debonding between active material particles and polymer binder, as well as the cracking of the mixture of conductive additive and polymer binder [5]. Figure 5.1 provides an illustration of the above-mentioned failure modes. Fracture not only impacts the mechanical integrity of the electrodes, but also causes loss of electrical contact and increases the surface area exposed to the electrolyte, causing increased side-reactions, Mn^{2+} dissolution and capacity fade [1, 5, 6, 7].

One possible cause of fracture in battery materials is high stress, which may result from the cycling of the cells throughout the lifetime of the Li-ion batteries. The intercalation and deintercalation of lithium ions causes the expansion and contraction of the cubic lattice structure in $Li_xMn_2O_4$ ($0<x<1$) [8, 9]; during phase transition (when $1<x<2$) an even larger volume change and stress level increase occurs, resulting from a 5.6% expansion caused by Jahn-Teller distortion [10, 11]. The stress caused by both the

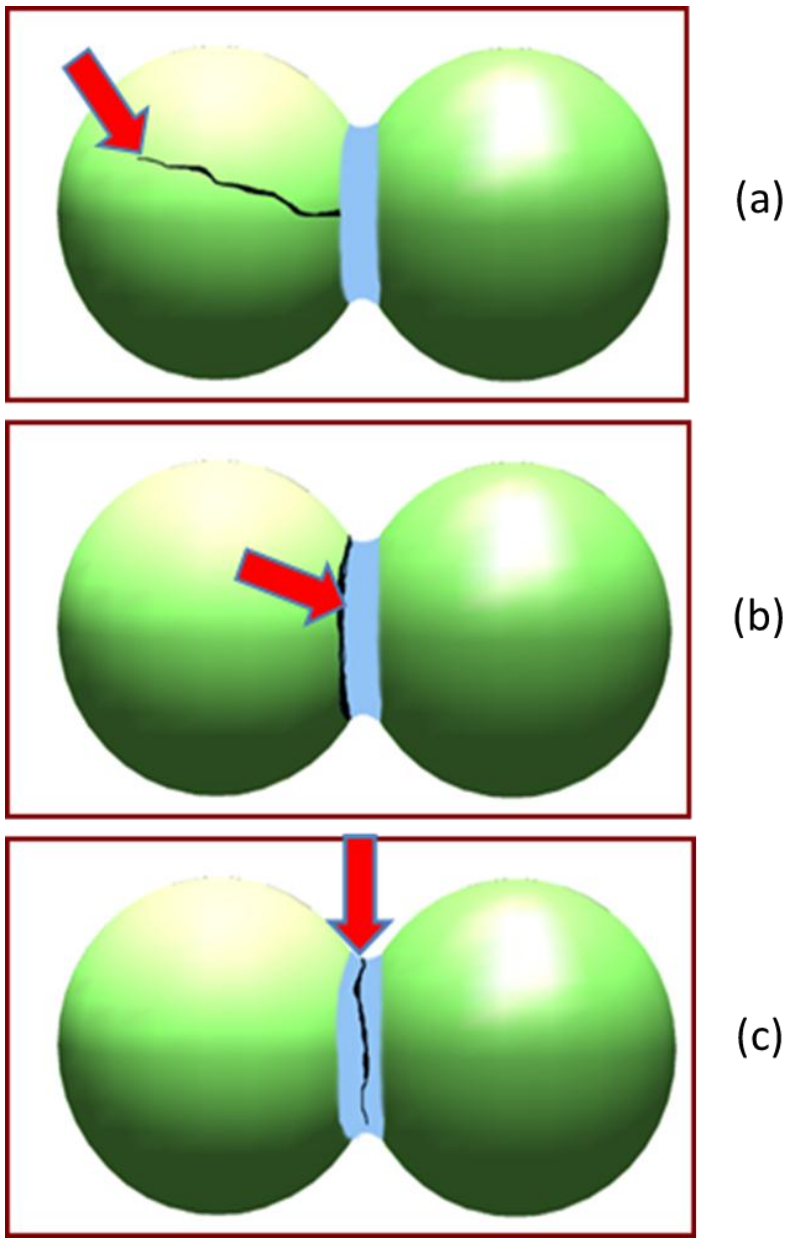

Figure 5.1: The spheres represent active material particles, with polymer binders in between. Fracture in the cathode system (denoted by red arrow) can occur (a) inside a single particle, (b) as debonding between the particle and binder, and (c) in the binder.

first order transition and Jahn-Teller distortion can contribute to local fracture in the active material of a battery cathode.

Several analytical and numerical models have been proposed to predict stress level and fracturing in a single Li-ion battery cathode active material particle [12, 13, 14, 15, 16, 17,18, 19, 20, 21, 22]. Aggregated cathode structures have been constructed using physics-based algorithms—Browning dynamics simulation, for instance, which provides insight into the structural integrity and conductive path for the cathode system—that consider realistic forces during cathode fabrication [5]. In the previous chapter, we presented stress analysis for single spherical active material particles with various aspect ratios. However, fracture analysis has not been conducted for cathode aggregates in the prior arts. Thus, in this work our objectives are as follows:

1) find the stress level within a regular lattice system consisting of active material particles and polymer binders;
2) find the effects of a few geometric parameters on the stress level of the aggregate;
3) find the stress level within an aggregated structure obtained from physics-based aggregation simulation

METHODS

In a cathode-aggregated structure consisting of both brittle active material and ductile polymer binder, tensile stress level is one of the indicators of failure. Thus, three principal stresses, σ_1, σ_2, and σ_3, were calculated using COMSOL Multiphysics simulation for particle aggregates without initial defects during cycling. Their evolution

during lithium intercalation and deintercalation was also captured. The three principal stresses were ranked in descending order, and the largest of the three—maximum principal stress—was denoted σ_1. In each case, the highest point of σ_1 was identified in the particle, and the maximum principal stress at that location was denoted $\sigma_{1,MAX}$. $\sigma_{1,MAX}$ rose to its peak before the charge/discharge process reached its end due to the reduction of the Li-ion concentration gradient in the later stage.

Section 1 provides the governing equations and methodologies used in the 3D finite element analysis in this study; Section 2 explains the simulation setups and the range of parameters under study; and Section 3 describes the material properties used in the simulation.

1. Three-dimensional Finite Element Simulation

In the aggregates consisting of active material (Mn_2O_4) and polymer binder (PVDF), the PVDF binders were treated as electrochemically inert and impenetrable by Li-ions during the reaction. As for the active materials, it was assumed that only a single cubic phase of $Li_xMn_2O_4$ existed in the particle, where $0<x<1$. The volume change in a single phase particle was solely attributable to the insertion and extraction of lithium to and from the interstitial sites in the Mn_2O_4 framework. In the simulations conducted, it was assumed that the onset of Jahn-Teller distortion in the spinel structure was prevented by charging and discharging the cell between x=0 and x=1 only. The lithium intercalation-induced stress during cycling was calculated using an analogy to thermal stress [14, 15, 23], assuming that the lattice constants of the material changed linearly with the amount of ions inserted [8].

To obtain the concentration profile due to intercalation, the diffusion problem was solved together with the elastic field. The driving force for Li-ion diffusion can be obtained by the gradient of the characteristic potential comprising the chemical and elastic energy of the system. The diffusion flux **J** is given by [14]

$$\mathbf{J} = -D\left(\nabla c - \frac{\Omega c}{RT}\nabla \sigma_h\right) \tag{1}$$

where c is the concentration of the Li-ions, D is the diffusion coefficient, Ω is the partial molar volume of Li-ion, R is a gas constant, T is absolute temperature, and σ_h is the hydrostatic stress.

Combining Eq. 1 with the mass conservation equation, $\partial c/\partial t + \nabla \cdot \mathbf{J} = 0$, we have

$$\frac{\partial c}{\partial t} = D\left(\nabla^2 c - \frac{\Omega}{RT}\nabla c \cdot \nabla \sigma_h - \frac{\Omega c}{RT}\nabla^2 \sigma_h\right) \tag{2}$$

The initial condition is $c=c_o$, and the constant current boundary condition

$$\mathbf{J} = -D\left(\nabla c - \frac{\Omega c}{RT}\nabla \sigma_h\right) = \frac{\mathbf{i_n}}{F} \tag{3}$$

where $\mathbf{i}_n$ is the current density on the particle surface and F is Faraday's constant.

The stress-strain relation with the existing concentration gradients can be written as

$$\varepsilon_{ij} = \frac{1}{E}\left[(1+\nu)\sigma_{ij} - \nu\sigma_{kk}\delta_{ij}\right] + \frac{\tilde{c}\Omega}{3}\delta_{ij} \tag{4}$$

where $\tilde{c} = c - c_0$ is the lithium concentration change from the original stress-free value, ε_{ij} and σ_{ij} are strain and stress components, E is Young's modulus, ν is Poisson's ratio, c is the Li-ion concentration, and δ_{ij} is the Kronecker delta. The last term accounts for the intercalation strain.

The problem was solved in three-dimensional space using FEMLAB (COMSOL Multiphysics). Two models were included in the multiphysics simulation: the PDE (partial differential equation) model and the solid stress–strain model. In the PDE model, the diffusion process was described by the generalized form of Eq. 2. In the solid stress-strain model, "thermal expansion" was included as a load based on the variable of the concentration *c* instead of temperature in the thermal stress calculation.

2. Simulation setup

In this study, two types of aggregated systems are investigated. The first is a uniform infinite lattice formed by active material and polymer binder, as shown in Figure 5.2. The active material particles are modeled as complete spheres, and the PVDF binders are modeled as spheres connecting two adjacent active material particles. The portions of the PVDF binder spheres which overlap with the active material are cut away, forming craters in the binder sphere that fit perfectly with the active material particle surface. A small part of the system is simulated with symmetry boundary conditions applied on all flat surfaces. The second type of aggregated system is generated from the Brownian dynamics simulation presented in Chapter II; carbon black is omitted, as shown in Figure 5.3. The aggregate consists of 10 active material particles, which are modeled as spheres. Similar to the previous system, the portions of the PVDF binder cylinders which overlap with the active material are cut away, forming craters in the binder cylinder that fit perfectly with the active material particle surface.

In both of these two types of aggregation systems, Li-ion intercalation-induced expansion is simulated in the active material phase; PVDF is assumed to be chemically

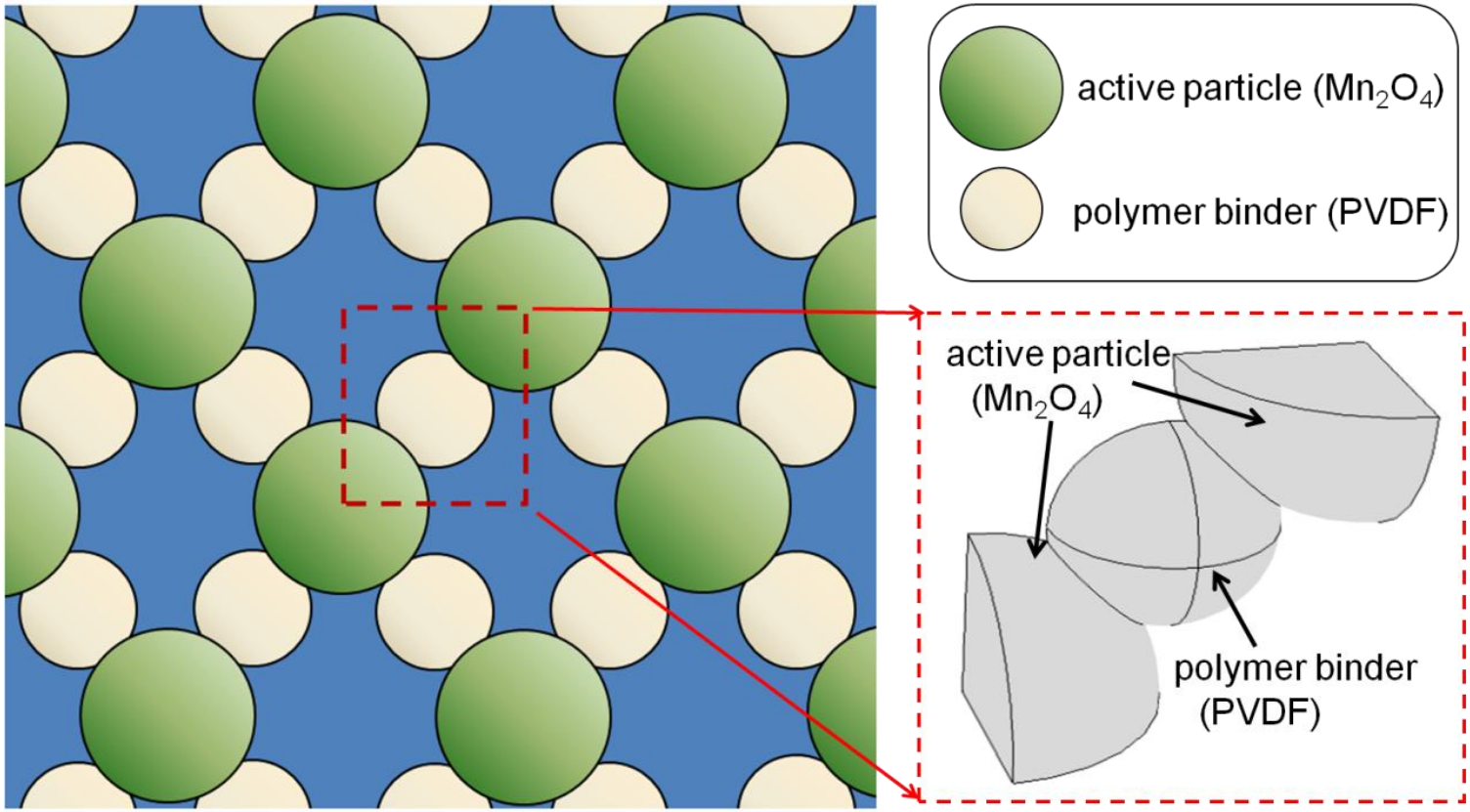

Figure 5.2: Illustration of the uniform lattice (1st type of aggregated system) modeled. A small part of the system is simulation in COMSOL, with symmetry boundary conditions applied to all flat surfaces

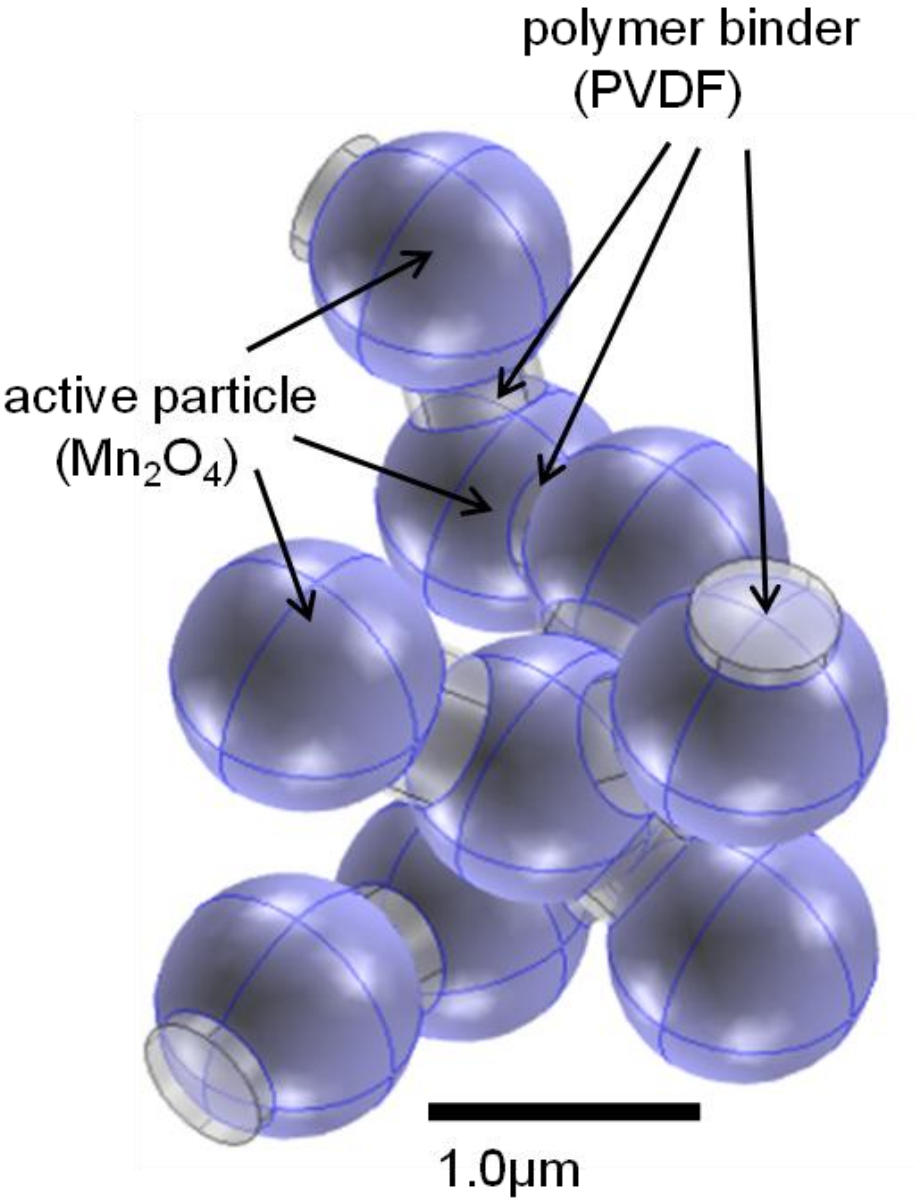

Figure 5.3: Illustration of the aggregated structure from Brownian dynamics simulation (2nd type of aggregated system) modeled

inert and impermeable to Li-ion; perfect attachment is assumed at the interface between PVDF binder and active material; and no Li-ion flux occurs at the interface.

In the 1st type of aggregation system, we studied the effect of 1) the particle-binder contact area and 2) the relative position between active particles. In these studies, the radii of active material particls are fixed at 5.0μm, and the surface current density is fixed at 1.6A/m^2. To study the first effect, we fixed the distance between two adjacent active material particles at 7.07μm and increased the contact area between active particles and polymer binder by increasing the radius of the polymer. We increased the radius of the polymer from 2.4μm to 3.6μm, with an increment of 0.3μm, as shown in Figure 5.4. To study the second effect, we fixed the distance between the centers of adjacent active material particle and the polymer binder and fixed the radii of the polymer binders at 2.4μm, thus fixing the contact area between adjacent active material particles and polymer binders. The contacting angle was varied from 180^o to 142^o. The setup is shown in Figure 5.5. In the 2nd type of aggregation system, we modeled an aggregated cluster generated considering physical interaction forces. The diameter of the active material particles was 1.0μm, and the total volume of the PVDF binder was determined based on the mass fraction of the constituents of the cathode system. The mass fraction of the active material, PVDF binder and carbon black was 92%, 4% and 4%, respectively. In this work, carbon black is omitted. The discharge rate is 1C.

3. Material Properties

As seen in many engineering materials, the orientation of crystalline and grain microstructures are distributed randomly [24 , 25] so that macroscopic elastic

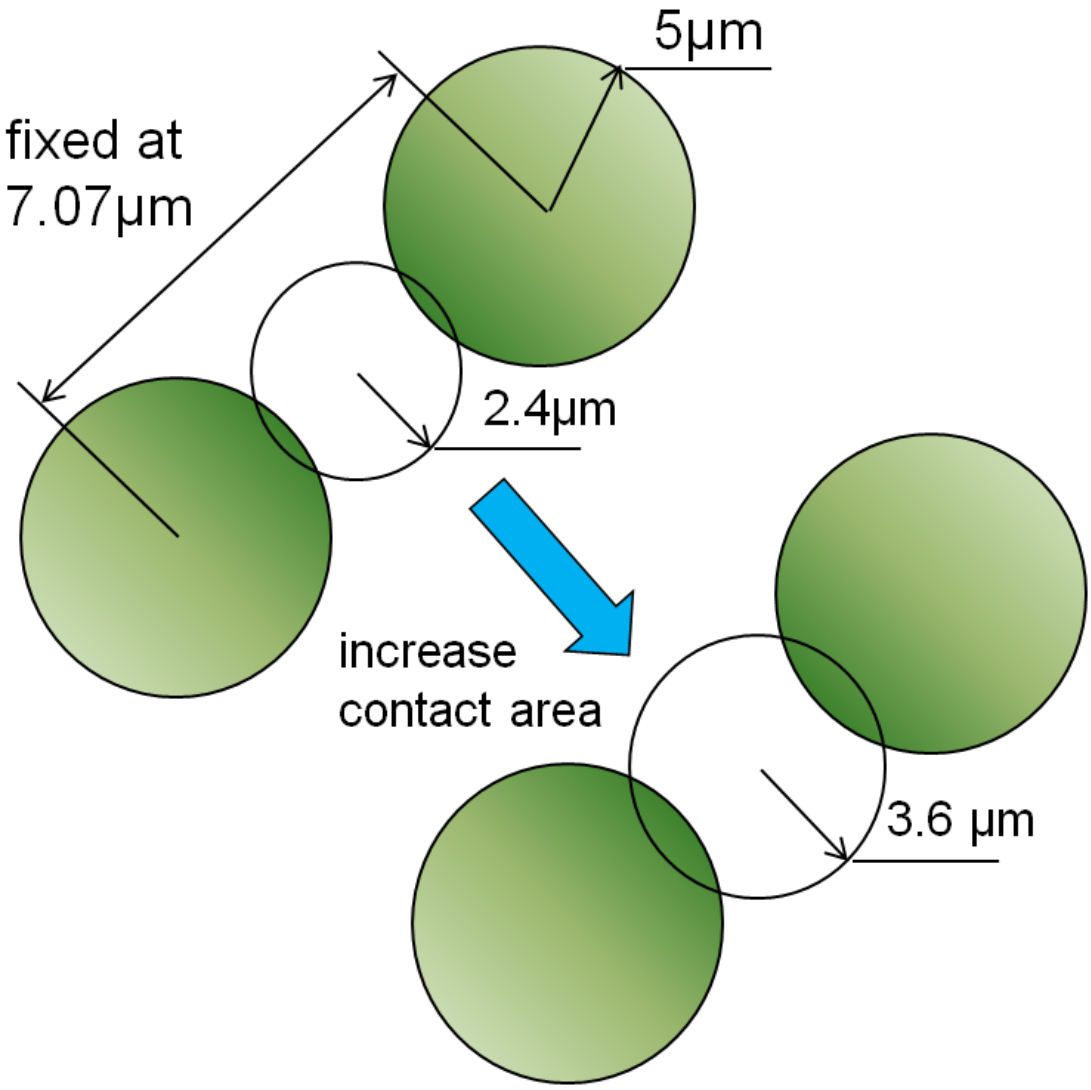

Figure 5.4: Simulation setup to study the effect of contact area between particle and binder

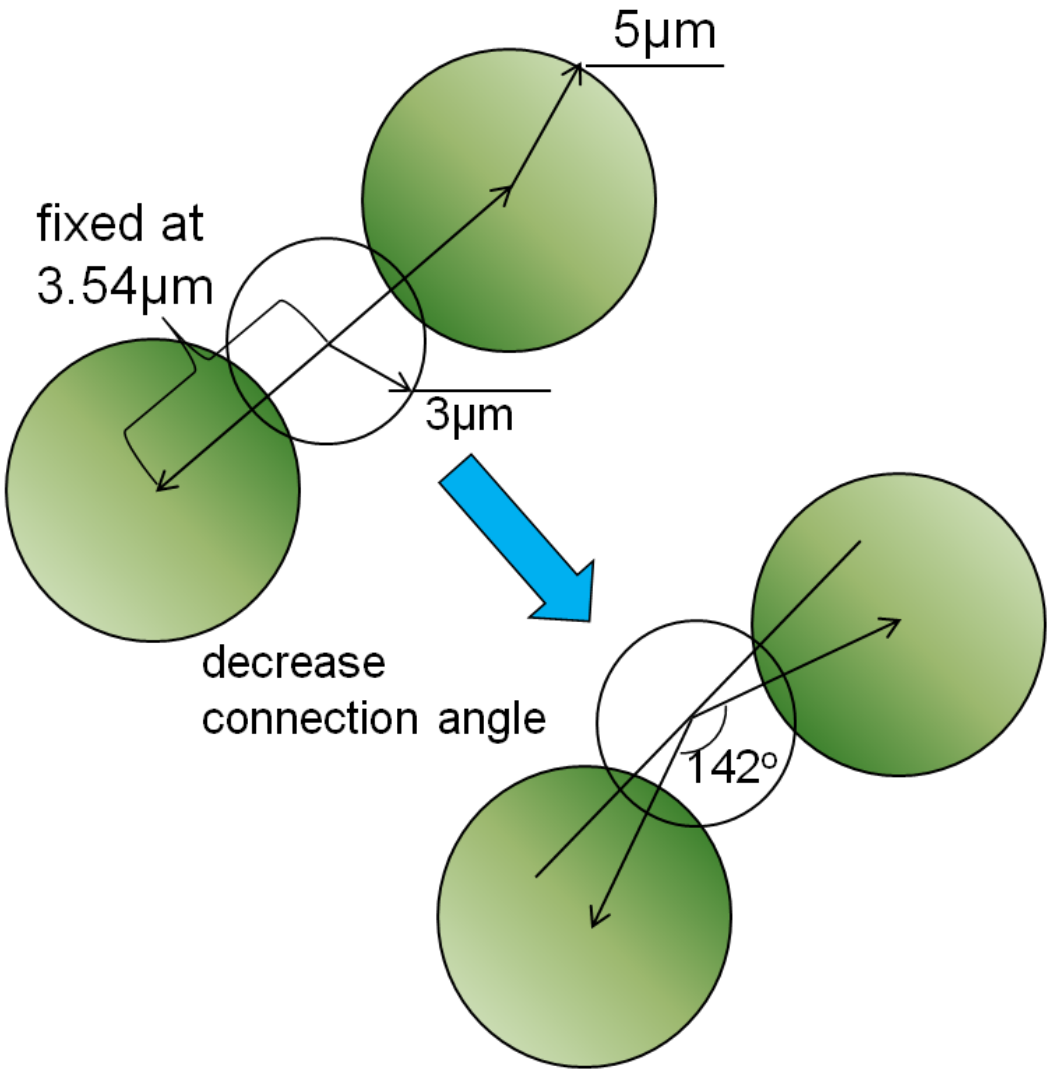

Figure 5.5: Simulation setup to study the effect of relative position between active material particles.

properties are almost equal in all directions. Thus, isotropic behavior was assumed, which was reasonable for the purpose of the present work.

The Young's modulus value for the exact material (Mn_2O_4) in the electrode from direct measurement was not readily available. Values reported in the literature on porous sintered polycrystalline samples and other spinel oxides ranged from 10GPa to 300GPa [26, 27, 28]. In this work, an estimated value of 100GPa was used as Young's modulus.

Because maximum tensile strength for the exact material (Mn_2O_4) was not reported in the literature, this study estimated the maximum tensile strength based on the properties of similar brittle materials. For example, TiO_2, which is also an oxide and has a density similar to $Li_xMn_2O_4$ (4.24g/cm^3 compared to 4.4-4.5 g/cm^3), had a tensile strength of 69-103MPa [19, 29]. The maximum tensile strength was estimated to be 100 MPa for Mn_2O_4 in the simulation. The surface energy was estimated from similar cathode material as 0.66J/m^2 [20].

Material properties are summarized in Table 5.1.

RESULTS

Infinite lattice system – Representative distribution profiles for first principal stress and first principal strain in the infinite lattice system (θ = 0 and PVDF radius = 3μm) at the peak stress level are shown in Figure 5.6. In the profiles shown, when the surface current density is 1.6A/m^2, the maximum tensile stress is 119MPa, exceeding the tensile strength of Mn_2O_4 and PVDF, and the maximum compressive strength is 110MPa, exceeding the compressive strength of PVDF. The maximum strain is 5.99%, well below the elongation limit of PVDF.

Property	Unit	Mn_2O_4	PVDF
Young's modulus (E)	GPa	100 [26, 27, 28]	1.1 [30]
Poisson's ratio (ν)		0.3 [23]	0.3
Elongation	%	-	300 [30]
maximum tensile strength (σ_{TS})	MPa	100 [19, 29]	31 [30]
compressive strength	MPa	-	80 [30]
Diffusion coefficient (D)	m^2/s	7.08×10^{-15} [14]	-
Stoichiometric maximum concentration (c_{max})	mol/m^3	2.29×10^4 [31]	-
surface energy (γ)	J/m^2	0.66 [20]	-

Table 5.1: Material properties of Mn_2O_4 and PVDF

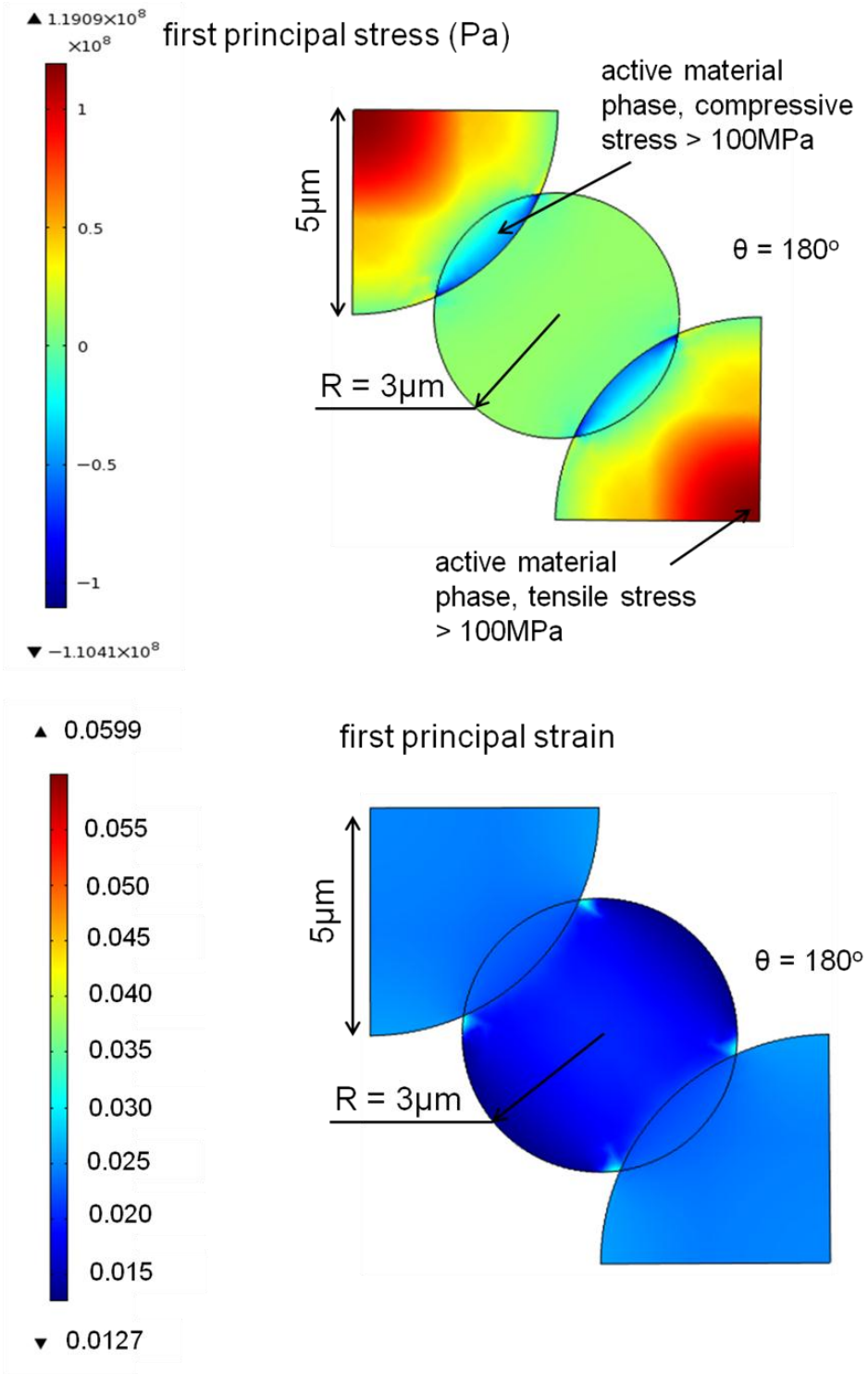

Figure 5.6: Representative distribution profiles for (a) first principal stress and (b) first principal strain for an infinite lattice system at peak stress level

The maximum 1st principal stress values found in the aggregated clusters with different values of R and θ are listed in Table 5.2 and plotted in Figure 5.7. The reference stress value for a single spherical active material particle without PVDF binder is also plotted for comparison (particle radius = 5 μm and surface current density = 1.6A/m^2). The stress level increases with the radius of the PVDF binder, but remains almost unchanged with different angle θ. In all cases, the stress level in the aggregated lattice system is significantly higher than in the single particles.

Aggregates constructed by Brownian Dynamics simulation – At a discharge rate of 1C, for an aggregated cluster consisting of spherical particles with radius 1 μm, the first principal stress at the center of the active material particles was found to peak at 10 seconds into discharge, whereas the surface first principal stress was found to peak at the end of discharge, when the active material particles expanded to their maximum volume.

Li-ion concentration profile and first principal stress profile within an active material particle at 10 seconds into discharge are plotted in Figure 5.8; first principal stress levels at both the active material particle and PVDF binder at the end of the discharge are also plotted in Figure 5.8.

DISCUSSION

This work is the first to extend fracture analysis to the aggregates level in Li-ion battery cathodes. It is also the first work to perform stress analysis on a cathode system consisting of polymer binders as well as active material particles generated from simulations considering realistic inter-particle forces.

R (μm)	2.4	2.7	3.0	3.3	3.6
max. 1st principal stress in active particles (MPa)	100	113	119	124	128

(a)

θ	180°	170°	160°	150°	142°
max. 1st principal stress in active particles (MPa)	119.1	118.9	118.7	117.5	117.1

(b)

Table 5.2: Maximum first principal stress in aggregates with varying (a) radius of PVDF binder and (b) relative angle θ between active material particles

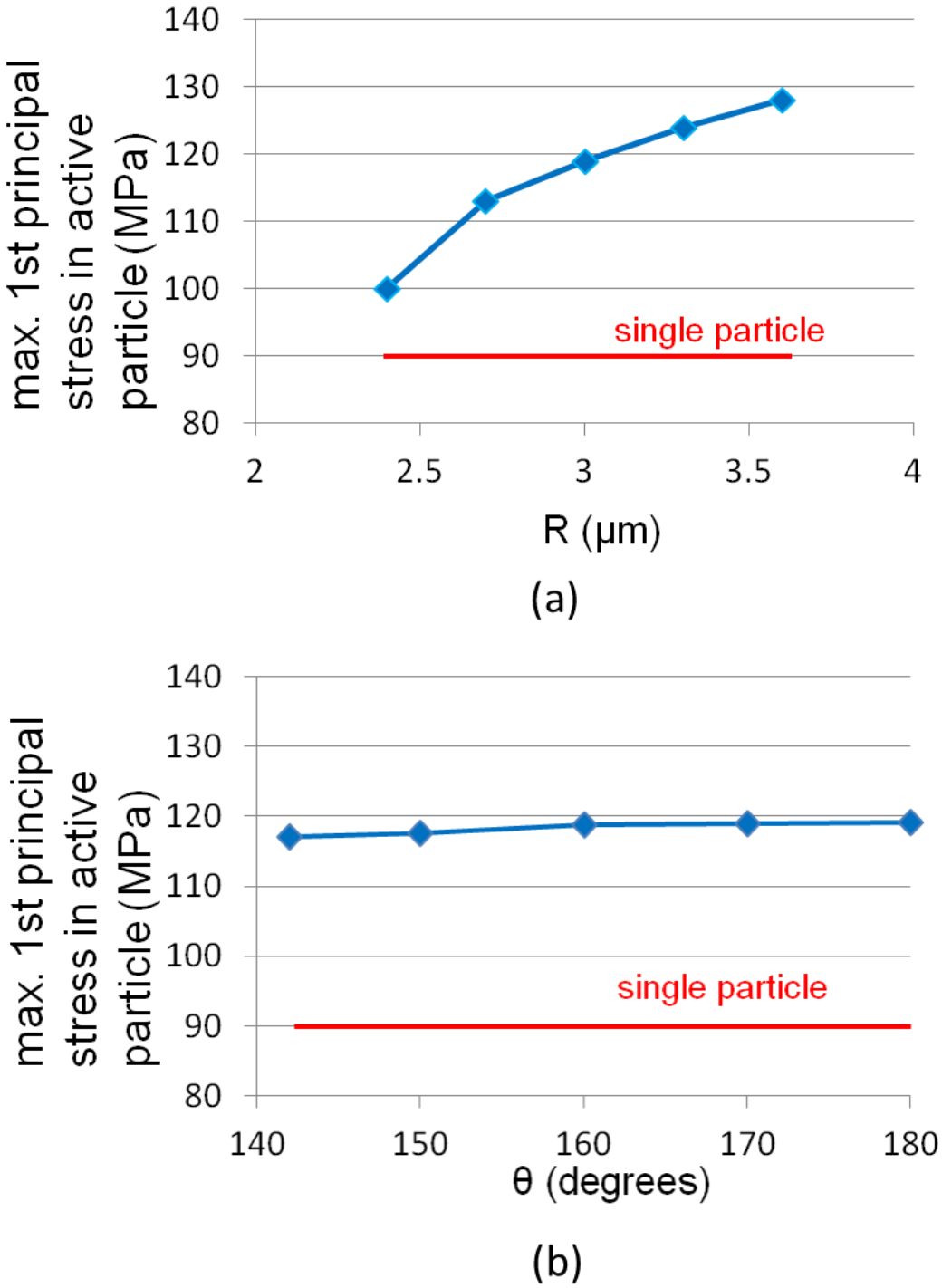

Figure 5.7: Maximum 1st principal stress in aggregates with varying (a) radius of PVDF binder and (b) relative angle θ between active material particles

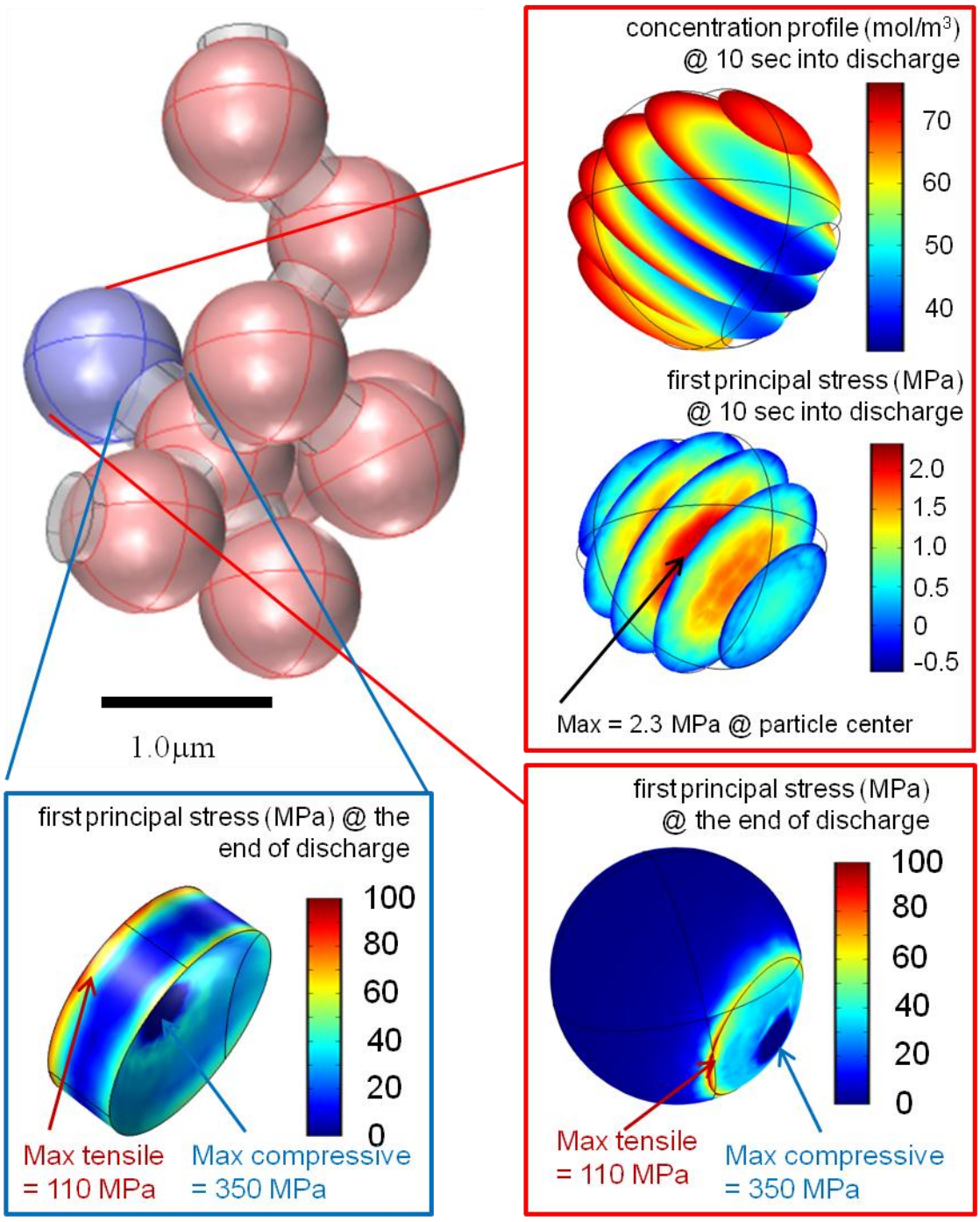

Figure 5.8: (a) Li-ion concentration and (b) first principal within an active material particle at 10 seconds into discharge; first principal stress on the surface of (c) the active material particle and (d) PVDF binder at the end of discharge

The morphology of PVDF binders is simplified. The binders are treated as spheres in the uniform lattice system and cylinders in the Brownian dynamics aggregates system, whereas in the real cathode the morphology of PVDF binders is much more complicated. In this work, we are mainly interested in the effect of parameters such as the AM-PVDF contact area and relative position between AM particles, thus simplifying the PVDF binder shape.

In this work, it is assumed that the active material particles remain in perfect contact with PVDF binders at the interface. Debonding is not simulated even when the stress levels exceed the strength of both the AM and PVDF phases. Realistically, debonding is very likely to occur under such stress levels. However, this work is the first step in fracture analysis on the aggregates level, and we are interested in finding the differences in the fracture behavior between single unconstrained particles and particle clusters. Our results have shown that it is possible for fracture to occur in the cluster (either in AM particles or PVDF binders) under an electrochemical loading condition which will not cause the failure of a single unconstrained particle.

BIBLIOGRAPHY

[1] Wang, D., Wu, X., Wang, Z. and Chen L., 2005, "Cracking causing cyclic instability of $LiFePO_4$ cathode material", *Journal of Power Sources*, **140**, pp. 125–128

[2] Lim, M.-R., Cho, W.-I. and Kim, K.-B., 2001, "Preparation and characterization of gold-codeposited $LiMn_2O_4$ electrodes", *Journal of Power Sources*, **92**, pp. 168-176

[3] Wang, H., Jang, Y.-I., Huang, B., Sadoway, D.R. and Chiang, Y.-M., 1999 "TEM Study of Electrochemical Cycling-Induced Damage and Disorder in $LiCoO_2$ Cathodes for Rechargeable Lithium Batteries", *Journal of The Electrochemical Society*, **146** (2) , pp. 473-480

[4]Christensen, J., 2010, "Modeling Diffusion-Induced Stress in Li-Ion Cells with Porous Electrodes", *Journal of The Electrochemical Society*, **157** (3), pp. A366-A380

[5] Zhu, M., Park, J. and Sastry, A. M., 2011, "Simulation of Particle Interactions in Cathode Material of Li-Ion Batteries", *Journal of The Electrochemical Society*, **158** (10) pp. A1155-A1159

[6] Blyr, A., Sigala, C., Amatucci, G., Guyomard, D., Chabre, Y. and Tarascon, J.M., 1998, "Self-discharge of LiMn2O4/C Li-ion cells in their discharged state - Understanding by means of three-electrode measurements", *Journal of The Electrochemical Society*, **145** (1), pp.194-209

[7] Park, J., Seo, J.H., Plett, G., Lu, W. and Sastry, A.M., 2011, "Numerical simulation of the effect of the dissolution of LiMn2O4 particles on Li-ion battery performance", Electrochemical and Solid-State Letters, v. **14** (2), pp. A14-18.

[8] David, W. I. F., Thackeray, M. M., de Piccitotto, L. A. and Goodenough, J. B., 1987, "Structure refinement of the spinel-related phases Li2Mn2O4 and Li0.2Mn2O4", *J. Solid State Chem.,* **67**, pp.316

[9] Scarminio, J., Talledo, A., Andersson, A. A., Passerini, S. and Decker, F., 1993, "Stress And Electrochromism Induced by Li Insertion In Crystalline And Amorphous V_2O_5 Thin Film Electrodes", *Elecrrochimica Acta*, **38** (12), pp. 1637-1642.

[10] Ohzuku, T., Kitagawa, M. and Hirai, T., 1989, "Electrochemistry of Manganese Dioxide in Lithium Nonaqueous Cell", *J. Electrochem. Soc*., **136** (11), pp.3169

[11] Ohzuku, T., Kitagawa, M. and Hirai, T., 1990, "Electrochemistry of Manganese Dioxide in Lithium Nonaqueous Cell", *J. Electrochem. Soc*., **137**, pp.769

[12] Zaghib, K., Shim, J., Guerfi, A., Charest, P. and Striebel, K. A., 2005, "Effect of carbon source as additives in LiFePO4 as positive electrode for lithium-ion batteries", *Electrochem. Solid-State Lett.*, **8**, pp. A207

[13] Christensen, J. and Newman, J., 2006 "Stress generation and fracture in lithium insertion materials", *J. Solid State Electrochem.*, **10**, pp.293

[14] Zhang, X., Shyy, W. and Sastry, A. M., 2007, "Numerical Simulation of Intercalation-Induced Stress in Li-Ion Battery Electrode Particles", *Journal of The Electrochemical Society*, **154**(10), pp. A910

[15] Zhang, X., Sastry, A.M. and Shyy, W., 2008, "Intercalation-induced stress and heat generation within single lithium-ion battery cathode", Journal of the Electrochemical Society, **155**(7), pp.A542

[16]. Cheng, Y.-T. and Verbrugge, M. W., 2008, "The influence of surface mechanics on diffusion induced stresses within spherical nanoparticles", *J. Appl. Phys.*, **104**, pp.083521

[17] Cheng, Y.-T. and Verbrugge, M. W., 2009, "Evolution of stress within a spherical insertion electrode particle under potentiostatic and galvanostatic operation", *J. Power Sources*, **190**, pp.453

[18]Cheng, Y.-T. and Verbrugge, M. W., 2010, "Diffusion-Induced Stress, Interfacial Charge Transfer, and Criteria for Avoiding Crack Initiation of Electrode Particles", *Journal of The Electrochemical Society*, **157** (4), A508

[19] Christensen, J. and Newman, J., 2006, "A Mathematical Model of Stress Generation and Fracture in Lithium Manganese Oxide", *Journal of The Electrochemical Society*, **153** (6), pp. A1019

[20] Hu, Y., Zhao, X. and Suo, Z., 2010, "Averting cracks caused by insertion reaction in lithium–ion batteries", *J. Mater. Res*., **25**(6), pp. 1007

[21] Woodford, W. H., Chiang, Y.-M. and Carter, C., 2010, "'Electrochemical Shock' of Intercalation Electrodes: A Fracture Mechanics Analysis", *Journal of The Electrochemical Society*, **157** (10), pp. A1052

[22] Zhu, M., Park, J. and Sastry, A. M., 2012, "Fracture Analysis of the Cathode in Li-Ion Batteries: A Simulation Study", *J. Electrochem. Soc.*, **159** (4), pp. A492-A498

[23] Prussin, S., 1961, "Generation and Distribution of Dislocations by Solute Diffusion", *J. Appl. Phys.*, **32**, pp. 1876

[24] He, X., J Cai, . Li, Y., Jiang, C. and Wan, C., 2006, "Preparation of spherical spinel LiMn2O4 cathode material for Li-ion batteries", *Materials Chemistry and Physics*, **95**, pp.105

[25] Choa, T.H., Parka, S.M., Yoshioa, M., Hiraib, T. and Hideshimab, Y., 2005, "Effect of synthesis condition on the structural and electrochemical properties of Li[Ni1/3Mn1/3Co1/3]O2 prepared by carbonate co-precipitation method", *Journal of Power Sources*, **142**, pp. 306

[26] Paolone, A., Cantelli, R., Rousse, G. and Masquelier, C., 2003 " The charge order transition and elastic/anelastic properties of $LiMn_2O_4$", *J. Phys.: Condens. Matter*, **15**, pp.457

[27] Yoneda, A., 1990, "Pressure derivatives of elastic-constants of single-crystal MgO and $MgAl_2O_4$", *J. Phys. Earth*, **38**, pp.19

[28] Ravinder, D., 1994, "Composition dependence of the elastic moduli of mixed lithium–cadmium ferrites", J. Appl. Phys., **75**, pp.6121

[29] Cardarelli, F., 2000, *Materials Handbook: A Concise Desktop Reference*, Springer-Verlag, London

[30] The TexLoc Library, "TexLoc Library – PVDF Properties", Available: http://www.texloc.com/cl_pvdf_properties.html [2011-05-17]

[31] Yamada, A. and Tanaka, M., 1995, "Jahn-Teller structural phase transition around 280K in $LiMn_2O_4$", *Mater. Res. Bull.*, **30**, pp.715

CHAPTER VI

CONCLUSIONS AND FUTURE WORK

AGGREGATION OF SPHERICAL CATHODE PARTICLES

A Brownian dynamics simulation was performed on a binary system (CB and AM spherical particles) with a solid volume fraction of 50%. The final configuration from the simulation shows that all AM particles are aggregated into a single cluster and percolate the simulation domain. Local aggregates of CB particles are observed. CB particles are also observed to connect to the percolated AM clusters. In a battery cathode, it is desirable for a large number of CB particles to connect to AM particles to form pathways through which electrons can flow, thus increasing the conductivity of the electrode.

Our simulation results show that larger AM particle size and higher CB/AM mass ratio each contribute positively to the percentage of CB particles that connect to the percolated AM cluster. Larger AM particle size leads to larger attraction forces binding the CB particles around the AM cluster, thus increasing the percentage of CB attachment. Higher CB/AM mass ratio means a larger CB particle number for a given number of AM particles, so that the CB particles will have a higher probability of interacting with each other and with AM particles, leading to a higher percentage of attachment.

However, the percentage of CB attachment increases with increasing temperature for AM particles possessing a diameter of 1μm, but decreases for AM particles

possessing a diameter of 0.5μm. Increasing temperature leads to increasing Brownian motion. When AM particles are larger, this Brownian motion enables CB particles to overcome the energy barrier and minimize potential. However, the attraction forces between AM particles and CB particles will be sufficiently large to reduce the probability of debonding due to Brownian motion. The end result is an increasing percentage of CB particles connecting to the AM cluster. However, in cases where AM particles are small, the attraction forces are weaker. Higher Brownian motion caused by higher temperature can disturb the connection between particles, leading to a decrease in the percentage of CB attachment. In addition, the Brownian motion effect is more significant for systems of smaller particle size; this also contributes to the decrease in the CB attachment for smaller AM particles.

Further simulation of solvent (NMP) evaporation and the formation of PVDF solid phase following the aggregation process will enable us to determine the electrical conductivity as well as other properties of the fabricated cathode. Future simulations will be conducted in order to map, in detail, the parameters discussed in this work, and to find the optimum conditions that maximize conductivity with minimal added mass.

AGGREGATION OF ELLIPSOIDAL CATHODE PARTICLES

The simulation of cathode particle aggregation was extended to include ellipsoidal particles. Monte Carlo simulation was performed on a system consisting of spherical CB particles and ellipsoidal AM particles in the cathode of Li-ion batteries with a solid volume fraction of 50%. The mass ratio of CB:AM:PVDF is 4%:92%:4%, and the PVDF is not treated as a solid phase in our simulation. After the system stabilized, all AM

particles aggregated and formed a percolating cluster. In the 5 cases we simulated, an average of 42.5% of CB particles attached to the surface of AM particles. The remaining CB particles formed localized aggregates which are not connected to active material clusters; thus, they fail to form conductive pathways, and make no contribution to the conductivity of the cathode.

We compared the result to the case of an aggregated cathode particle system containing only spherical particles, which is simulated using Brownian dynamics and discussed in Chapter II. In this system, the mass ratio of CB:AM:PVDF is also 4%:92%:4%. Simulation parameters such as temperature, volume fraction of solid phase and the mass of each individual particle are the same as in the cases simulated using Monte Carlo simulation, the only difference being the aspect ratio of active material particles. From this comparison, we conclude that the percentage of CB attached to AM clusters increased with increased active material aspect ratio. The surface area for particles with constant volume increases when the particle aspect ratio increases from 1 to 2, which is one of the probable reasons for an increase in the percentage of CB attachment.

In future work, a surrogate model can be created based on the look-up table. In this way, algebra can be used to find interaction potential during simulations, reducing the consumption of memory. In the future, particle size and aspect ratio can also be treated as an additional two parameters and incorporated in the look-up table or surrogate model so that the simulation can be extended to systems that contain particles of continuously varying size and aspect ratio.

FRACTURE ANALYSIS OF SINGLE CATHODE PARTICLES

In this work, multiphysics simulations and linear elastic fracture mechanics were employed to simulate crack propagation in ellipsoidal cathode particles under realistic electrochemical loading conditions.

It was found that a defect at the center of the particle will present the most adverse conditions in terms of failure through fracture during discharge. The maximum principal stress at the particle center ranged from 4.8MPa to 203MPa for particles with sizes from 1μm to 9μm and a discharging current density from 0.1A/m^2 to 0.6A/m^2. The stress level in the most severe case was more than twice the maximum tensile strength. This resulted in crack propagation from the defect. Simulation also confirmed that an initial defect located at the center of the particle required the lowest C-rate (relative to other locations inside the particle or on the surface) to propagate during discharge. The conditions that allowed such initial center defects in spherical and ellipsoidal particles to propagate were explored and mapped. Increasing particle size and current density contributed positively to the tendency toward crack propagation. According to our results, for a spherical particle with a radius of 9μm, a current density of more than 0.25A/m^2 can lead to crack propagation, whereas a 4μm-radius particle can withstand a current density of as high as 0.53A/m^2 without failure through fracture.

However, the C-rates required for cracks to propagate first decreased and then increased with increasing particle aspect ratio. For particles with an aspect ratio of about 1.5:1, the required C-rate for center defects to propagate was the lowest at 0.18C.

Our simulation demonstrated that fracture can develop from defects under moderate C-rates for a range of particle sizes. However, due to the power-law correlation

between the particle size and the maximum allowable C-rate, particles with a size below 1μm are very resistant to fracturing (max. allowable discharge rate > 10C). Thus, fracture effect should be considered in the design of batteries to minimize capacity degradation; further, one may reduce the risk of fracturing by using particles with sizes smaller than certain threshold values.

In future work, phase transition needs to be modeled in the fracture analysis since it is difficult to control the charge/discharge rate for a single particle during cycling in a real electrode, and some particles may have significantly higher surface current density than average. Also, the single particle fracture analysis model can be extended to irregular and non-smooth cathode particles with multiple convex and concave surfaces. The geometry of these real world particles may be obtained using methods such as atomic force microscopy. Other defects, such as phase boundaries and/or grain boundaries, can also be included in future fracture analysis.

FRACTURE ANALYSIS OF CATHODE AGGREGATES

Multiphysics simulation was extended to the stress analysis of aggregated structures in the cathode. The stress profile results from simulation are essential for predicting failure in the cathode system. We performed simulations on both uniform lattice systems as well as aggregates generated using Brownian dynamics. In both types of systems, the general profile of stress distribution in the active material particles in the clusters is similar to that of a single active particle with an unconstrained outer surface.

In the uniform lattice system with active material particles 10μm in diameter, the maximum first principal stress was found at the center of the particles, indicating that

crack propagation is most likely to occur when the initial defect is located at the center. With the addition of polymer binder, the maximum principal stress in the active material particle increased from 89.9MPa in a single particle with unconstrained outer surface to beyond 100MPa, thus increasing the propensity toward crack propagation. We also found that increasing the contact area between active particles and polymer binders will significantly increase the maximum first principal stress in the active particles, which rose from 100 MPa to 128 MPa as the diameter of the binder sphere increased by 50% in our simulation. However, changing the connection angle between active particles (from 180^{o} to 142^{o}) while maintaining constant contact area only changed the stress level slightly. According to the findings in Chapter IV, crack propagation will not occur in single active particles with unconstrained outer surfaces within the parameter range in our simulation. ,In the lattice system, however, the PVDF binder material will not experience failure during discharge based on the stress profile found, whereas crack propagation will occur in the active particles if an initial defect is present at the center.

In the aggregate system generated by Brownian dynamics simulation, the active material particles are 1.0μm in diameter. Under a discharge rate of 1C, the typical peak value of the first principal stress during discharge is ~2.3MPa at the particle center; this is not significantly different from the stress level found in a particle with an unconstrained outer surface. In the particle network, compressive stress on the order of 300MPa occurs near the contact point of two adjacent particles, and tensile stress on the order of 100MPa occurs at the interface between the active particle and PVDF binder; this exceeds the compressive strength and tensile strength of the PVDF. The stress level in the binder exceeds the strength of the PVDF; thus, although connection type, degree of bonding and

the geometry of the binder will affect the stress level, failure in the binder is a possible failure mechanism in batteries.

In future work, debonding behavior will be included in the fracture analysis, and the dominant failure mode for cathode aggregates will be determined. Additionally, the impact of fracture/debonding to the conductivity of the cathode system will be investigated.

Further, an iterative method can be implemented, and data can be passed back and forth between intercalation-induced stress calculation and fracture/debonding simulation. The newly exposed active material surface will add to the Li-ion diffusion pathways and consequently change the Li-ion distribution profile. An iterative method will update the geometry of particles repetitively for the electrochemical simulation as crack propagation or debonding ensues.

BATTERY OPTIMIZATION

When it comes to the optimization of Li-ion batteries, conductivity, specific energy, and fracture need to be considered. Of particular importance are the effects that temperature, additive-active material mass ratio, particle size and shape have on these battery performance parameters.

The maximum allowable discharge rates are beyond 10C for particle sizes 0.5μm and 1.0μm, which means that these small particle sizes are very resistant to fracture under practical battery usage. We can thus focus our optimization efforts on the effects of input parameters on conductivity and specific energy for particles with radii under 1.0μm.

Since the total mass of the carbon black particles that attach to the active material and form conductive paths is directly related to the conductivity of the cathode, we calculated this mass as a fraction of the total mass of the cathode system and listed the values for each parameter combination in Table 6.1 below. The specific energy of the cathode system (containing AM, CB and PVDF) for each case was also calculated, assuming that the theoretical capacity for $Li_xMn_2O_4$ is 150Ah/kg.

Table 6.1 shows that conductivity is the most sensitive to the additive-active material mass ratio: when conductive additive mass is increased from 4% to 8% of the total cathode mass, the total mass of attached CB increases from below 2% to 6.92% of the total cathode mass. This translates into a significant increase in conductivity. At the same time, the specific energy only decreases slightly from 138Ah/kg to 132Ah/kg. This decrease of specific energy can be justified by the significantly increased conductivity. Larger active material particle size and aspect ratio are also preferable as long as the particle size is kept under 1.0μm, ensuring that fracture will be unlikely for discharge rates under 10C.

To conclude: according to the findings regarding batteries optimization discussed in this thesis, we would set conductive additive mass at 8% of the total cathode mass, and use active material particles with an aspect ratio of 2 and a volume equal to those of the spheres with 1.0μm radius.

FINAL REMARKS

It is known that aggregation of inactive and active materials in the Li-ion battery electrodes greatly impact the conductivity and power performance of the electrodes. This work is the first attempt to numerically simulate this process using techniques such as

Brownian dynamics and Monte Carlo method, and to reveal the effects of particle shape, size, mass ratio and temperature on the packing of cathode particles. Future work may focus study on the effective diffusivity and the electrical conductivity of the resultant aggregated structures, and their linkage to battery cell performance.

For now, the methods developed here form a toolkit with which to study present generation materials, continuously, from raw materials to battery electrodes. The coupled multiphysics analysis and fracture modeling, and simulation of the behavior of electrode particles of general shapes, under realistic charging and discharging conditions, demonstrated here, may also be extended. Grain boundaries, phase transitions, and fatigue caused by repeated cycling will also be targets for the academic community to investigate. In doing so, a more holistic analysis of battery materials may be possible, one that may offer greater insight into the design and selection of storage materials.

AM aspect ratio	1			2
mass ratio (CB:AM)	4% : 92%		8% : 88%	4% : 92%
AM size (diameter for spheres)	1.0 µm	0.5 µm	0.5 µm	volume equals to 0.5µm sphere
specific energy	138 Ah/kg	138 Ah/kg	132 Ah/kg	138 Ah/kg
max. C-rate before fracture	>10C	>10C	>10C	>10C
mass of attached CB (% of total cathode mass)	1.73%	1.00%	6.91%	1.70%

Table 6.1: Cathode optimization for specific energy, fracture, and conductivity